Metallophthalocyanines linked to metal nanoparticles and folic acid for use in photodynamic therapy of cancer and photoinactivation of bacterial microorganisms.

A thesis submitted in fulfilment of the requirement for the degree of

DOCTOR OF PHILOSOPHY

of

RHODES UNIVERSITY

By

GAUTA GOLD MATLOU

https://orcid.org/0000-0002-2373-2365

MARCH 2020.

DEDICATION

This thesis is dedicated to all the big dreamers, the visionaries, the winners, and all those who defies the odds to succeed in their dreams.

ACKNOWLEDGEMENTS

I would like to give thanks to my supervisors and the institute of nanotechnology and innovation team, Dist. Prof Tebello Nyokong, Dr Jonathan Britton, Prof John Mack, and Ms Gail Cobus for the great mentorship and assistance during my PhD Study. Thanks again to the NRF (National Research Foundation) for the funding during my doctoral program.

To my Lab S22 colleagues and managers over the years (2016-2019), Japan colleagues and collaborators (Prof Nagao Kobayashi & Prof Mitsumi Kimura), and the Rhodes University chemistry department, thank you very much for the help and support during my times in the laboratory or department. A deep appreciation to papa Francis, Sherly and Marvin at EM-unit for keeping the instruments well maintained and running for all of us, thank you.

A special gratitude to my wife: Offentse Ingrid, my mom: Maria Mmapula Matlou, my siblings and their kids, my church mates, my great friends and relatives for the prayers, the support and all the inspiring messages to keep me going. Kea Leboga, we did it together. Let us get more, impossible is nothing.

Tloga-tloga e tloga kgale, modiša wa dikgomo otšwa natšo šakeng.

ABSTRACT

This thesis presents on the synthesis and characterization of novel asymmetric and symmetrical metallophthalocyanines (MPcs) substituted with carboxylic acid functional groups and centrally metallated with zinc and indium. The MPcs are further covalently linked to cysteine capped silver nanoparticles (cys-AgNPs), amino functionalized magnetic nanoparticles (AMNPs) and folic acid (FA) through an amide bond between the carboxylic group of MPcs and the amino group of FA, cys-AgNPs or AMNPs. The covalent linkage of MPcs to FA improved the water solubility of MPcs and allowed for singlet oxygen quantum yield determination in water. Asymmetric MPcs and their conjugates were found to have improved photochemical and photophysical properties compared to symmetrical MPcs and their conjugates. The heavy atom effect of AMNPs and AgNPs improved the triplet and singlet oxygen quantum yields of MPcs.

MPcs and their conjugates (MPc-FA, MPc-AMNPs, MPc-AgNPs) were found to have lower *in vitro* dark cytotoxicity and higher photodynamic therapy (PDT) activity on MCF-7 breast cancer cells. The water soluble MPc-FA had better PDT activity when compared to MPc-AMNPs due to the active targeting of folic acid-folate binding on cancer cell surface. MPcs and MPc-AgNPs conjugates also showed excellent *in vitro* cytotoxicity on *S. aureus* under light irradiation compared to dark cytotoxicity. The photosensitizing properties of MPcs and their conjugates are demonstrated for the first time in this thesis, both on breast cancer cells (MCF-7) through photodynamic therapy and on microorganisms (*S. aureus*) through photodynamic antimicrobial chemotherapy.

TABLE OF CONTENTS

Section ***Page***

LIST OF ABBREVIATIONS

ADMA	= Anthracene -9, 10 – bis-methylmalonate.
APTES	= 3- amino propyl triethoxysilane
AMNPs	=Amino functionalized magnetic nanoparticles.
Cys-AgNPs	= Cysteine functionalized Silver nanoparticles.
DBU	=1.8-diazabicyclo [5.4.0] undec-7-ene.
DCC	= *N, N'*-dicyclohexylcarbodiimide
DCM	= Dichloromethane
DLS	=Dynamic light scattering
DMSO	=Dimethyl sulfoxide
DMF	=*N, N*-Dimethyl formamide
DPBF	= Dipheylisobenzofuran.
EPR	= Enhanced permeability and retention
FA	=Folic acid
FTIR	= Fourier transform infrared spectroscopy
ISC	= Intersystem crossing
PACT	=Photodynamic antimicrobial chemotherapy
PBS	= Phosphate buffer saline
PDT	=Photodynamic therapy
PS	=Photosensitizer
MPcs	=Metallophthalocyanines
NHS	= *N*-hydroxysuccinimide

NPs	=Nanoparticles
NMR	=Nuclear magnetic resonance spectroscopy
ROS	= Reactive oxygen species
TCSPC	= Time-correlated single photon counting
TEM	=Transmission electron microscope
TEOS	= Tetra ethyl orthosilicate
Uv/Vis	= Ultraviolet/ visible spectroscopy
XRD	= X-ray diffraction spectroscopy

LIST OF SYMBOLS

S_1 = Excited singlet state

S_0 = Ground singlet state

Φ_F = Fluorescence quantum yield

τ_F = Fluorescence lifetime

hv = Light

μ = micro ($x10^{-6}$)

ε = Molar extinction coefficient

α = Non-peripheral position

β = Peripheral position

Φ_Δ = Singlet oxygen quantum yield

τ_T = Triplet state lifetime

Φ_T = Triplet quantum yield

T_1 = Triplet excited state

λ = Wavelength

CHAPTER 1

INTRODUCTION

Preamble

This thesis presents the synthesis of symmetrical and asymmetric metallophthalocyanines (MPcs) centrally metallated with zinc and indium. The MPcs are covalently linked to folic acid (FA), magnetic nanoparticles (MNPs) and silver nanoparticles (AgNPs). The photophysical and photochemical properties of MPcs, MPc-FA, MPc-AMNPs and MPc-AgNPs conjugates are reported, together with their photocytotoxicity efficacy on breast cancer cells (MCF-7) and microbes (*Staphylococcus aureus*).

1.1 METALLOPHTHALOCYANINES.

Metallophthalocyanines (MPcs) are macrocyclic structures with 18 π-electron aromatic porphyrin synthetic analogues, consisting of four diiminoisoindoline units linked together through nitrogen atoms, Fig 1.1. MPcs have been extensively studied for their exclusive properties that are due to the electronic delocalization and extensive hetero-aromatic π-conjugation structure. The MPc's structure allows for insertion of different heavy metals in the central cavity, can also be substituted on the peripheral (β) and non-peripheral (α) positions with various substituents to improve the physical, electronic and optical properties of the complex [1–3].

These properties, together with excellent thermal and chemical stabilities and low toxicity have made MPcs great candidates for use in various fields including gas sensors [4], optical limiting applications [5], catalysis [6] and as photosensitizers in photodynamic therapy [PDT] [7] and in photodynamic antimicrobial chemotherapy (PACT) [8]. For this work, MPcs substituted at the peripheral (β) position with carboxylic acid containing substituents are used as photosensitizer agents for PDT and PACT.

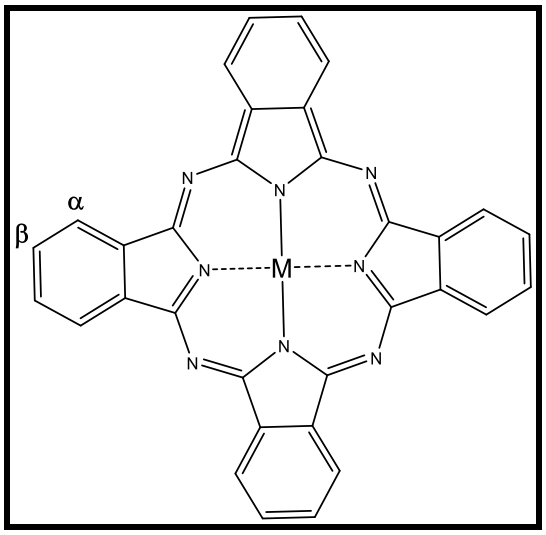

Fig 1.1. A typical structure of metallophthalocyanine depicting the α and β positions of the isoindoline units.

1.1.1 Spectroscopy.

MPcs have two strong distinctive absorption bands known as the Q and B bands. The Q-band is the single most intense band in the visible region (ca 670 nm and beyond) [9,10] while the B-band consist of two superimposed bands (B_1 and B_2) that appear as a broad peak in the ultraviolet region (300 - 400 nm) [11], Fig 1.2. Using the four-orbital model proposed by Gouterman [12], the Q-band is as a result of the transition between the ground state a_{1u} of the highest occupied molecular orbital (HOMO) to e_g of the lowest unoccupied molecular orbital, while the B-bands are due to the a_{2u} to e_g (B_1) and b_{2u} to e_g (B_2) transitions, Fig 1.3.

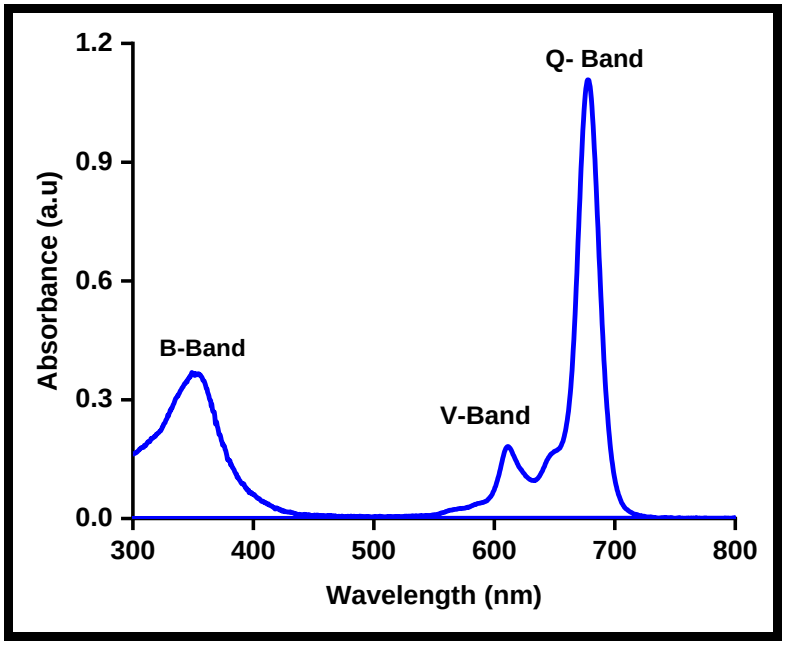

Fig 1.2. Typical ground state electronic absorption spectra of MPcs in DMSO. Unpublished work.

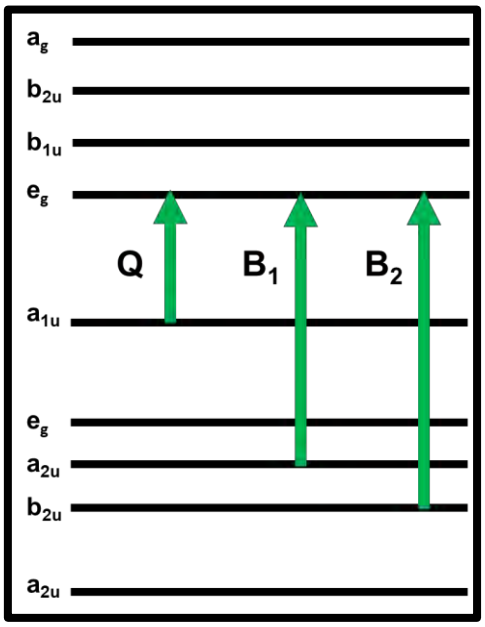

Fig 1.3. Electronic transitions showing the origin of the Q-band and the B-bands of MPcs.

MPcs typically form aggregates in solution. Aggregation is a result of interactions between the π-systems of the Pc rings, resulting in blue or red shifting and splitting of the Q-band. Fig 1.4 shows the electronic transitions that are caused by the two types of aggregates found in Pcs. The formation of such aggregates causes a split of the excited state energy level, Fig 1.4. The J-aggregates results in red shifting and H-aggregates results in blue shifting of the Q-band [13,14]. H-aggregates are formed when there is parallel stacking of the monomer units while J-aggregates forms when the monomer units form end to end stacking.

Aggregation can be reduced by the presence of bulky substituents or addition of axial ligands to defer the association of the rings. In this work, bulky *tert*-butyl containing substituents were introduced as secondary substituents on asymmetric MPcs to reduce aggregation.

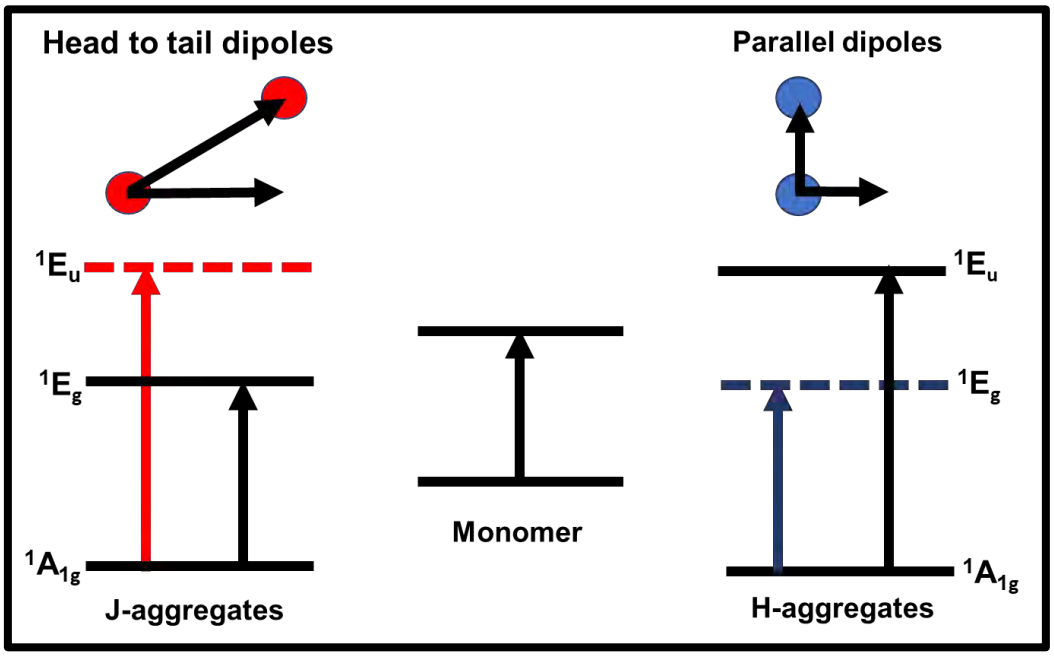

Fig 1.4. Molecular exciton theory depicting the electronic transitions for J and H-aggregates of MPcs.

1.1.2 Synthesis.

There are several methods that can be used to synthesize MPcs, Scheme 1.1. The synthesis of MPcs from the precursors such as phthalic anhydride, phthalic acid, phthalimide, o-dibromobenzene, o-cyanobenzamide and phthalonitrile is achieved through cyclotetramerization reaction in the presence of metal salt (MX) and a catalyst [15–18]. Phthalic anhydride route is usually used in large scale production of MPcs since the starting material is cheaper [19].

The phthalonitrile route, as was used in this study, gives higher purity of MPcs. The preparation of substituted MPcs can be achieved from the condensation of one or two substituted phthalonitriles in the presence of a metal salt, a high boiling point solvent and a catalyst (commonly 1,8-diazabicyclo [5.4.0]undec-7-ene (DBU)), Scheme 1.2 B. Different substituted phthalonitrile precursors of MPcs can be prepared through the nucleophilic substitution of the nitro groups of 3- or 4-nitrophthalonitrile in the presence of potassium carbonate at room temperature [20], Scheme 1.2 A.

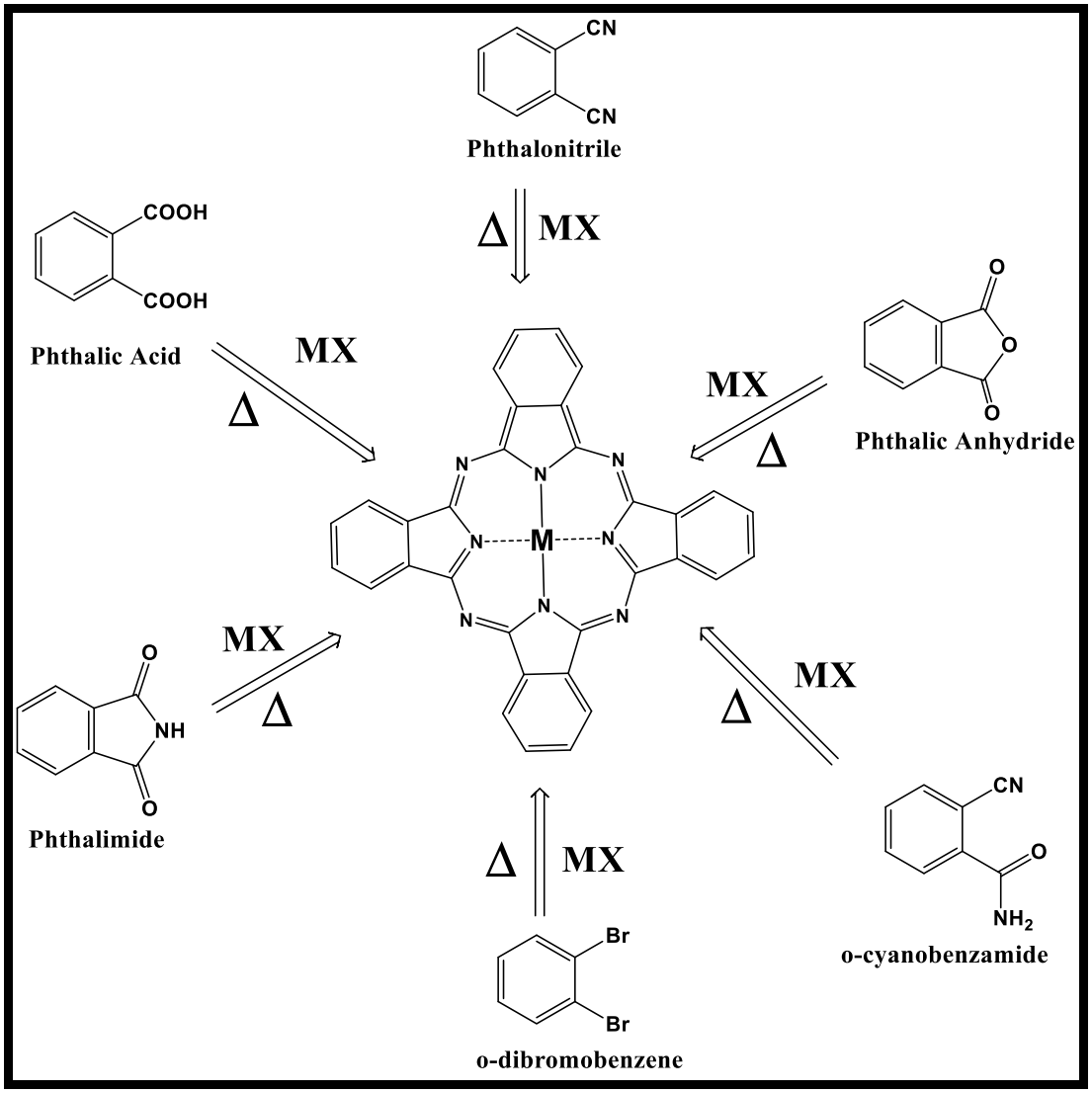

Scheme 1.1. Synthetic routes of MPcs from various precursors.

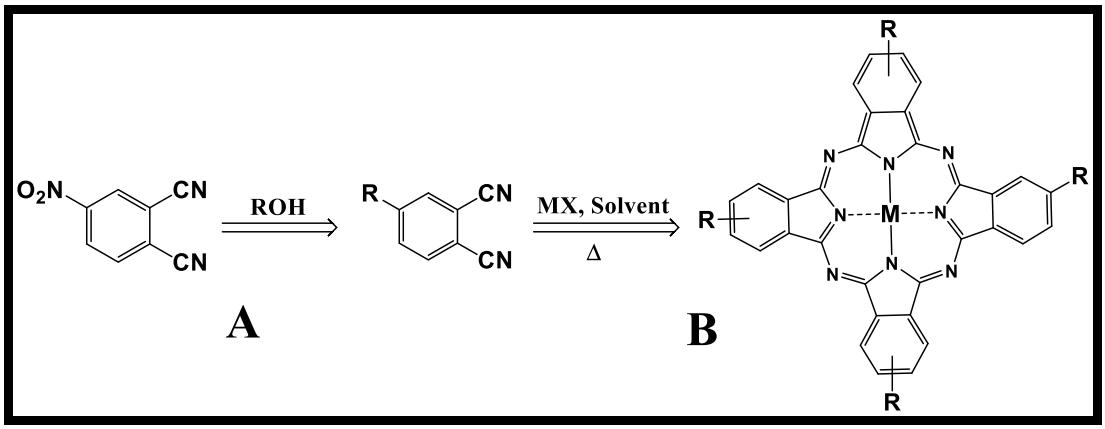

Scheme 1.2. Illustration of the synthesis of a tetra substituted MPcs from 4-nitrophthalonitrile.

Symmetrically substituted MPc derivatives are synthesized from one phthalonitrile (Scheme 1.2) while asymmetric type MPc derivatives are synthesized from a mixed condensation of two phthalonitriles (Scheme 1.3). Asymmetric MPcs are of interest as they provide one point of co-ordination, whilst exhibiting unique set of properties required for use in applications such as PDT [21], PACT [8], optical limiting and material science [22]. Mixed condensation reaction of two phthalonitrile (A and B) results in a mixture of six MPcs labelled ABBB, AABB, ABAB, BBBB, AAAB and AAAA, Scheme 1.3.

A higher yield and purity of asymmetric (ABBB type MPc) can be achieved by adjusting the mole ratio of B to be thrice or higher than that of A [15,23], followed by chromatic separation and purification. This study reports on both the symmetrical and asymmetric carboxyl MPcs, and further link the MPcs to folic acid, silver, and magnetic nanoparticles through an amide bond.

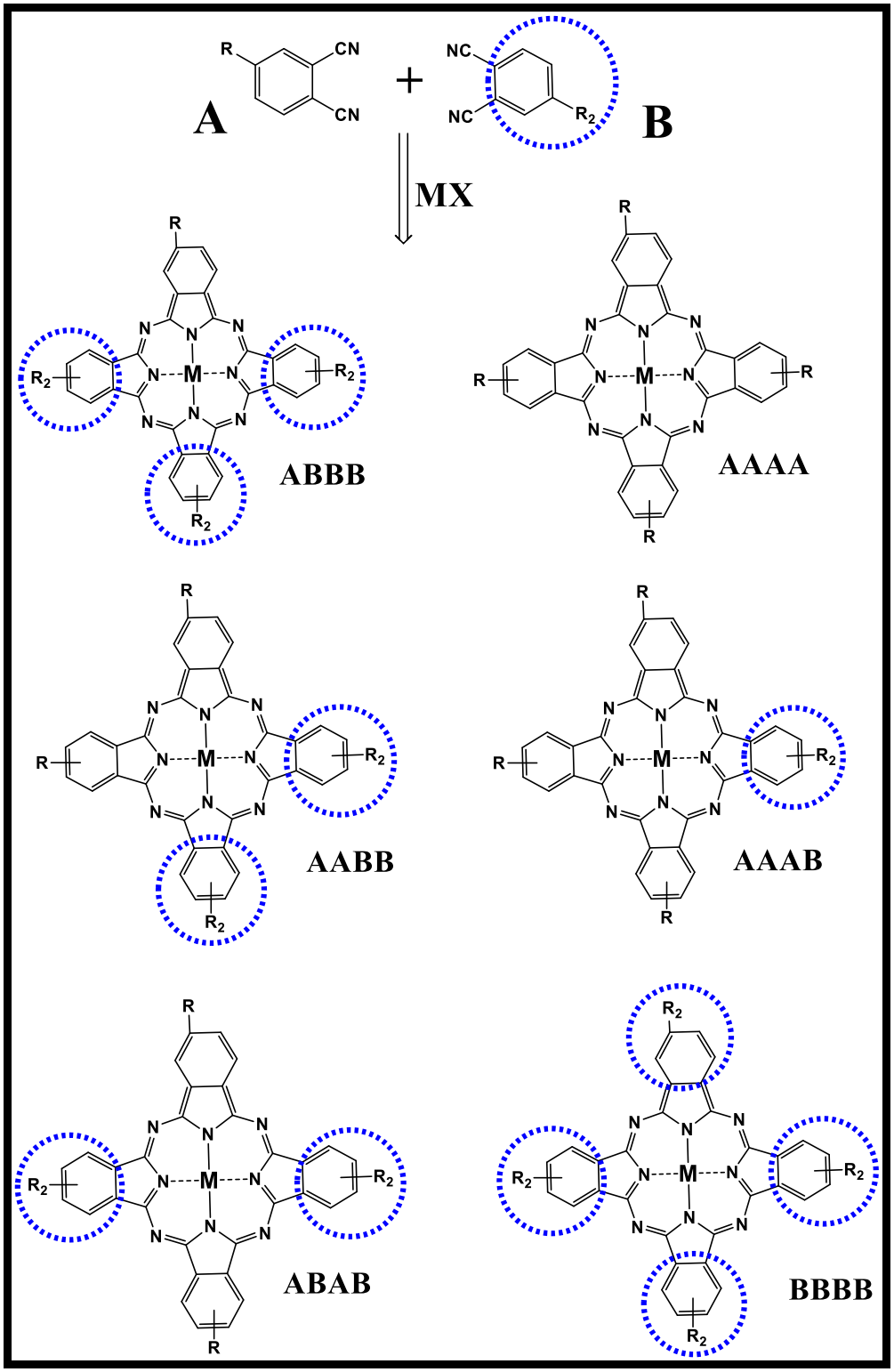

Scheme 1.3. Mixed condensation reaction of two phthalonitrile (A and B) complexes to yield a mixture of six MPcs.

1.2 PHOTODYNAMIC THERAPY.

Photodynamic therapy (PDT) of cancer has been extensively studied as an alternative to conventional cancer treatments such as chemotherapy and radiotherapy. These treatment methods have extensive side effects such as toxicity to kidneys and bone marrow, increasing drug resistance overtime, hair loss and nausea [24,25]. An advantage of PDT is that the administered photosensitizer (PS) agent is harmless until activated by light. The activation of the PS agent by light of specific wavelength generates cytotoxic singlet oxygen that is responsible for the destruction of tumour cells.

1.2.1 MPcs in PDT.

MPcs are well-known photosensitizer agents [7] with known compounds in clinical trials for the treatment of cancer, Fig 1.5. Photosens and Pc-4 are already at the advanced stages of the clinical trials [26,27]. MPcs with central metals such as Zn (II), Sn (IV) and Ge (IV) are preferred MPc derivatives for PDT application due to their ability to increase intersystem crossing (ISC) of excited molecules to the triplet state. These MPcs have also shown to have longer triplet lifetimes and quantum yields that can effectively interact with ground state molecular oxygen ($^3O_2$) to produce cytotoxic singlet oxygen ($^1O_2$) [28,29]. It is for this reasons that this work focused on preparing MPcs containing Zn (II) and In (III) as photosensitizer agents on breast cancer cells.

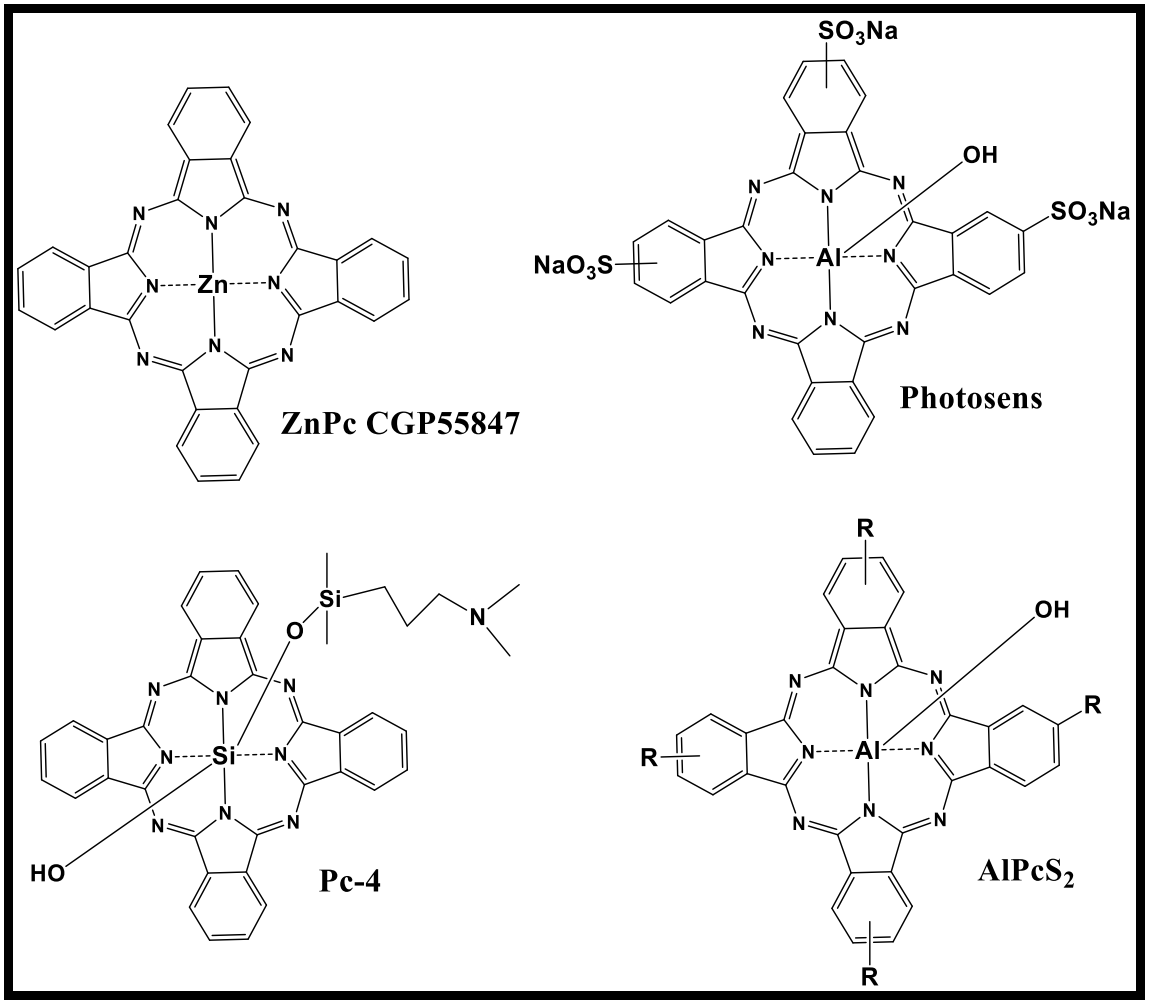

Fig 1.5. MPcs currently in clinical trials.

1.2.2 PDT mechanism.

Scheme 1.4 shows the Type I and Type II photochemical mechanisms that are followed by MPcs after photoexcitation with light. MPcs in the ground state absorbs energy from light to reach the electronically excited singlet state (^{1}MPc*). The short-lived ^{1}MPc* undergoes ISC to the long-lived triplet excited state (^{3}MPc*) [30]. Type II mechanism involves the generation of singlet oxygen from the interaction of molecular oxygen ($^3O_2$) with the MPc in the excited triplet state (^{3}MPc*).

In the Type I mechanism, the ^{3}MPc* interacts with the molecular oxygen to generate superoxide and hydroperoxyl radicals that oxidizes the substrate, Scheme 1.4. The Type II mechanism is the most common in PDT [28].

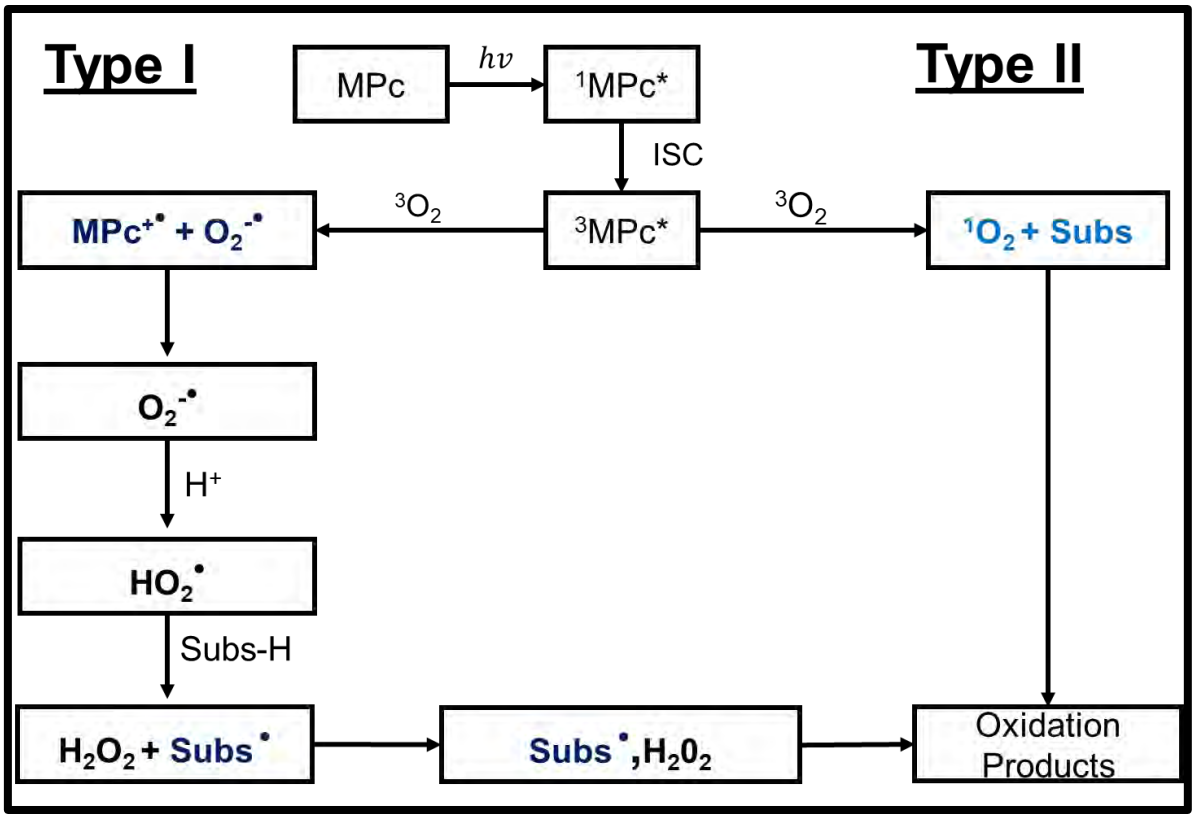

Scheme 1.4. Schematic representation of Type I and Type II photochemical mechanism of PDT. ISC =Intersystem crossing, Subs = Substrate.

1.2.3 Specificity in PDT.

The main drawback of PDT is non-specificity and non-selectivity of photosensitizer agents to cancerous cells over normal cells [31]. Enhanced delivery, retention and localization of photosensitizer agents can be achieved through active and passive targeted drug delivery systems, which further increases efficiency of the treatment [32]. Active targeting involves the use of photosensitizer agents linked to ligand molecules that are specific cancer cell surface markers (receptors or antigens) which are over-expressed on tumour cell surfaces [33]. Molecules such as antibodies, aptamers, folic acid, peptides and oligonucleotides are typically been used as high affinity ligands [34].

For this work, MPcs are linked to folic acid (FA) to maximize the selectivity and retention of MPcs on tumour cells through folic acid-folate receptors binding. A number of malignant cells have folate receptors expressed on their surfaces, which helps them to multiply rapidly during cell proliferation [35,36]. Linking MPcs to FA, results in tumour-selective drug delivery system [37] that could improve the PDT activity of MPcs on the cancer cells.

Passive targeting takes advantage of the leaky intratumoral blood vessels. Photosensitizer agents are linked to nanocarriers that can permeate through the leaky blood vessels and deliver the drug at the cancer site, a phenomenon known as enhanced permeability and retention (EPR) effect [38,39]. Nanomaterials with unique physicochemical properties such as quantum dots, gold nanoparticles, liposomes and magnetic nanoparticles (MNPs) [39–42] have been used previously as nanocarriers for PS agents. In this work, silver nanoparticles (AgNPs) and

magnetic nanoparticles (MNPs) are used as nanocarriers for MPcs to optimize the accumulation of MPcs at the cancer site [32]. Additionally, the heavy atom of nanoparticles is known to improve the photosensitizing properties through external heavy atom effect [41,43]. Table 1.1 lists previously reported MPcs conjugated to different cancer specific biomolecules and nanoparticles for application in PDT using different cancer cell lines [7,21,44–54]. In this work, the photodynamic activity of MPcs covalently linked to folic acid (FA), AgNPs and MNPs on MCF-7 human breast adenocarcinoma cell is investigated.

The conjugation of FA to MPcs was previously achieved by amide bond linkage between the NH_2 of MPcs and the COOH of FA [49,50,52]. This will be the first time that the linkage of MPcs to FA is achieved by using the COOH of MPcs with the NH_2 of FA, Table 1.1. FA molecules possesses two carboxyl groups, termed α and γ. Linking MPcs to COOH moiety of FA (especially the α) disrupts folate receptor binding recognition [55], hence this work uses the amino group instead of the COOH groups of FA employed in the past. Additionally, MPcs reported in this work are mono substituted with carboxyl groups which offers a more defined amide bonding to the primary NH_2 of FA compared to the previously reported tetra substituted amino ZnPc [52].

MPc-MNPs mixed conjugates were previously reported for PDT of cancer cells [47]. Covalently linked MPc-MNPs are reported for the first time in this work for use in PDT, Table1.1. The MNPs reported in this work are amino functionalized, which affords amide bonding to the COOH groups of MPcs. Covalent linkage ensures that

the conjugates does not separate during PDT. Photosensitizers such as MPcs linked to MNPs possess a further advantage of a targeted PDT mode with combined magnetic resonance imaging [56].

MPc-AgNPs conjugates have also been reported for PDT [21,51], the conjugation of MPcs to AgNPs was achieved through affinity binding of thiol groups of Pcs to Ag surface [21] and the covalent linkage of MPcs to AgNPs [51], Table 1.1. This work reports for the first time on the covalent linkage of MPcs to AgNPs using cysteine as a linker. Cysteine is a small chain molecule without an extra amide bond compared to the previously reported glutathione [57]. Additionally, the asymmetric MPcs used in this work have cinnamic acid substituents compared to acetic acid [51] and alkyl thiols [21] of reported complexes, Table 1.1. Cinnamic acids are natural carboxylic acid containing compounds with known inhibitory properties against fungi, tumour and parasites [58–60], hence are used in this study to further improve the PDT efficiency of MPcs. Their carboxylic acid groups are also used to form an amide bond with the NH_2 of cysteine on AgNPs surface.

The effects of symmetry and substituents on the photophysical and photochemical properties of MPcs linked to AgNPs or MNPs, as well as their PDT activity on MCF-7 breast cancer cells are investigated. The heavy atoms of MNPs and AgNPs are also used to improve the photosensitizing properties of MPcs by influencing ISC of excited molecules through heavy atom effect.

Table 1.1. MPc-conjugates used in PDT.

Complex	Cell-line	Ref
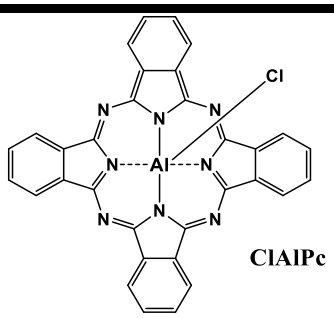 Chloro aluminium Pc (ClAlPc) and ClAlPc mixed MNPs.	Human mesenchymal stem cells derived from bone marrow (BM-MSC), Human glioma cell lines (tumorigenic: U87MG and non-tumorigenic: T98G)	[47]
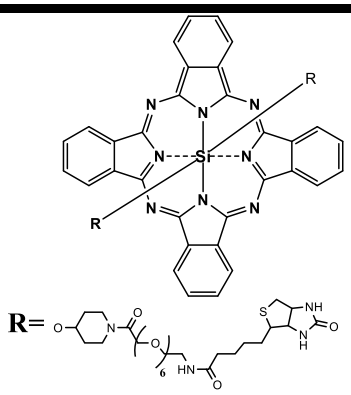 Axially substituted biotin SiPc	Hela cells (Hela human cervical carcinoma cells)	[48]
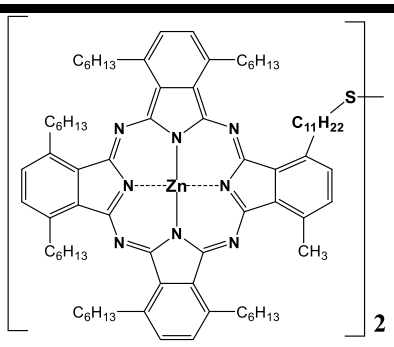 ZnPc disulphide (C11Pc) and C11Pc-AuNPs	B78H1 cell line (amelanotic clone of murine melanoma)	[7]

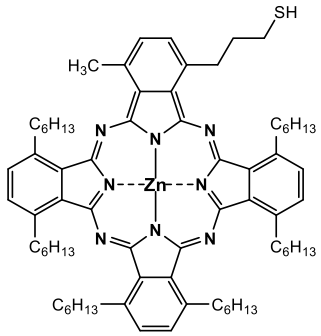 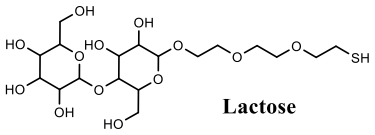 Asymmetric ZnPc and lactose linked to AuNPs through Au-S bonds.	MDA-MB-231 human breast adenocarcinoma and MCF-10A human mammary epithelial cells.	[21]
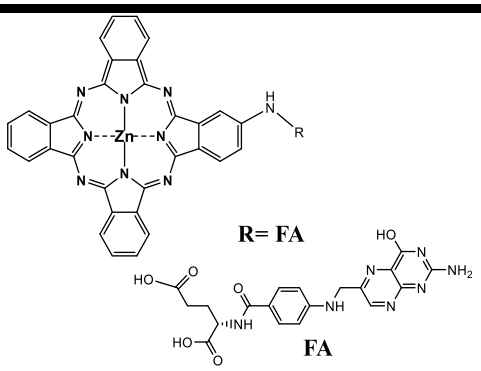 Zinc (II) mono amino Pc (ZnMAPc) and ZnMAPc linked to folic acid.	MCF-7 human breast adenocarcinoma cells.	[49,50]
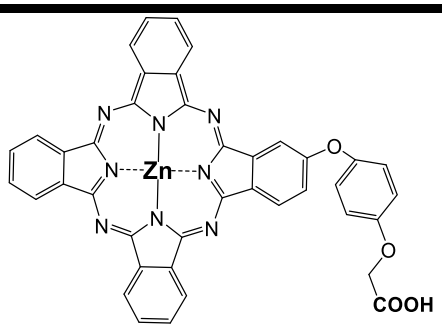 ZnPc mono acetic acid conjugated to AgNPs and AuNPs.	MCF-7 human breast adenocarcinoma cells.	[51]

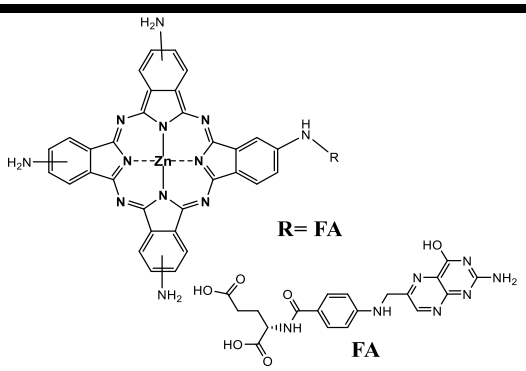 Zn tetra amino Pc (ZnTAPc) and ZnTAPc linked to folic acid (FA)	KB cells (human nasopharyngeal epidermal carcinoma cell lines) and A549 cells (human lung epithelial carcinoma cancer cell lines).	[52]
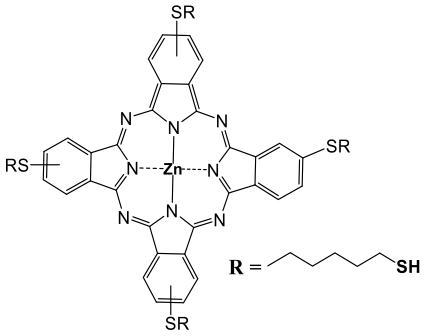 Tetra hexanyl dithiol ZnPc linked to AuNPs	MCF-7 human breast adenocarcinoma cells, and healthy fibroblast cells.	[53]
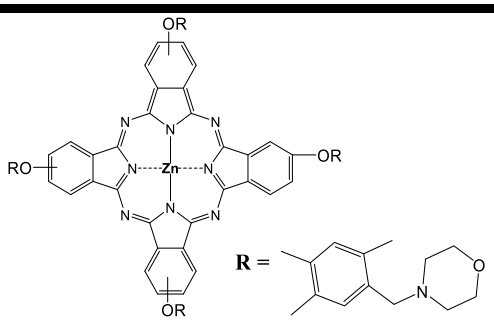 Zn tetra morpholino methyl phenoxy Pc conjugated to biotin-graphene quantum dots	MCF-7 human breast adenocarcinoma cells.	[54]

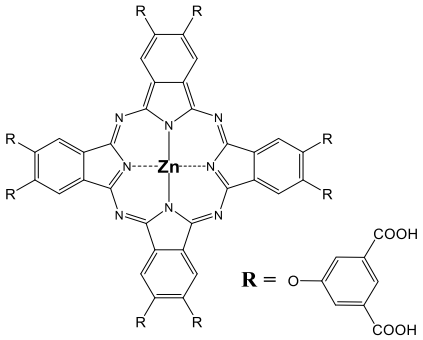 ZnPc/upconversion nanoparticle coated with hyaluronic acid (HA) crosslinked gel.	Human gastric cancer cell line SGC-7901.	[44]
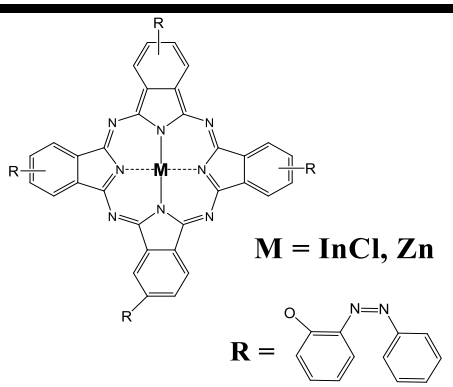 Tetra phenyldiazenyl phenoxy phthalocyanines incorporated into Pluronic® F127 micelles.	MCF-7 human breast adenocarcinoma cells.	[45]
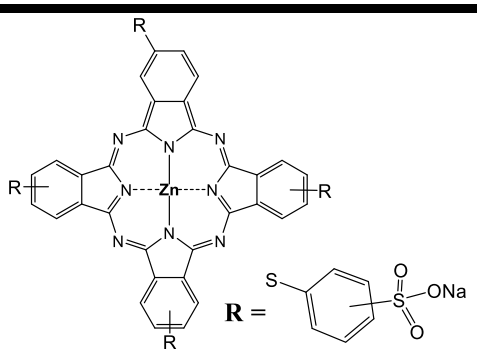 Sulfonated ZnPc loaded in lipid nano-carriers.	Liver hepatocellular carcinoma (HepG2) cells	[46]

1.3 PHOTODYNAMIC ANTIMICROBIAL CHEMOTHERAPY.

1.3.1 Background.

Photodynamic antimicrobial chemotherapy (PACT) is a promising photoinactivation modality based on the same principle as PDT of cancer, but for bacterial killing. In PACT, the administered photosensitizer localizes in the microbial cells for a given period followed by irradiation with light of appropriate wavelength to produce reactive oxygen species (ROS) that inactivates the bacterial microorganisms [8,61,62]. MPcs are common photosensitizer agents that are used in PDT [7,63] and have now found a role in PACT [8].

The difference in cell walls of Gram (+) bacteria such as *Staphylococcus aureus* or Gram (-) such as *Escherichia coli* plays a key role in the efficiency of photosensitizer agent in PACT. Gram (+) bacteria have a thick and porous peptidoglycan layers that surround an outer membrane, while Gram (-) bacteria possess an outer membrane, surrounding a thinner peptidoglycan layer that contain cytoplasmic membrane [64,65]. This makes it easier for photosensitizer agents to permeate and localize within the cytoplasm of Gram (+) bacteria as compared to Gram (-) bacteria. Thus, this study employs neutral ZnPc derivatives as photosensitizer agents for the photoinactivation of Gram (+) *S. aureus* microbes. *S. aureus* is resistant to Methicillin and is one of the most studied microbe [7,66]. It causes life-threatening skin, soft tissue and blood stream infections in hospitals and within communities [67], hence this work focuses on the photoinactivation of *S. aureus* as the target bacterium.

1.3.2 MPc-nanoparticle conjugates in PACT.

The interest on nanomedicine in the last decades has been fuelled by the unique and interesting properties that nanoparticles possess [68]. In PACT, nanoparticles are conjugated to MPcs to improve the singlet oxygen quantum yields of MPcs [69] which further improves the inactivation efficiency of MPcs [70] on the bacteria. Nanoparticles can also be used to improve the solubility, delivery and accumulation of photosensitizer agents to the bacteria [70,71]. Titania dioxide nanoparticles (TiO_2) [72], magnetic nanoparticles (MNPs) [73,74], silver nanoparticles (AgNPs) [57,75] and gold nanoparticles (AuNPs) [69,75] are some of nanoparticles that have been used in conjugation with MPcs for PACT on different microbes.

In this study, MPcs covalently bound on the surface of silver nanoparticles (AgNPs) are reported. Covalently bound MPc-nanoparticle conjugates yield better properties compared to embedded or mixed conjugates due to the lack of separation during treatment and the synergistic properties of nanoparticles and the MPcs [70]. AgNPs have proven antimicrobial properties [76] which will be taken advantage of to improve PACT efficiency. Additionally, the plasmon-resonance effect of AgNPs has the potential to improve the photoantimicrobial efficiency of conjugates on the microorganisms [77], hence AgNPs are used in this work as nanocarriers of ZnPcs for use in PACT. The heavy atom of AgNPs is also known to improve the intersystem crossing of molecules to the excited triplet state, thus improving the generation of cytotoxic singlet oxygen responsible for bacterial killing.

Table 1.2 lists conjugated MPcs that have been reported for PACT [57,72–75,78–82]. Neutral MPcs have been shown to be effective for the photoinactivation of different microorganisms [57,72,74,75,78,79,81,82]. This work reports for the first time on cinnamic acid substituted ZnPcs for application in PACT. Cinnamic acid derivatives have proven therapeutic agents with inhibitory activity against fungi, tumor and parasites [59,60]. Their incorporation as ring substituents on ZnPcs for applications in PACT is expected to improve the inactivation of microorganisms. The effect of symmetry and substituents of ZnPcs alone and when covalently linked to AgNPs on PACT are reported for the first time in this study.

MPcs conjugated to AgNPs for application in PACT have been reported before [57,75,79]. As previously discussed, covalent linkage through an amide bond of MPcs to AgNPs using cysteine as a linker are reported for the first time in this study as compared to previously reported affinity binding using Ag-S bonds [79] and covalent linkage through glutathione capped AgNPs [57]. The amide bond between the NH_2 groups of cysteine AgNPs and the COOH of asymmetric MPcs is more defined as cysteine only has one NH_2 moiety. The cinnamic acid ZnPcs and their AgNPs conjugates are applied for the photoinactivation of *S. aureus* as a target bacterium.

Table 1.2. MPc-conjugates used in PACT.

Complex	**Microbe**	**Ref**
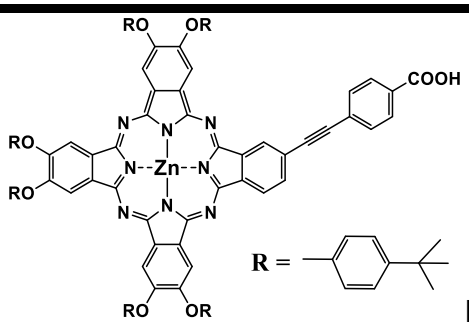 **Neutral.** Asymmetric carboxy ZnPc coupled with TiO_2 NPs	*S. aureus.*	[72]
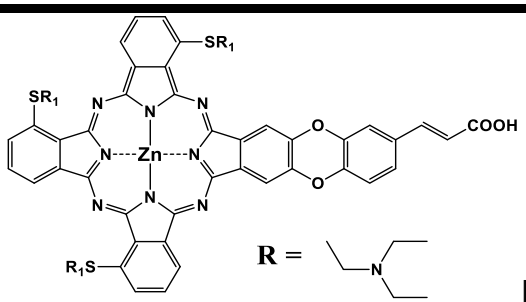 **Neutral.** ZnPc mono caffeic acid conjugated to AgNPs.	*E. coli.*	[57]
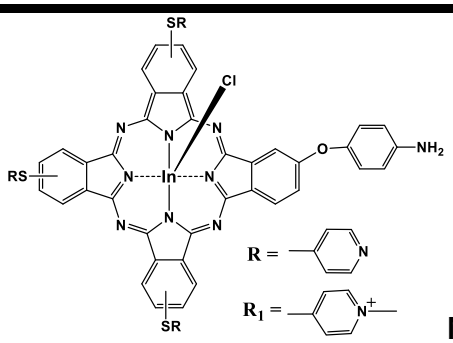 **Neutral, Quaternized**. InCl mono amino-phenoxy Pcs alone, when quaternized and conjugated to MNPs	*E. coli.*	[73]

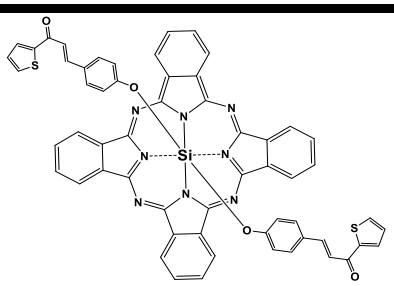 **Neutral**. Axially substituted 2-thienylpropenyl phenoxy SiPc	*S. aureus,* *E. coli.*	[78]
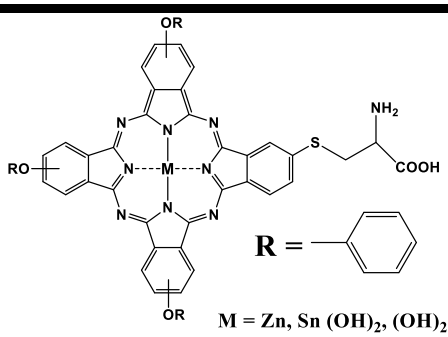 **Neutral**. Mono cysteinyl MPcs conjugated to AgNPs.	*S. aureus.*	[79]
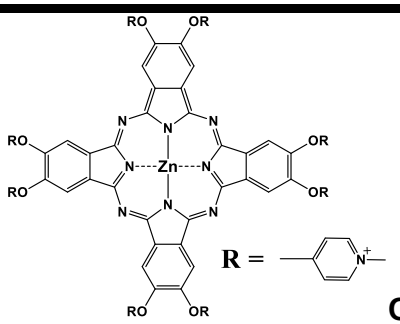 **Cationic**. Octa 1-methylpyridine ZnPc	*S. aureus,* *E. coli,* *C. albicans.*	[80]
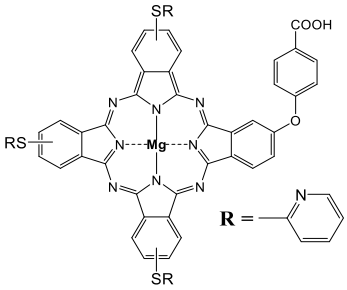 **Neutral.** MgPc mono carboxy phenoxy, tri-mercaptopyridine, Linked to MNPs	*E. coli.*	[74]

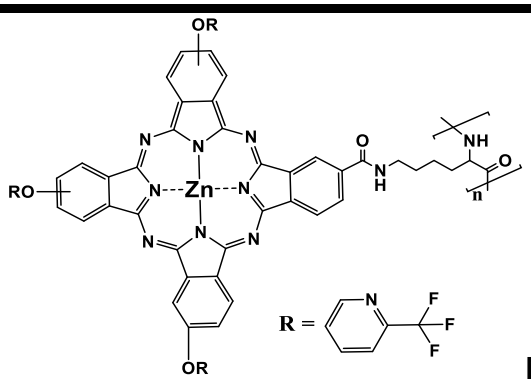 **Neutral.** Asymmetric ZnPc-ε-polylysine (ZnPc-ε-PL) conjugated to AgNPs or AuNPs.	*S. aureus.*	[75]
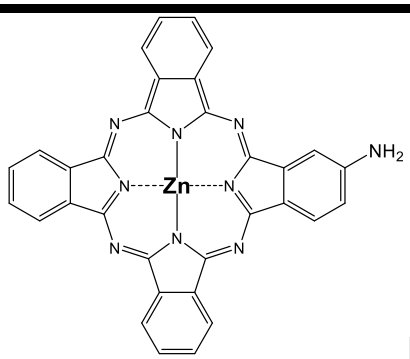 **Neutral.** Zn mono amino Pc functionalizes poly (glycidyl methacrylate) nano-assemblies.	*S. aureus,* *E. coli.*	[81]
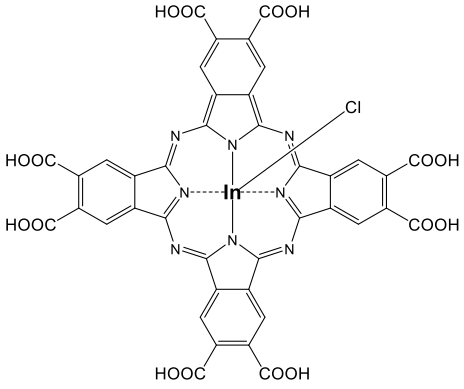 **Neutral**. Indium octa carboxy Pc linked to MNPs	*S. aureus.*	[82]

1.4 METALLOPHTHALOCYANINES USED IN THIS STUDY.

MPcs used in this work are shown in Table 1.3. Zn (II) 2-mono-(carboxy phenoxy) phthalocyanine (**2**) [83] has been reported before. Zn (II) tris-(*tert*-butyl)-2-(carboxy phenoxy) phthalocyanine (**1**), Zn (II) 2-mono-(4-oxy cinnamic acid) phthalocyanine (**3**), Zn (II) tris-(*tert*-butyl)-2-(4-oxy cinnamic acid) phthalocyanine (**4**), Zn (II) tris-(4-*tert*-butyl phenoxy)-2-(4-oxy cinnamic acid) phthalocyanine (**5**), Zn (II) 2(3), 9(10), 16(17), 23(24)-tetrakis-(4-oxy cinnamic acid) phthalocyanine (**6**) and InCl (III) 2(3), 9(10), 16(17), 23(24)-tetrakis-(4-oxy cinnamic acid) phthalocyanine (**7**) are reported for the first time in this study. The conjugation of MPcs (**1-7**) is achieved through an amide bond formation between COOH groups of MPcs and NH_2 group of cys-AgNPs, or AMNPs or FA.

Asymmetric MPcs **1-5** have one COOH group that is used as the point of attachment while symmetrical **6** and **7** have four COOH groups that can form attachment during conjugation. Stoichiometric mole ratio is used at the activation stage to allow activation of one COOH group to avoid chain reactions during conjugation, Table 1.3.

Table 1.3. MPcs that were studied in this work.

Complex	**Conjugated to**	**STUDIES**
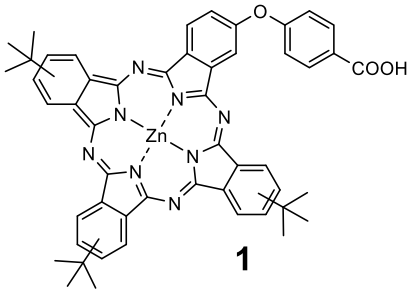 **1** Zinc (II) tris (*tert*-butyl)-2-(carboxy phenoxy) phthalocyanine.	Folic acid (FA) and magnetic nanoparticles (AMNPs). **1**-FA **1**-AMNPs	**<u>Photophysical and photochemical studies.</u>** Φ_{F}, Φ_T, Φ_{Δ}, τ_F , τ_T
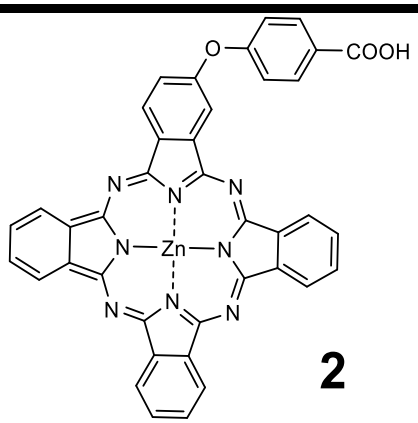 **2** Zinc (II) 2-mono-(carboxy phenoxy) phthalocyanine [83].	Folic acid (FA) and magnetic nanoparticles (AMNPs). **2**-FA **2**-AMNPs	**<u>Photophysical and photochemical studies</u>** Φ_{F}, Φ_T, Φ_{Δ}, τ_F , τ_T **<u>Application</u>**. -PDT

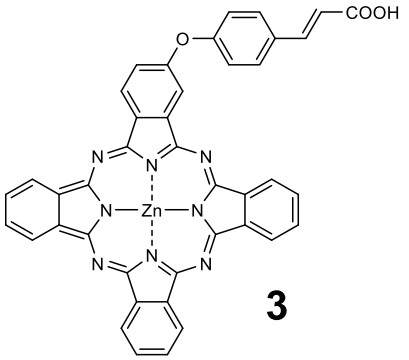 **3** Zinc (II) 2-mono-(4-oxy cinnamic acid) phthalocyanine.	Folic acid (FA), magnetic nanoparticles (AMNPs) and silver nanoparticles (cys-AgNPs). **3**-FA, **3**-AMNPs, **3**-cys-AgNPs	**Photophysical and photochemical studies** Φ_F, Φ_T, Φ_Δ, τ_F, τ_T **Application**. -PDT -PACT
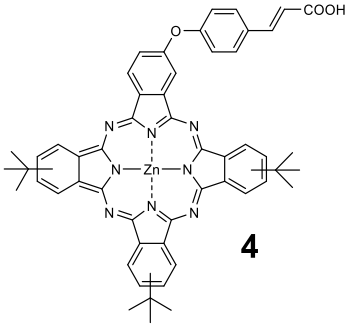 **4** Zinc (II) tris-(*tert*-butyl) 2-(4-oxy cinnamic acid) phthalocyanine	Silver nanoparticles (cys-AgNPs) and magnetic nanoparticles (AMNPs). **4**-cys-AgNPs **4**-AMNPs	**Photophysical and photochemical studies** Φ_F, Φ_T, Φ_Δ, τ_F, τ_T **Application**. -PDT -PACT
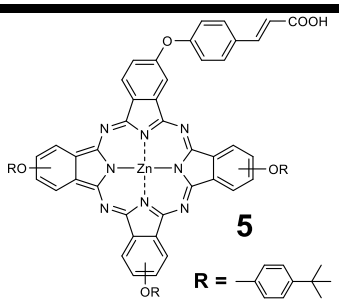 **5** R = Zinc (II) tris-(4-*tert*-butyl phenoxy)-2-(4-oxy cinnamic acid) phthalocyanine	Silver nanoparticles (cys-AgNPs). **5**-cys-AgNPs	**Photophysical and photochemical studies** Φ_F, Φ_T, Φ_Δ, τ_F, τ_T **Application**. -PACT

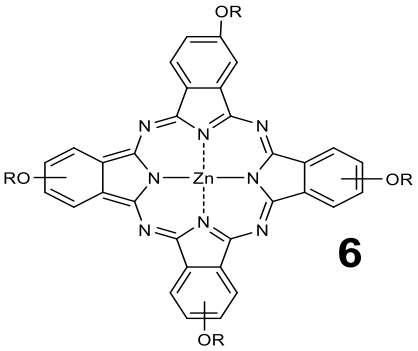 **R =** 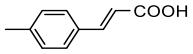 Zinc (II) 2(3), 9(10), 16(17), 23(24)-tetrakis-(4-oxy cinnamic acid) phthalocyanine	Magnetic nanoparticles (AMNPs) and silver nanoparticles (cys-AgNPs). **6**-AMNPs **6**-cys-AgNPs	**<u>Photophysical and photochemical studies</u>** Φ_{F} , Φ_T, Φ_{Δ} , τ_F , τ_T **<u>Application</u>**. -PDT -PACT
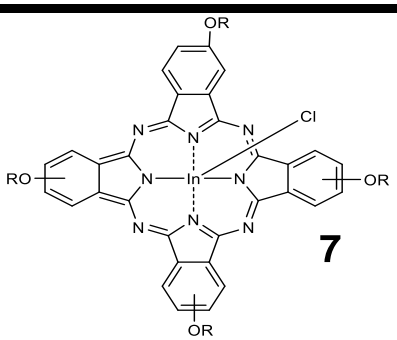 **R =** 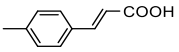 Indium (II) chloride 2(3), 9(10), 16(17), 23(24)-tetrakis-(4-oxy cinnamic acid) phthalocyanine	Magnetic nanoparticles (AMNPs) **7**-AMNPs	**<u>Photophysical and photochemical studies</u>** Φ_{F} , Φ_T, Φ_{Δ} , τ_F , τ_T **<u>Application</u>**. -PDT

MPcs and conjugates reported in this thesis will be compared for their photophysical and photochemical properties and their photocytotoxicity on MCF-cells and *S. aureus*. The effect of symmetry, substituents, central metal, metal nanoparticle or folic acid conjugation on the singlet oxygen generation abilities and PDT or PACT cytotoxicity will be investigated and compared. This will be for the first time that the same MPcs are applied for both PDT and PACT.

1. Asymmetric MPcs **1**-**5** will be compared to symmetrical MPcs **6** and **7** for the effect of symmetry on the photophysical and photochemical properties.
2. **6** and **7** alone and when conjugated to AMNPs will be studied for the effect of the central metal on the photophysical and photochemical properties as well as the PDT efficiency on MCF-7 breast cancer cells.
3. The effect of substituents and conjugation of **1** and **2** to FA and AMNPs on the photophysical and photochemical properties will be investigated. Complex **2** has only the carboxy phenoxy substituent, while **1** has carboxy phenoxy and *tert*-butyl as its substituents. The cinnamic acid asymmetric MPcs (**3**-**5**) will also be compared with each other and to the carboxy phenoxy asymmetric MPcs **1** and **2.**
4. The effect of *tert*-butyl and *tert*-butyl phenoxy substituents on **4** and **5** alone and when linked to cys-AgNPs will be compared for their effect on the photophysical and photochemical properties and the PACT efficiency on *S. aureus*.

5. MPcs **3**, **4**, and **6** will be used to compare the effect of metal nanoparticle (AMNPs or AgNPs) conjugation on the photophysical and photochemical properties.
6. The effect of specificity on the efficiency of PDT using MCF-7 cells will be studied using MPcs **2** and **3** when conjugated to FA and AMNPs.
7. **3**, **4**, **4**-cys-AgNPs and **6** will be compared for their cytotoxic efficiency on MCF-7 through PDT and on *S. aureus* through PACT. Complex **5** and **5**-cys-AgNPs will also be tested for PACT efficiency on *S. aureus* and compared to those of **3**, **4** and **6** with their conjugates.

1.5 NANOPARTICLES USED IN THIS STUDY.

1.5.1 Magnetic nanoparticles.

Iron oxide (Fe_2O_3) magnetic nanoparticles (MNPs) have attracted attention in nanotherapeutics due to their biocompatibility, biodegradability, and high surface biofunctionality. The extensive attention on MNPs is also due to their unique magnetic properties that have been exploited to render MNPs as dual diagnostic tools as magnetic resonance imaging and targeted drug carrier systems for therapy [84].

Synthesis of MNPs can be achieved from different methods that includes sol-gel synthesis [85], microemulsion [86], co-precipitation [87], hydrolysis and thermolysis [88]. Co-precipitation is a chemical reaction of Fe^{2+} and Fe^{3+} salts in alkaline media to result in MNPs (Fe_2O_3). Co-precipitation allows for easy of control over the desired nanoparticle properties (surface chemistry, size and shape) by controlling the ratio of iron salts with reaction condition [87,89], hence the MNPs used in this work where synthesized using co-precipitation method.

Spherically shaped amino functionalized MNPs (AMNPs) were synthesized and used as nanocarrier platforms for loading of MPcs for PDT applications. An advantage of designing such a platform is that the magnetic properties can be used to guide the therapeutic agent to the tumour site with an aid of an external magnetic field [90]. Additionally, the nano size drug system can easily permeate onto the tumour cells through the leaky blood vessels by EPR effect [38,39].

1.5.2 Silver nanoparticles.

Silver nanoparticles (AgNPs) are metal nanoparticles that exhibit optical, chemical and biological properties that can be harnessed for biological applications [91]. They are predominantly used as drug loading platforms in therapeutics [91,92]. In cancer therapy, a proper control and consideration of the size and shape of nanoparticles, the charge, surface properties and toxicological effects of nanoparticle is critical to overcome the difficulties imposed by treating cancer at a molecular level [91,92].

The AgNPs surface easily oxidizes and releases Ag^{+} ions at ambient conditions making AgNPs unstable and toxic [91,93,94]. To improve the stability and minimize the toxicity of Ag+ ions of AgNPs, capping agents are introduced during the growth phase of AgNPs in synthesis [76], this process can also be used to control the size and shape of nanoparticles [95].

In this work, L-cysteine is used as a capping agent on spherically shaped AgNPs (cys-AgNPs). The nanoparticles are used as nanocarrier platforms for loading MPcs for application in PDT and PACT. Like MNPs, the nano drugs have an advantage of delivering the photosensitiser agents (MPcs) through EPR effect at the tumour site to improve the efficacy of PDT. In PACT, the antimicrobial properties [76] of AgNPs are used to improve the inactivation efficiency of bacteria. Hence this work employs AgNPs conjugated to MPcs to improve the photoinactivation of MPcs on bacteria. Additionally, the heavy atom Ag enhances ISC and improves singlet oxygen quantum yields of MPcs

1.6 PHOTOPHYSICAL AND PHOTOCHEMICAL PARAMETERS.

1.6.1 Background.

The study and determination of the photophysical and photochemical parameters of MPcs are fundamental for their use in various applications, more especially in PDT and PACT. The photophysicochemical properties of MPcs depend on their electronic properties at the photo-excited state, Fig 1.6. The Jablonski diagram [96] illustrates the physical changes that photo-excited MPcs can undergo. This work explores the transitions of excited MPcs through intersystem crossing to the triplet state. In the presence of molecular oxygen ($^3O_1$), energy from the excited triplet state can be transferred to the ground state molecular oxygen to generate singlet oxygen ($^1O_2$) which is particularly important for PDT and PACT.

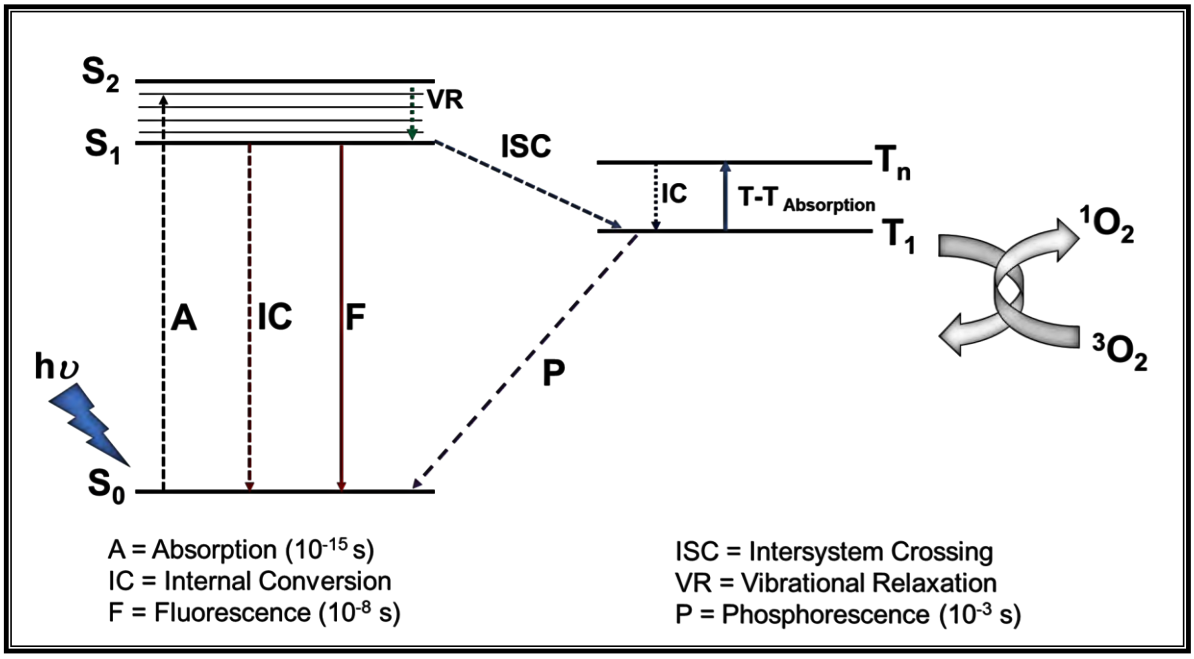

Fig 1.6. Jablonski diagram showing the electronic transitions between the singlet ground state (**S_0**) and the electronic excited states (**S_1** and **T_1**).

1.6.2 Fluorescence quantum yield and lifetimes.

Fluorescence quantum yield (Φ_F) is defined as the ratio of number of photons emitted to the number of photons absorbed. Φ_F can be determined by a comparative method [97] using equation 1.1.

$$\Phi_F = \Phi_{F\,(STD)} \cdot \frac{F.\ A_{STD}.n^2}{F_{STD}.A.\ n_{STD}^2} \quad \text{1.1}$$

where $\Phi_{F\,(STD)}$ is the fluorescence quantum yield of ZnPc standard ($\Phi_{F\,(STD)} = 0.20$) [98] , F and F_{STD} are the areas under the fluorescence emission curves of the sample (MPcs) and the standard, respectively. A and A_{STD} are the absorbances of the sample and the standard at the excitation wavelength, respectively. n and n_{STD} refers to the refractive indices of the solvents used for the sample and the standard, respectively.

Fluorescence lifetime (τ_F) is the average time a molecule spends in its excited singlet state before transitioning to the ground state through fluorescence. Time correlated single photon counting (TCSPC) is a technique that is used to measure the τ_F, and was used in this study. Fluorescence lifetimes of phthalocyanines are in the order of less than 10 ns. A typical fluorescence decay curve of MPc is solution is shown in Fig 1.7 [99].

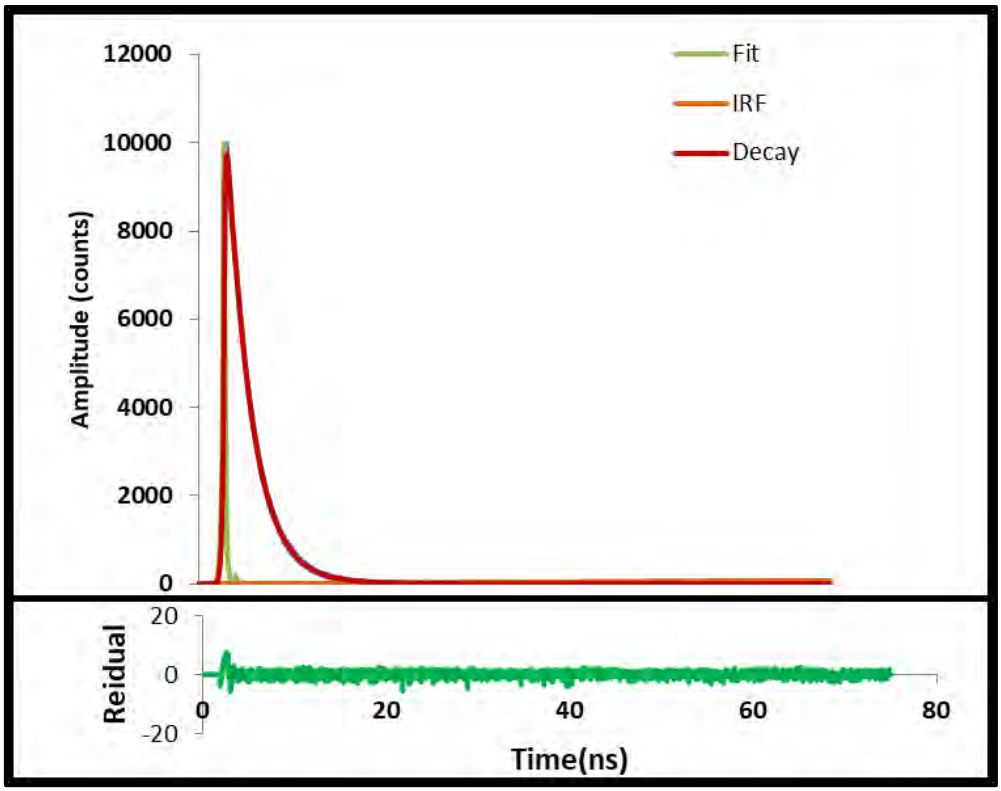

Fig 1.7. Fluorescence decay curve of a typical MPc in solution [99].

1.6.3 Triplet quantum yield and lifetimes

Laser flash photolysis is a technique that is used to study the properties of the molecule in the triplet excited state. An intense pulse of light from the laser is introduced into the sample to generate time-evolved electronic absorption from the T_1 -T_n state, from which the time spent (τ_T) and the population (Φ_T) of the triplet state can be calculated [100,101].

The triplet quantum yield (Φ_T) is used to determine the efficiency of the molecule to populate the triplet state. Triplet quantum yields can be determined from equation 1.2.

$$\Phi_T = \Phi_T^{STD} . \frac{\Delta A_T . \mathcal{E}_T^{STD}}{\Delta A_T^{STD} . \mathcal{E}_T} \quad \ldots\ldots\ldots\ldots\ldots\ldots\ldots\ldots\ldots\ldots\ldots\ldots \quad 1.2$$

where Φ_T^{STD} is the triplet quantum yield of unsubstituted ZnPc standard (Φ_T^{STD} = 0.65 in DMSO) [100], ΔA_T and ΔA_T^{STD} are the changes in the triplet state absorbances of the sample and the standard, respectively. $\mathcal{E}_T$ and $\mathcal{E}_T^{STD}$ are the triplet state molar extinction coefficients for the sample and the standard, respectively. $\mathcal{E}_T$ and $\mathcal{E}_T^{STD}$ can be calculated from the equations 1.3 A and 1.3 B.

$$\varepsilon_T = \varepsilon_S . \frac{\Delta A_T}{\Delta A_S} \quad \ldots\ldots\ldots\ldots\ldots\ldots\ldots\ldots\ldots\ldots\ldots\ldots\ldots\ldots\ldots\ldots \quad 1.3A$$

$$\varepsilon_T^{STD} = \varepsilon_S^{STD} \frac{A_T^{STD}}{A_S^{STD}} \quad \ldots\ldots\ldots\ldots\ldots\ldots\ldots\ldots\ldots\ldots\ldots\ldots\ldots\ldots\ldots\ldots\ldots\ldots \quad 1.3B$$

where $\mathcal{E}_S$ and ε_S^{STD} are the ground state molar extinction coefficients for the sample and the standard, respectively and ΔA_S and ΔA_S^{STD} are the changes in the ground state absorbances of the sample and the standard, respectively.

The triplet lifetime (τ_T) is an average time an excited MPc molecule remains in the T_1 state. The molecule is long-lived in the triplet state due to the forbidden T_1-S_0 transitions. τ_T of an MPc molecule can be obtained by fitting the triplet decay curve using OriginPro software, this method was used to obtain τ_T of complexes under study. A typical triplet decay curve is shown in Fig 1.8 [99].

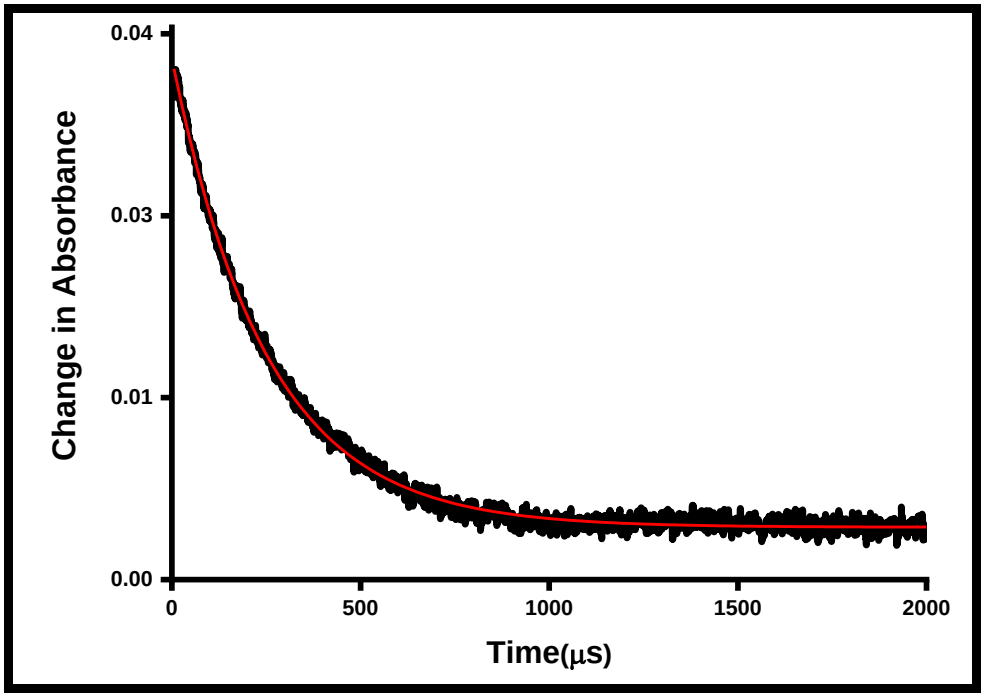

Fig 1.8. Triplet decay curve of a typical MPc in solution [99].

1.6.4 Singlet oxygen quantum yields.

Singlet oxygen quantum yield (Φ_Δ) is defined as the number of singlet oxygen molecules produced per quanta of light absorbed. The determination of Φ_Δ is important in the application of MPcs as photosensitizer in fields such as PDT and PACT. A relative method of comparing the Φ_Δ of the sample to that of the standard with a known Φ_Δ can be used. Two methods can be used for the determination of Φ_Δ, the chemical method and the singlet oxygen luminescence method. The former was used in this work; hence it is further discussed below.

The chemical method involves the use of a singlet oxygen quencher such as 1,3-diphenylsobenzofural (DPBF), 1,4-diazabicyclo-octane (DABCO), tetrasodium α, α-(anthracene-9,10-diyl) dimethylmalonate (ADMA) and sodium azide (NaN_3). ADMA and NaN_3 are commonly used in aqueous conditions while DBPF and DABCO are used in organic solvents [102,103].

Spectroscopic methods are then used to monitor the production of singlet oxygen through the decay of the quencher over a period. In this work, DPBF and ADMA were used as singlet oxygen scavengers for complexes soluble in organic solvents and aqueous solutions, respectively. Equation 1.4 is used to calculate the Φ_Δ of complexes.

$$\Phi_\Delta = \Phi_\Delta^{STD} . \frac{R^{sample} . I^{STD}}{R^{STD} . I^{Sample}} \quad \text{..... 1.4}$$

where Φ_Δ^{STD} is the singlet oxygen quantum yield of the standard (Φ_Δ^{STD} = 0.67 for unsubstituted ZnPc in DMSO [104] and $\Phi_\triangle^{std}$ = 0.34 for $AlPcS_{mix}$ in aqueous media [105]), R^{sample} and R^{STD} are the DPBF photobleaching rates in the presence of the sample under investigation and the standard, respectively. I^{Sample} and I^{STD} are the rates of light absorption by the sample and the standard, respectively.

1.7 SUMMARY OF AIMS OF THIS THESIS.

The aims of this thesis can be summarized as follows.

1. To synthesize and characterize symmetrical and asymmetric MPc derivatives (Zn and In) alone and conjugate them to folic acid, magnetic nanoparticles and silver nanoparticles.

2. To study the electronic absorptions and fluorescence spectroscopy of MPc derivatives and their conjugates.

3. To study and compare the photophysical and photochemical properties (fluorescence quantum yield and lifetimes, triplet quantum yield and lifetimes and the singlet quantum yield) of MPc derivatives and their conjugates.

4. To study the cytotoxic efficiency of MPc derivatives with their respective conjugates on MCF-7 cells through PDT or on *S. aureus* through PACT.

5. To study and compare the effect of metal nanoparticles, substituents, and symmetry of MPc derivatives on the photophysical and photochemical properties and their PACT or PDT activity.

6. To study the effect and PDT efficacy of active targeting using MPc-FA conjugates as compared to passive targeting using MPc-NPs conjugates on MCF-7 cells.

CHAPTER 2

EXPERIMENTAL PROCEDURE

This chapter outlines the materials and methods that were used for the synthesis and characterization of MPcs and their conjugates. The chapter also covers the procedures followed for cytotoxicity studies using PACT and PDT.

2.1 MATERIALS.

2.1.1 Solvents.

Absolute ethanol, methanol, dimethyl sulfoxide (DMSO), dimethylformamide (DMF) were purchased from SAARChem®. Dichloromethane (DCM) was purchased from B & M Scientific®. Acetonitrile was purchased from Merck®. 1-Pentanol, propanol, hydrochloric acid, ethyl acetate, 25% ammonium solution, acetic acid, tetrahydrofuran (THF), 2',5' dihydroxy acetophenone (used as a MALDI-TOF matrix), deuterated chloroform ($CDCl_3$) and deuterated dimethyl sulfoxide (DMSO-d_6) were purchased from Sigma–Aldrich.

2.1.2 Reagents.

2.1.2.1 Synthesis and characterization of MPcs.

Zinc (II) chloride, zinc (II) acetate, indium (III) chloride, 1, 8-diazabicyclo [5.4.0] undec-7-ene (DBU) were purchased from Fluka. Potassium carbonate, dimethyl amino ethanol (DMAE) and potassium hydroxide pellets were purchased from Sigma Aldrich. 4-nitrophthalonitrile (**8**) [106] was synthesized before. Methyl 4-hydroxybenzoate (**9a**), para-hydroxycinnamic acid (**10a**), 4-(*tert*-butyl) phthalonitrile (**11**) and dicyanobenzene (**12**) were purchased from Sigma Aldrich. 4-(4-*tert*-butyl phenoxy) phthalonitrile (**13**) [107] and zinc (II) 2-mono-(carboxyphenoxy) phthalocyanine (ZnMCPPc) (**2**) [83] were synthesized as reported before.

2.1.2.2 Synthesis of metal nanoparticles.

Iron (III) chloride, iron (II) sulphate, trisodium acetate, tetraethylorthosilicate (TEOS), (3-aminopropyl) triethoxysilane (APTES), L-cysteine, diphenyl ether, oleylamine (OLM), oleic acid (OA), silver acetate ($AgC_2H_3O_2$) were purchased from Sigma Aldrich.

2.1.2.3 Conjugation reactions.

N, N'- dicyclohexylcarbodiimide (DCC), *N*-hydroxysuccinimide (NHS) and 4- (di-methyl amino) pyridine (DMAP) were purchased from Sigma–Aldrich. Folic acid (FA) was purchased from SAARChem®

2.1.2.4 Cytotoxicity testing in PACT and PDT.

Human breast adenocarcinoma cell cultures (MCF–7 cells) were procured from Cellonex®. Dulbecco modified eagle's medium (DMEM) and Dulbecco phosphate-buffer saline (DPBS) were purchased from Lonza®. Heat-inactivated fetal bovine serum (FBS) and 100 unit/mL penicillin-100 µg/mL streptomycin-amphotericin B were obtained from Biowest®. WST1 cell proliferation neutral red reagent (Roche®) was purchased from Sigma–Aldrich. *S. aureus* (ATCC 25923) was purchased from Davies Diagnostics, South Africa. Phosphate buffer saline (PBS) of pH 7.4 was prepared using appropriate amounts of disodium phosphate (Na_2HPO_4) and sodium hydroxide (NaOH) in ultra-pure water using Type II water from an Elga purelab Chorus 2 (RO/DI) system.

2.1.2.5 Singlet oxygen determination.

Anthracene-9,10-bis-methylmalonate (ADMA) and 1,3-diphenylisobenzofuran (DPBF) were purchased from Sigma Aldrich®. AlPcSmix (containing a mixture of sulfonated Pc derivatives and used as a standard for singlet oxygen quantum yields (in aqueous media) was synthesized according to reported method [108]. Unsubstituted ZnPc was synthesized from cyclotetramerization of dicyanobenzene and was used as a standard for photochemical and photophysical studies of complexes in DMSO.

2.2 EQUIPMENT.

1. The ground state electronic absorption was measured using Shimadzu® Uv-2550 spectrophotometer.

2. Fluorescence excitation and emission spectra were collected on a Varian Eclipse® spectrofluorometer. All samples and the standard (ZnPc) were excited at the same wavelength (crossover). The absorbances at the vibrionic band of the samples and the standard were prepared to ≈0.05 to avoid any filter effects

3. Bruker® Alpha FT-IR spectrophotometer with universal attenuated total reflectance (ATR) was used to measure FT-IR spectra.

4. Bruker® Autoflex III smartbeam TOF/TOF mass spectrophotometer was used to collect mass spectra data using 2 ,5 dihydroxy acetophenone as a matrix.

5. Elemental analysis (CHNS microanalysis) were recorded using the Vario-Elementar® Microcube ELIII.

6. Time correlated single photon counting (TCSPC) setup (FluoTime 300, Picoquant GmbH) was used for the fluorescence decay studies, Fig 2.1. The excitation source was a diode laser (LDH-P-670 driven by PDL 800-B, 670 nm, 20 MHz repetition rate, 44 ps pulse width, Picoquant GmbH).

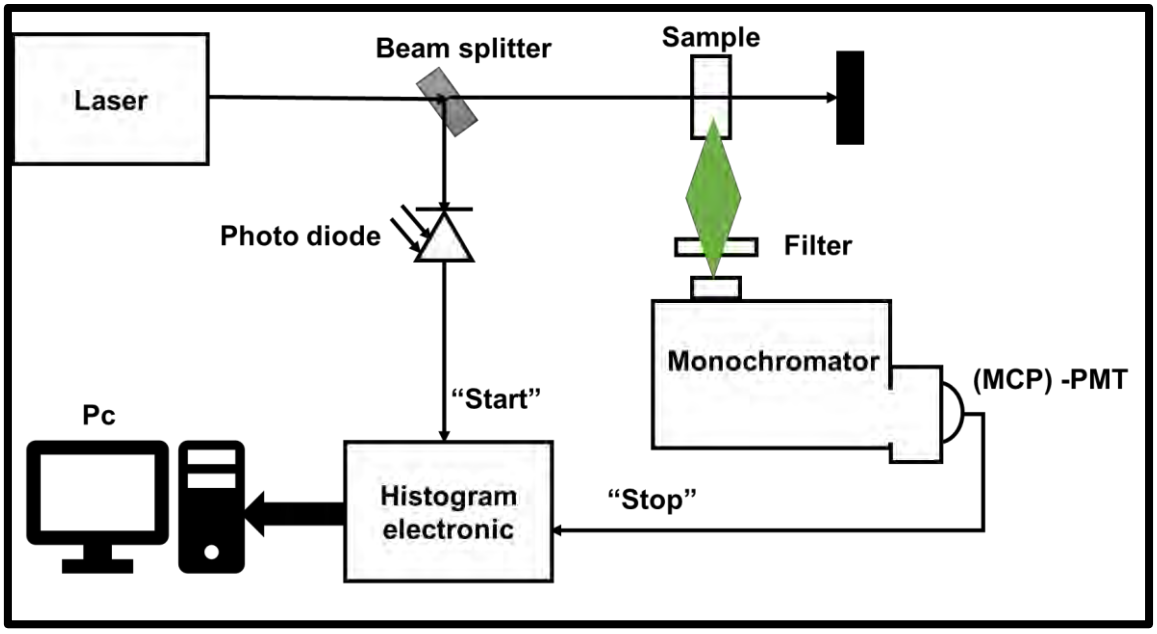

Fig 2.1. Schematic representation of the time-correlated single photon counting (TCSPC) set-up. (MCP)-PMT = (multi-channel plate detector)-photomultiplier tube.

7. Triplet quantum yields were determined using laser flash photolysis system, Fig 2.2. The excitation pulses were produced using a tunable laser system consisting of an Nd: YAG laser (355 nm, 135 mJ/4-6 ns) pumping an optical parametric oscillator (OPO, 30 mJ/ 3-5 ns) with a wavelength range of 420-2300 nm (NT-342B, Ekspla). In some studies, LP980 spectrometer with a PMT-LP detector and an ICCD camera (Andor DH320T-25F03) was used to obtain triplet quantum yields. The signal from a PMT detector was recorded on a Tektronix TDS3012C digital storage oscilloscope. The absorbances of samples and ZnPc standard solutions were ~1.5 at the Q-band. The solution was then introduced into a spectrophotometer cell of 1 cm path length and de-aerated using argon for 15 min. The fitting of triplet lifetimes was determined by exponential fitting of the kinetic curve using OriginPro® 8 software.

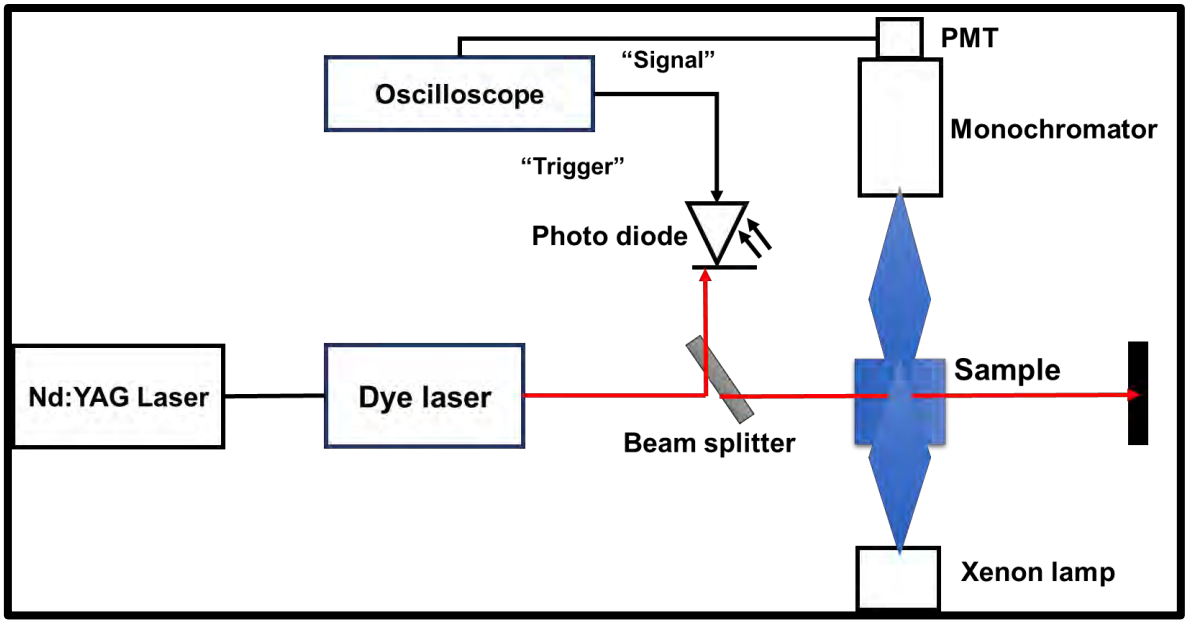

Fig 2.2. Schematic representation of a laser flash photolysis set-up. PMT= Photomultiplier tube.

8. Dynamic light scattering (DLS) experiments were conducted on a Malvern® Zetasizer Nanoseries, Nano-ZS90.

9. Singlet oxygen quantum yield studies were carried out using irradiation from a halogen lamp (300 W), 600 nm glass (Schott) and water were used to filter off ultra-violet and far infrared radiation respectively, Fig 2.3. An interference filter (Intor, 670 nm with bandwidth of 40 nm) was placed in the light path just before the reaction of the sample. Light intensities were measured with a POWER MAX 5100 (Molelectron detector incorporated) power meter. A chemical method was used for the determination of Φ_{Δ}. The samples or ZnPc standard with an absorbance of ~1.5 at the Q-band were mixed with the photobleaching agent (DPBF or ADMA) at a ratio of 1:1. The rate of degradation of the photobleaching agent was used to calculate the singlet oxygen quantum yields using equation 1.4.

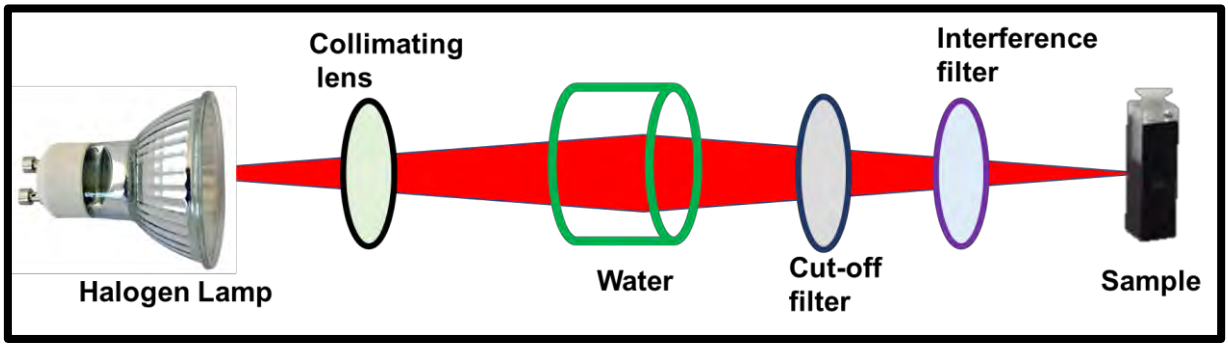

Fig 2.3. Schematic representation of a photo-irradiation set-up for singlet oxygen determination.

10. Bruker® AMX 300 and Bruker® AVANCE 600 MHz Hz NMR spectrometers were used to measure the proton (^{1}H) NMR spectra.

11. Transmission electron microscope (TEM) images were obtained using a JEOL TEM 1210 transmission electron micro- scope at 100 kV accelerating voltage.

12. Energy dispersive X-ray spectroscopy (EDX), INCA PENTA FET coupled to the VAGA TESCAM operated at 20 kV accelerating voltage was used to obtain the elemental compositions of metal nanoparticles and the nanoconjugates.

13. X-ray powder diffraction (XRD) patterns were recorded on a Bruker® D8 Discover equipped with a Lynx Eye detector, using Cu K α-radiation (l = 1.5405 Å, nickel filter).

14. The optical densities of the bacteria culture were determined using the LEDETECT 96 from LABXIM PRODUCTS.

15. Scan® 500 automatic color colony counter was used to evaluate the colony forming units (CFU)/mL of the bacteria.

16. Zeiss® Axiovert.A1 Fluorescence LED (FL-LED) inverted microscope was used to view MCF-7 adenocarcinoma breast cancer cells under phase contrast.

17. BioTek® Synergy 2 multi-mode microplate reader was used to measure the viable cells containing WST-1 cell proliferation neutral red reagent (Roche®)

18. Vortex mixer and HERMLE Z233M-2 centrifuge from LASIEC were used to mix the bacteria/fungus suspension and for the harvesting of the bacteria/fungus cells, respectively.

19. The Modulight ML7710-680-RHO laser system (680 wavelength probe) was employed for PDT and PACT studies. Modulight® Medical Laser System (MLS) 7710-680 channel Turnkey laser system coupled with a 2 x 3 W channel at 680 nm, cylindrical out-put channels, aiming beam, integrated calibration module, foot/hand switch pedal, sub-miniature version A connectors, and safety interlocks.

20. HealForce® humidified atmosphere incubator with ~5% CO_2 and a physiological temperature of 37 °C was used to culture MCF-7 cells.

2.3 SYNTHESIS

2.3.1 Phthalonitriles, Scheme 3.1.

Phthalonitrile derivatives were synthesized by base catalyzed nucleophilic nitro displacement of nitro group from 4-nitrophthalonitrile (**8**) with hydroxyl containing compound **9a** and **10a** (Scheme 3.1). All reactions were carried out at room temperature under an inert gas with constant stirring. Typically, compound **9** was synthesized from a reaction of **8** (3.0 g, 0.017 mol) and **9a** (2.64 g, 0.017 mol) in the presence of dry K_2CO_3 (3.52 g, 0.026 mol) in dry DMSO (20 mL) for 48 h to yield 3.58 g (75% yield) of compound **9** (methyl 4-(3,4-dicyanophenoxy) benzoate). Compound **10** (4-(3,4-dicyanophenoxy) cinnamic acid) was synthesized by reacting **8** (2.01 g, 0.011 mol) and **10a** (1.89 g, 0.011 mol) in the presence of dry K_2CO_3 (1.50 g, 0.010 mol) in dry DMSO (20 mL) for 48 h to yield 2.18 g (67% yield) of **10**. Compound **9** was washed and precipitated out of the reaction mixture by propanol and finally recrystallized twice with hot methanol. Compound **10** was precipitated using ice water containing few drops of hydrochloric acid. The precipitate was filtered, washed with water, and recrystallized twice with methanol.

9, Yield = 75%. IR (ATR): 2230 cm^{-1} (C≡N), 2959, 3079 cm^{-1} (C-H), 1710 cm^{-1} (C=O), 1240 cm^{-1} (Ar-O-Ar). ^1H NMR (300 MHz, $CDCl_3$) δ 7.71 (d, *J* = 8.7 Hz, 2H, Ar-H), 7.42 – 7.11 (m, 4H, Subs-Ar-H), 6.88 (s, 1H, Ar-H), 2.11 (s, 3H, $-CH_3$). Calcd for $C_{16}H_{10}N_2O_3$: C (69.06); H (3.62); N (10.07); Found C (68.34); H (3.05); N (11.02).

10, Yield: 67%. FTIR (ATR), cm^{-1}. 3302 (Carboxylic OH), 3060 (Ar-H), 2232 (C≡N), 1705 (C=O), 1622 (C=C), 1589 (Ar-C=C), 1253 (Ar-O-Ar). ^{1}H NMR (300 MHz, DMSO-d_6) δ 12.46 (s, 1H, -OH), 7.81 (d, *J* = 1.0 Hz, 2H, C=C-H), 7.48 (dd, *J* = 8.05, 3.24 Hz, 4H, Ar-H), 7.42 (d, *J* = 1.0 Hz, 2H, Ar-H), 7.21 (s, 1H, Ar-H). Calcd for $C_{17}H_{10}N_2O_3$: C (70.34), H (3.47), N (9.65); Found C (69.55), H (3.63), N (9.22).

2.3.2 Metallophthalocyanines.

Different synthetic methods, chemicals and solvents were used due to availability of reagents and solvents. A higher range of mole ratios for the second phthalonitrile to the target phthalonitrile were used for the synthesis of asymmetric MPcs to improve the yield of the desired MPc.

2.3.2.1 Zinc (II) tris-(*tert*-butyl) – 2-(carboxy phenoxy) phthalocyanine, Scheme 3.2.

Mixed condensation reaction involving two phthalonitriles (**9** and **11**) was used to achieve the desired asymmetrical ZnPcs, Scheme 3.2. In a typical synthesis of **1Me**, **11** (460.0 mg, 2.5 mmol) was reacted with **9** (440.0 mg, 1.5 mmol) in a glass tube reactor containing dry dimethyl amino ethanol (1 mL) and dry zinc acetate (150.0 mg, 8.0 mmol), Scheme 3.2A. The reaction was carried out at 160 °C in an argon atmosphere for 7 h with constant stirring. Silica packed column chromatography using 2% methanol in dichloromethane as eluting solvent mixture, were used to separate **1Me** (yield 62.28 mg) from a mixture of ZnPcs. Hydrolysis of **1Me** to yield mono functionalized carboxylic acid ZnPc (**1**) was achieved by reacting 50 mg of **1Me** with 3 M KOH in dry tetrahydrofuran (2 mL) and methanol (2 mL) for 24 h at 70

°C, Scheme 3.2 B. The product (**1**) was then precipitated and filtered out of the reaction mixture by adding few drops of acetic acid and excess amounts of water to yield 26 mg (52%) of **1**.

1Me, Yield = 11%. Uv/Vis (DMSO) λ_{max} / nm (Log ε): 676(5.02), 610(4.41), 351(4.73). IR (ATR): 2963 cm^{-1} (C-H), 1711 cm^{-1} (C=O), 1493 cm^{-1} (Ar-C=C), 1242 cm^{-1} (C-N). 1H NMR (600 MHz, DMSO-d_6) δ 8.31 (d, *J* = 2.0 Hz, 6H, Pc-Ar), 7.71 (s, 3H, Pc-Ar), 8.02 (s, 1H, Pc-Ar), 7.29 (d, *J* = 2.3 Hz, 2H, Pc-Ar), 7.62 (d, *J*=2.8 Hz, 2H, subs-Ar), 7.32 (d, *J* = 1.8 Hz, 2H, subs-Ar), 3.75 (s, 3H, -OCH_3), 1.78 (s, 27H, -CH_3). MALDI-TOF MS (m/z): Calcd 944.49; Found 940 $[M - 4H]^-$. Calcd for $C_{52}H_{46}N_8O_3Zn$: C (69.68); H (5.17); N (12.50); Found C (69.31); H (5.05); N (13.30).

1, Yield = 52%. Uv/Vis (DMSO) λ_{max} / nm (Log ε): 677 (4.71), 611 (4.32),352 (3.99).IR (ATR): 3310 cm^{-1} (OH), 2961 cm^{-1} (C-H), 1708 cm^{-1} (C=O), 1497 cm^{-1} (Ar-C=C), 1236 cm^{-1} (C-N).^{1}H NMR (600 MHz, DMSO-d_6) δ 9.10 (s, 1H, -OH), 8.29 – 8.16 (m, 8H, Pc-Ar), 7.81 (s. 1H, Pc-Ar), 7.97 (s, 3H, Pc-Ar), 7.53 (dd, *J* = 8.3, 2.2 Hz, 4H, subs-Ar), 1.75 (s, 27H, -CH_3). MALDI-TOF MS (m/z): Calcd 930.46: Found 931 $[M + 1H]^+$. Calcd for $C_{51}H_{44}N_8O_3Zn$: C (69.42); H (5.03); N (12.70); Found C (68.83); H (5.46); N (11.22).

2.3.2.2 Zinc (II) 2-mono-(4-oxy cinnamic acid) phthalocyanine, Scheme 3.3.

Synthesis of **3** was carried out by using mixed condensation of **10** (435.0 mg, 1.5 mmol) and **12** (320.0 mg, 2.5 mmol) in the presence of zinc chloride (200.0 mg,1.5 mmol) in 1-pentanol (2 mL), Scheme 3.3. The reaction was carried at 160 °C for 7 h catalyzed with few drops of DBU. The desired product (**3**) was separated from the

mixture by extensive column chromatography with silica as a stationary phase and 5% methanol in tetrahydrofuran as eluting solvent mixture.

3, Yield = 17%, Uv/Vis (DMSO) λ_{max} / nm (Log ε): 675 (5.54), 608 (4.77), 352 (5.01). IR (ATR): 3090 (Carboxylic O-H), 1712 (Carboxylic C=O), 1475 (Ar-C=C), 1661 (C=C), 1233 (C-N). ^{1}H NMR (600 MHz, DMSO-d_6) δ 12.45 (s, 1H, OH), 8.13 (d, J = 8.8 Hz, 2H, Pc–Ar), 7.91–7.77 (m, 8H, Pc–Ar), 7.62 (d, J = 16.0 Hz, 2H, Pc–Ar), 7.50–7.43 (m, 3H, Pc–Ar), 7.22 (dd, J = 8.7,4.3 Hz, 4H, Subs-Ar), 6.57 (s, 1H,-C=C), 6.51 (s, 1H, -C=C). MALDI-TOF MS (m/z): Calcd: 740, Found: 742 $[M + 2H]^{+}$ $^{-}$. Calcd for $C_{41}H_{22}N_8O_3Zn$: C (66.54), H (3.00), N (15.14): Found C (65.48), H (3.13), N (14.56).

2.3.2.3 Zinc (II) tris-(*tert-butyl*)-2-(4-oxy cinnamic acid) phthalocyanine, Scheme 3.4.

Complex **4** was synthesized from a reaction of **10** (250.0 mg, 0.86 mmol) and **11** (650.0 mg, 3.52 mmol) in the presence of zinc chloride (200.0 mg, 1.47 mmol) in 1-pentanol (2 mL), Scheme 3.4. The reactants were left stirring for 1 h at room temperature to allow homogenous mixing before adding few drops of DBU and setting the reaction temperature to 160 °C, followed by stirring for 7 h. The products were precipitated out of the reaction mixture by centrifugation in ethyl acetate and hexane. The desired product was then separated and purified on silica packed column chromatography with 1% methanol in dichloromethane as eluting solvent mixture.

4, Yield: 17%. Uv/Vis λ_{max}/ nm (log ε), DMSO. 678 (5.2). 611 (4.3). 351 (4.7). FTIR (ATR), cm^{-1}: 3075 (Carboxylic O-H), 1710 (Carboxylic C=O), 1488 (Ar-C=C), 1604 (C=C), 1235 (Ar-O-Ar). ^{1}H NMR (600 MHz, DMSO-d_6) δ 12.95 (s, 1H, Pc-COOH), 8.42 – 8.10 (m, 4H, Pc-Ar), 7.87 – 7.51 (m, 8H, Pc-Ar), 7.38 (s, 1H, Subs -C-H), 7.22 (d, *J* = 7.8 Hz, 2H, Subs-Ar), 7.15 (d, *J* = 7.0 Hz, 2H, Subs-Ar), 7.01 (s, 1H, Subs-C-H), 1.35 (s, 27H, *tert*-butyl). MALDI-TOF MS (*m/z*): Calc: 908.38 Found 908.45 [M]. Calc for $C_{53}H_{46}N_8O_3Zn$: C (70.08), H (5.10), N (12.34). Found C (70.34), H (5.83), N (11.33).

2.3.2.4 Zinc (II) tris-(4-*tert*-butyl phenoxy)-2- (4-oxycinnamic acid) phthalocyanine, Scheme 3.5.

Complex **5** was synthesized by reacting **10** (250.0 mg, 0.86 mmol) and **13** (580.00 mg, 2.49 mmol) in the presence of zinc chloride (120.0 mg, 0.86 mmol) in 1-pentanol (2 mL), Scheme 3.5. Few drops of DBU were added and the reaction was set at 160 °C with continuous stirring for 7 h. The product was washed and precipitated out of the reaction mixture with continuous centrifuge in methanol, ethyl acetate and acetonitrile. Silica packed column chromatography with 10% methanol in dichloromethane as mobile phase (eluting solvent mixture) was then used to separate and purify the desired product (complex **5**) from a mixture of MPcs.

5, Yield: 15%. Uv/ Vis λ_{max}/ nm. 682 (5.3), 614 (4.5), 352 (4.8). FTIR (ATR) cm^{-1}: 3061 (Carboxylic O-H), 2949, 2859 (-CH_3), 1711 (Carboxylic C=O), 1486 (Ar-C=C), 1590 (Ar-C=C), 1229 (Ar-O-Ar). ^{1}H NMR (600 MHz, DMSO-d_6) δ 11.29 (s, 1H, Subs-COOH), 8.38 – 8.20 (m, 6H, Pc-Ar-H), 8.02 – 7.73 (m, 12H, Subs-Ar-H), 7.52 (dd, J = 23.0, 8.2 Hz, 4H, Subs-Ar-H), 7.48 – 7.33 (m, 6H, Pc-Ar-H), 7.13 (d, J = 6.8 Hz,

2H, Subs -C-H), 1.31 (s, 27H, *tert*-butyl). MALDI-TOF MS (*m/z*): Calc: 1185, found 1186 $[M+H]^+$. Calc for $C_{71}H_{58}N_8O_6Zn$: C (71.98), H (4.94), N (9.46). Found C (71.21), H (5.25), N (9.81).

2.3.2.5 Zinc (II) and indium (III) chloride 2(3), 9(10), 16(17), 23(24)-tetrakis-(4-oxy cinnamic acid) phthalocyanine, Scheme 3.6.

Zinc (II) (**6**) and indium (III) chloride (**7**) 2(3), 9(10), 16(17), 23(24)-tetrakis-(4-oxy cinnamic acid) phthalocyanines were synthesized from **10** (500.0 mg, 1.72 mmol) in separate round bottomed flasks containing 1-pentanol (3 mL) and metal salts, Scheme 3.6. Zinc chloride (200.0 mg, 1.47 mmol) was used for **6**, and indium chloride (200.0 mg, 0.90 mmol) for **7.** DBU (0.2 mL) was added and the reactions were left stirring while heating at 160 °C for 8 h to afford zinc (II) 2(3), 9(10), 16(17), 23(24)-tetrakis-(4-oxy cinnamic acid) phthalocyanine (ZnTCAPc, **6**) or indium (III) chloride 2(3), 9(10), 16(17), 23(24)-tetrakis-(4-oxy cinnamic acid) phthalocyanine (InTCAPc, **7**). After completion of the reactions, the products were precipitated out of the reaction mixture by centrifuging in methanol and repeatedly washed with ethanol, acetonitrile, acetone, 1 M hydrochloric acid and water. Silica packed column chromatography was used to purify MPcs with 10% methanol in tetrahydrofuran containing drops of acetic acid.

ZnTCAPc (**6**), Yield: 73%, Uv/Vis λ_{max}/nm (log ε). 679 (5.3), 613 (4.6), 355 (4.9). FTIR (ATR) cm^{-1}: 3045 (Carboxylic O-H), 1694 (Carboxylic C=O), 1497 (Ar-C=C), 1610 (C=C), 1232 (Ar-O-Ar). ^1H NMR (600 MHz, DMSO–d_6) δ 12.36 (s, 4H, -COOH), 8.73 (d, *J* = 130.1 Hz, 8H, Pc-Ar-H), 7.96 (s, 4H, Pc-Ar-H), 7.91 – 7.67 (m, 10H, Subs-Ar-H), 7.49 (d, *J* = 64.9 Hz, 6H, Subs-Ar-H), 6.88 (s, 2H, C=C-H), 6.75 –

6.38 (m, 6H, C=C-H). MALDI-TOF MS (*m/z*): Calc: 1226 Found 1225 $[M-H]^-$. Calc for $C_{68}H_{40}N_8O_{12}$: C (66.59), H (3.29), N (9.14). Found C (65.89), H (4.11), N (9.74). InTCAPc (**7**), Yield: 69%, Uv/Vis λ_{max}/ nm (log ε). 687 (5.2), 625 (4.6), 360 (5.0). FTIR (ATR) cm^{-1}: 3030 (Carboxylic O-H), 1712 (Carboxylic C=O), 1489 (Ar-C=C), 1628 (C=C), 1228 (Ar-O-Ar). ^1H NMR (600 MHz, DMSO-d_6) δ 12.31 (s, 4H, -COOH), 8.32 – 7.76 (m, 12H, Pc-Ar-H), 7.73 – 7.56 (m, 10H, Subs-Ar-H), 7.42 (dd, *J* = 87.5, 34.8 Hz, 4H, Subs-Ar-H), 7.26 (d, *J* = 24.9 Hz, 2H, Subs-Ar-H), 6.88 (s, 2H, C=C-H), 6.62 (d, *J* = 41.9 Hz, 6H, C=C-H). MALDI-TOF MS (*m/z*) Calc :1311 Found 1312 $[M + H]^+$. Calc for $C_{68}H_{40}N_8O_{12}.H_2O$: C (61.45), H (3.07), N (8.54). Found C (61.01), H (3.15), N (8.47).

2.4 SYNTHESIS OF NANOPARTICLES.

2.4.1 Magnetic nanoparticles.

2.4.1.1 Bare magnetic nanoparticles, Scheme 3.7.

Iron oxide magnetic nanoparticles (MNPs) were synthesized using the co-precipitation method as published in literature [73,109,110], Scheme 3.7. A mixture of $FeCl_3$ (650.0 mg, 4.0 mmol), $FeSO_4$ (320.0 mg, 2.0 mmol) and ultrapure water (45 mL) was stirred under inert gas at 70 °C for 15 min. 25% ammonium solution (5 mL) was then added dropwise and the mixture was left stirring for an additional 60 min. Trisodium acetate (0.3 M, 100 mL) was then added and the reaction temperature was raised to 90 °C for 30 min. The black precipitate was collected using a magnet and washed several times with ultrapure water before drying in an oven.

2.4.1.2 Silica-coated magnetic nanoparticles (SMNPs), Scheme 3.7.

The as synthesized MNPs (250 mg) were added to a mixture of methanol (150 mL) and ultrapure water (50 mL). The mixture was stirred for 15 min at room temperature followed by dropwise addition of 25% ammonium solution (3 mL) and tetraethylorthosilicate (TEOS) (2 mL). The mixture was left stirring for 24 h. The prepared SMNPs were washed with ultrapure water and dried in an oven. 50 mg of SMNPs were washed twice with ethanol and thrice with toluene

2.4.1.3 Amino coated magnetic nanoparticle (AMNPs), Scheme 3.7.

The washed SMNPs (50 mg) were stirred for 24 h in the presence of dry DMF (24 mL), toluene (16 mL) and APTES (2 mL) under inert gas. The prepared AMNPs were then washed with DMF and dried in oven.

2.4.2 Silver nanoparticles, Scheme 3.9.

The synthesis of L-cysteine functionalized silver nanoparticles was achieved using a previously reported method [51] with modification as follows, diphenyl ether (25 g, 0.15 mol) and silver acetate (0.3 g, 0.017 mol) were mixed in a round bottomed flask followed by addition of oleylamine (OLA, 8 mL) and oleic acid (OA, 4 mL), Scheme 3.9. The mixture was left stirring for 5 h at 160 °C under argon gas. L-cysteine (0.05 g, 0.42 mol) was then added to the reaction mixture, followed by stirring for a further 3 h at a lower temperature (100 °C). The L-cysteine capped silver nanoparticles (Cys-AgNPs) were precipitated and washed with ethanol few times before drying them in the oven overnight.

2.5 CONJUGATION OF METALLOPHTHALOCYANINES.

MPcs (**1**-**7**) reported in this study were covalently linked to folic acid, silver, and magnetic nanoparticles. MPcs **1** - **4**, **6** and **7** were linked to magnetic nanoparticles (AMNPs) through an amide bond and **3** - **6** were linked to silver nanoparticles (cys-AgNPs). MPcs **1** - **3** were chemically linked to folic acid while **1** and **2** were also physically mixed to folic acid. The covalent linking methods are outlines below.

2.5.1 Conjugation of MPcs to MNPs, Scheme 3.8.

Scheme 3.8 illustrates the amide bond linkage of **3** to AMNPs (as an example). Complex **3** (20 mg, 0.027 mmol), DCC (5.58 mg, 0.027 mmol) and NHS (4.35 mg, 0.037 mmol) were added to a round bottomed flask containing dry DMF (3 mL) to activate the carboxylic acid of MPcs. The solution was left stirring for 48 h at room temperature. Afterwards, amino functionalized magnetic nanoparticles (AMNPs) (20 mg) were added to the reaction mixture and left to stir for a further 72 h to afford an amide bond linkage between the MPcs carboxylic groups and the amino moieties of AMNPs. After the linkage, the conjugate was washed and precipitated out of the solution by repeated centrifugation in ethanol, ethyl acetate and methanol**.** The same method was used to conjugate MPcs **1**, **2**, **4**, **6** and **7** to AMNPs to result in **1**-AMNPs, **2**-AMNPs, **4**-AMNPs and **6**-AMNPs and **7**-AMNPs, respectively.

2.5.2 Conjugation of MPcs to AgNPs, Scheme 3.10.

Complex **5** (20 mg, 0.023 mmol) (as an example), DCC (8.4 mg, 0.040 mmol) and NHS (4.61 mg, 0.040 mmol) were reacted in dry DMF (3 mL) for 48 h at room temperature to allow activation of carboxylic acid group on MPcs, Scheme 3.10. After 48 h, Cys-AgNPs (20 mg) in dry DMF (2 mL) were added and the mixture was left stirring for a further 48 h to afford an amide bond between the NH_2 groups of cys-AgNPs and the carboxylic acid group of MPcs (**5**-cys-AgNPs). The same reaction conditions were used to link **3**, **4** and **6** to cys-AgNPs to yield **3**-cys-AgNPs, **4**-cys-AgNPs and **6**-cys-AgNPs, Scheme 3.10. The conjugates were precipitated and purified from the reaction mixture by centrifuging with DMF, twice with methanol and twice with ethanol.

2.5.3 Conjugation of MPcs to folic acid, Scheme 3.11.

The amide bond linkage of MPcs **1** - **3** to folic acid (FA) was achieved as follows: complex **3** (20 mg, 0.027 mmol) (as an example) was dissolved in dry DMF (3 mL) in a round bottomed flasks containing DCC (8.32 mg, 0.04 mmol) and DMAP (4.89 mg, 0.04 mmol), Scheme 3.11. The mixture was left stirring for 48 h in room temperature under nitrogen atmosphere to activate the carboxylic group of MPcs. After activation, FA (20 mg, 0.045 mmol) dissolved in dry DMF (2 mL) was added to the reaction mixture and stirred at room temperature for a further 5 days or until the reaction was complete (monitored with 10% ninhydrin solution). The same method was used to link MPcs **1** and **2** to FA to form **1**-FA and **2**-FA. The amide linked conjugates (**1**-FA, **2**-FA, and **3**-FA) were isolated by centrifugation and washed with

DCM and hexane (1:1). The partially water-soluble conjugates were further purified on a small column chromatography packed with silica using 10% methanol: 5% DMF in acetonitrile as an eluting solvent mixture, giving linked MPc-FA represented as **1**-FA, **2**-FA and **3**-FA. Complexes **1** and **2** were also physically mixed with FA without a chemical bond and are represented as **1**/FA and **2**/FA for **1** and **2**, respectively.

1-FA, Yield: 58%. IR (ATR): 3334 cm^{-1} (N-H Amide), 3095 cm^{-1} (FA-COOH), 1693 cm^{-1} (C=O), 1609 cm^{-1} (N-H spike). MALDI-TOF MS (m/z): Calcd: 1305, Found: 1304 $[M - 1H]^{-}$.^{1}H NMR (600 MHz, DMSO-d_6) δ 11.53 (s, 2H, FA-COOH), 8.65 (s, 1H, FA-NH), 8.28 (dd, J = 26.1, 6.8 Hz, 4H, FA-Ar), 8.06 (s, 1H, FA-Pt ring), 7.91 (m, 8H, Pc-Ar), 7.81 (dd, J = 12.3, 4.5 Hz, 4H, Pc-Subs-Ar), 7.62 (t, J = 6.3 Hz, 3H, Pc-Ar), 7.59 (s, 1H, FA-NH), 7.45 (s, 1H, FA-Ar-NH), 6.96 (s, 1H, FA-2° NH), 7.12 (s, 1H, Pc-Ar), 4.48 (d, J = 7.1 Hz, 2H, FA-CH) 4.31 (s, 1H, FA-CH), 2.04 – 1.85 (m, 4H, FA-CH_2),1.54 – 1.16 (m, 27H, Pc-CH_3). Anal Calcd for $C_{70}H_{61}N_{15}O_8Zn$. $2H_2O$: C (62.63); H (4.88); N (15.63); Found C (62.85); H (5.13); N (15.14).

2-FA, Yield: 63%. IR (ATR): 3310 cm^{-1} (N-H amide), 3093 cm^{-1} (FA-COOH), 1690 cm-1 (C=O), 1607 cm^{-1} (N-H Spike). MALDI-TOF MS (m/z): Calcd: 1137, Found: 1138 $[M + 1H]^{+}$.^{1}H NMR (600 MHz, DMSO-d_6) δ 11.67 (s, 2H, FA-COOH), 8.64 (d, J = 5.7 Hz, 2H, FA-NH), 8.28 (d, J = 7.3 Hz, 2H, Pc-Subs-Ar) 8.06 (d, J = 4.9 Hz, 2H, Pc-subs-Ar),7.91 (t, 3H, Pc-Ar), 7.84 (s, 1H, FA-Pt-Ring), 7.72 (m, 8H, Pc-Ar), 7.63 (dd, J = 17.9, 10.0 Hz, 4H,FA-Ar), 7.43 (dd, J = 11.1, 8.6 Hz, 4H,Pc-Ar), 7.08 (s, 1H, FA-Ar-NH), 6.94 (s, 1H, FA-2° NH), 4.47 (d, J = 6.0 Hz, 2H, FA-CH), 4.27 (s,

1H, FA-CH), 2.41 – 1.47 (m, 4H, FA-CH). Anal Calcd for $C_{58}H_{37}N_{15}O_8Zn$: C (61.25); H (3.28); N (18.47); Found C (60.51); H (3.05); N (19.14).

3-FA, Yield: 53%, IR (ATR): 1602 cm^{-1} (Amide -NH Spike), 1650 cm^{-1} (Amide C=O), 3330 cm^{-1}(1° Amide NH). MALDI-TOF MS (m/z): Calcd: 1163. Found: 1162 $[M - H]^-$. ^1H NMR (600 MHz, DMSO-d_6) δ 12.04 (s, 2H, FA-COOH), 9.42 (s, 1H, FA-Pt-NH), 8.67 (d, *J* = 4.5 Hz, 2H, FA-NH), 8.45 (s, 1H, FA-Pt-Ar), 8.27 – 8.21 (m, 6H, Pc-Ar), 7.77 – 7.71 (m, 8H, Pc-Ar), 7.67 (d, *J* = 8.8 Hz, 2H, FA-Ar), 7.12 (d, *J* = 8.2 Hz, 2H, FA-Ar), 7.62 (d, *J* = 8.4 Hz, 2H, Subs-Ar), 7.57 (d, *J* = 8.3 Hz, 2H, Subs-Ar), 6.91 (s, 1H, FA-2°-NH), 6.68 (d, *J* = 8.8 Hz, 2H, Subs-CH), 6.65 (s, 1H, Pc-Ar), 4.51 (s, 1H, FA-CH), 2.33 – 2.19 (m, 4H, FA-CH_2). 4.26 (d, *J* = 6.8 Hz, 2H, FA-CH_2). CHN analysis: $C_{60}H_{39}N_{15}O_8Zn.2H_2O$. Calcd: C (60.08), H (3.61), N (17.52). Found C (60. 79), H (3.16), N (16.89).

2.6 PHOTODYNAMIC THERAPY STUDIES

MPcs and conjugates were tested against MCF-7 breast cancer cells in triplicates as described in the literatures [51,111] with modifications. The cells were first cultured in a T-25 flask using Dulbecco's Modified Eagle's Medium (DMEM) containing 4.5 g/L glucose with L-glutamine and phenol red. DMEM was supplemented with 10% fetal bovine serum (FBS) and 5% penicillin-streptomycin amphotericin (PSA) and was used as culture media. The cells were further grown into a T-75 flask following 80% confluence and after trypsinization from T-25 flask. Following 80% confluence, cell growth in T-75 flask, the cells were trypsinised and counted using trypan blue dye exclusion assay (0.4% trypan blue solution) by hemacytometer.

The cells were seeded into 96–well tissue culture plates at cell density of 10000 cells/well in culture media with phenol red and placed in an incubator (operated at 37 °C and 5% CO_2) for 24 h to foster cell attachment to the wells. The incubated seeded cells were washed with DPBS and treated with 100 µL of the gradient concentrations ranging from 5 µg/mL to 80 µg/mL in 1.6% DMSO with culture media having phenol red. The treated cells in 96 well tissue culture grade microwell plates were further incubated for 24 h at 37 °C and 5% CO_2 in the dark. After 24 h treatment, the cells were washed with 100 µL DPBS and re-incubated in fresh culture media. Post treatment cell viability was measured using the cell proliferation neutral red reagent (WST-1 assay) on a Synergy 2 multi-mode microplate reader (BioTek®) at a wavelength of 450 nm.

The percent cell viability was determined as a function of absorbance sample over absorbance control (culture media only); both determined at 450 nm. This is described in equation 2.1.

$$\% \text{ Cell Viability} = \frac{\text{Absorbance of samples at 450 nm}}{\text{Absorbance of control at 450 nm}} \text{ x } 100 \quad \ldots\ldots\ldots\ldots\ldots\ldots\ldots\ldots \quad 2.1$$

The photodynamic therapy activities of MPcs and conjugates (PS agents) were investigated at a fixed irradiation dosimetry of 150 J/cm^2 and 170 J/cm^2. Two irradiation doses were used due to availability of the light source (Modulight), the doses were used at different sets of studies. Gradient concentrations were employed for the *in vitro* dark toxicity studies. The cells containing the administered MPcs and conjugates were incubated for 24 h at 37 °C and 5% CO_2. The incubated cells containing the MPcs and conjugates were washed with 100 µL of DPBS and replaced with phenol-red free culture media.

The plates were subsequently illuminated with the Modulight® illumination set up at a fixed dosimetry of 150 J/cm^2 or 170 J/cm^2. After treatment, the phenol red free supplemented media was replaced with supplemented media with phenol red. Cell viability was expressed as percentage of placebo cells (cells without PS agents). Surviving cells were quantified after re-incubation with culture media with the use of WST-1 assay after 24 h. The data obtained from the three independent (n=3) triplicated experiments was statistically analysed with a 3-way factorial analysis of variance (ANOVA) for the *in vitro* dark cytotoxicity and PDT data of complexes against MCF-7 cell was evaluated. A p–value < 0.05 was considered statistically significant.

2.7 PHOTODYNAMIC ANTIMICROBIAL CHEMOTHERAPY STUDIES.

Cultures of bacteria were prepared as previously reported [112]. Briefly, aliquots of the cultures were aseptically transferred to 4 mL of fresh broth and incubated at 37 °C to mid logarithmic phase (absorbance at 620 nm ≈ 0.6). The bacteria culture in the logarithmic phase of growth were harvested through the removal of broth culture by centrifugation (3000 RPM for 15 min), washed once with 10 mM of PBS and re-suspended in PBS (4 mL). Then the bacteria culture was diluted to 1/1000 in PBS (working stock solution), corresponding to ≈10^8 colony forming units (CFU)/mL.

PACT studies of *S. aureus* were performed using methods previously reported [113,114] using 2% DMSO in PBS. In all the experiments, the *S. aureus* suspension were incubated in an oven equipped with a shaker for 30 min in the dark at 37 °C. Then half (1 mL) of incubated *S. aureus* suspensions were irradiated at the Q-band maximum of photosensitizers in a 24 well plate, using the set-up described above while the other half was kept in the dark. After irradiation, 100 µL samples were serially diluted (10-fold) with PBS and were aseptically spotted on agar plates using micropipette. The plates were incubated inverted at 37 °C overnight for 24 h. PACT studies were conducted at various irradiation periods at 0.5W cm^{-2} irradiance, resulting in energy doses ranging from 0.9 kJ cm^{-2} to 3.6 kJ cm^{-2} corresponding to time periods ranging from 30 min to 120 min. The data obtained from the three independent (n=3) triplicated experiments was statistically analysed with a 3-way factorial analysis of variance (ANOVA) for the *in vitro* dark cytotoxicity and PACT data of MPcs and conjugates against *S. aureus* cell was evaluated. A p–value < 0.05 was considered statistically significant.

CHAPTER 3

SYNTHESIS AND CHARACTERIZATION

This chapter describes the synthesis and characterizations of novel phthalocyanines, nanoparticles and the covalent linkage of MPcs to folic acid, silver, and magnetic nanoparticle

PUBLICATIONS.

The results discussed in the following chapters have been presented in the articles below, that have been published in internationally peer reviewed journals. These articles have not been referenced in this thesis.

1. **G. G. Matlou**, N. Kobayashi, M. Kimura, T. Nyokong. Synthesis and photophysical studies of asymmetric zinc phthalocyanine-magnetic nanoparticle conjugates. New Journal of chemistry, ***2017***, 41, 12309-12318.
2. **G. G. Matlou**, N. Kobayashi, M. Kimura, T. Nyokong. Physicochemical properties of water soluble asymmetric phthalocyanines-folic acid conjugates. Dyes and Pigments, ***2018***, 148, 393-398.
3. **G.G. Matlou**, D.O Oluwole, E. Prinsloo, T. Nyokong. Photodynamic therapy activity of zinc phthalocyanine linked folic acid and magnetic nanoparticles. Journal of Photochemistry and Photobiology B: Biology. ***2018***, 186, 216-224.
4. **G.G. Matlou**, D.O Oluwole, T. Nyokong. Evaluation of the photosensitizing properties of zinc and indium tetra cinnamic acid phthalocyanines linked to magnetic nanoparticles on human breast adenocarcinoma cells. Journal of Luminescence, ***2019***, 205, 285-392.
5. **G.G. Matlou**, M. Managa, T. Nyokong. Effect of symmetry and metal nanoparticles on the photophysicochemical and photodynamic therapy of cinnamic acid zinc phthalocyanine. Spectrochimica Acta Part A: Molecular and Biomolecular Spectroscopy. ***2019***, 214, 59-57.

6. **G.G. Matlou**, T. Nyokong. Photophysico-chemical properties and photoinactivation of *Staphylococcus aureus* using zinc phthalocyanines linked silver nanoparticles conjugates. Dyes and Pigments, ***2020***,176, 108237

3.1 PHTHALONITRILES.

The synthesis of phthalonitrile **9** and **10** were achieved by base (dry K_2CO_3) catalyzed nucleophilic nitro displacement of nitro group from 4-nitrophthalonitrile (**8**) with hydroxyl containing compounds (**9a** for **9** and **10a** for **10**), Scheme 3.1. The reactions were carried out in an inert environment at room temperature with DMSO as a solvent.

The infrared spectra of compound **9** and **10** indicated the presence of the nitrile (C≡N) peaks at 2230 cm^{-1} and 2232 cm^{-1}, respectively. The carbonyl peaks (C=O) were observed at 1710 cm^{-1} for **9** and 1705 cm^{-1} for **10**. Ar-O-Ar stretch at 1240 cm^{-1} (**9**) and 1253 cm^{-1} (**10**) results from the ether bond between the two benzene rings and confirms the structures of **9** and **10**.

The ^1H NMR spectra for compounds **9** and **10** gave peaks between 6.88 ppm to 7.81 ppm resulting from the two aromatic rings. Complex **9** had a multiplet (7.42 – 7.11 ppm) which integrated into 4 protons from the phenoxy ring, a doublet at 7.71 ppm and a singlet at 6.88 ppm which integrated into two protons and a single proton, respectively, which completes the phthalonitrile phenyl ring. The methyl protons gave a singlet peak at 2.11 which integrated into 3 protons.

10 had a broad singlet peak at 12.46 ppm representative of carboxylic hydroxyl peak which integrated into a singlet proton. The cinnamic acid phenyl ring gave a doublet of a doublet at 7.48 ppm which integrated into 4 protons, while the unsaturated carbons gave a doublet peak at 7.42 ppm, which integrated to give 2 protons completing the protons on the cinnamic acid substituent. The phthalonitrile phenyl ring gave doublet peak at 7.81 ppm that integrated into 2 protons and a singlet at

7.21 ppm which integrated into a single proton which completes the protons of the second ring for **10**. The elemental analysis of both the phthalonitrile gave the values in agreement with analytically calculated values.

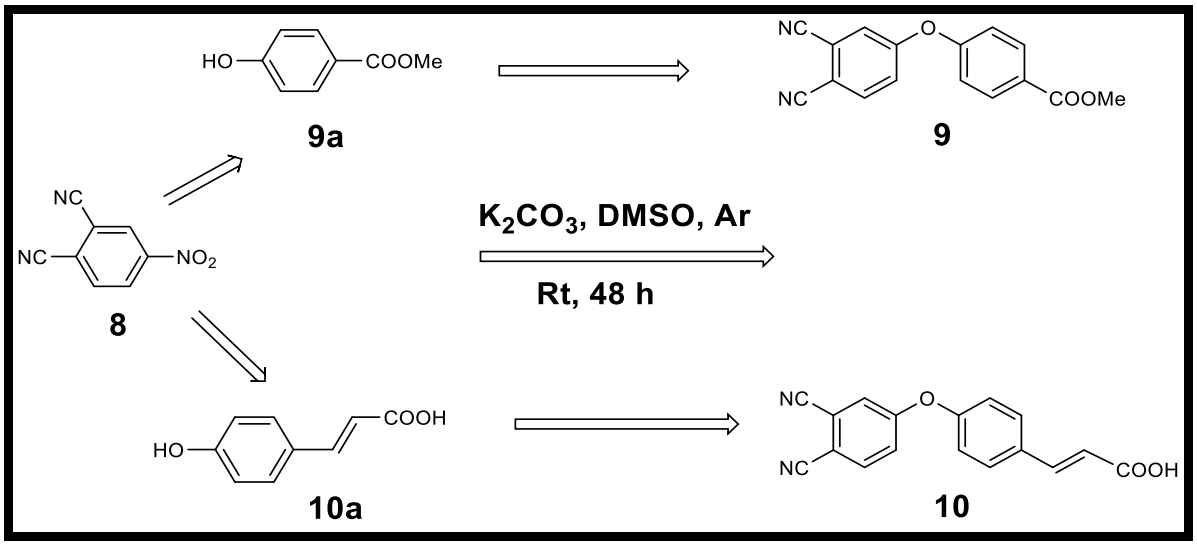

Scheme 3.1. Synthesis of methyl 4-(3,4-dicyanophenoxy) benzoate (**9**) and 4-(3,4-dicyanophenoxy) cinnamic acid (**10**).

3.2 METALLOPHTHALOCYANINES.

The following spectra were provided for illustrative purpose, ^{1}H NMR spectra for **3** and **6**, MALDI-TOF mass spectra for **4** and FTIR spectra for **3** and **4**.

3.2.1 Zinc (II) tris (*tert*-butyl) -2- (carboxy phenoxy) phthalocyanine.

The synthesis of complex **1Me** was achieved by mixed condensation reaction of methyl 4-(3,4-dicyanophenoxy) benzoate (**9**) and 4-(*tert*-butyl) phthalonitrile (**11**) in the presence of dimethyl amino ethane (DMAE) and zinc acetate, Scheme 3.2 A. The mole ratios of the phthalonitriles were 1.5 moles of **9** to 2.5 moles of **11**. Complex **1** was achieved by a hydrolysis reaction of **1Me** to replace the methoxy group with a hydroxyl group using 3 M KOH in the presence of methanol and tetrahydrofuran, Scheme 3.2B. All reactions were carried out under an inert environment.

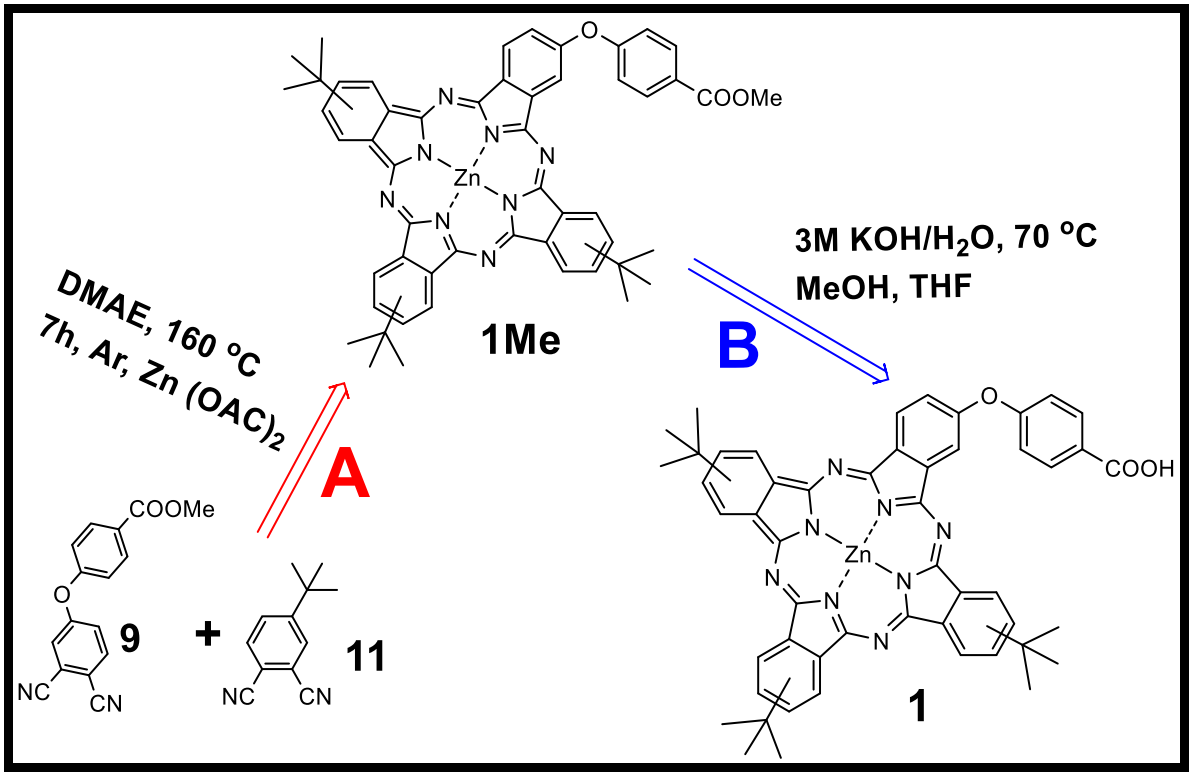

Scheme 3.2. Synthesis of zinc (II) tris-(*tert*-butyl)-2-(carboxy phenoxy) phthalocyanine.

FTIR spectra (figure not shown) of MPcs **1Me** and **1** indicated unsaturated (C-H) carbon vibrations at 2963 cm^{-1} for **1Me** and 2961 cm^{-1} for **1** which are representatives of *tert*-butyl substituents and the ester methyl group. The hydroxyl group of carboxylic acid was observed at 3310 cm^{-1} for **1** while the carbonyl carbons were observed at 1711 cm^{-1} and 1708 cm^{-1} for **1Me** and **1**, respectively. The Pc core IR peaks were indicated by the aromatic carbon-carbon (Ar-C=C) peaks at 1493 cm^{-1} for **1Me** and 1497 cm^{-1} for **1**, together with the carbon-nitrogen (C-N) peaks at 1242 cm^{-1} for **1Me** and 1236 cm^{-1} for **1**. The successful synthesis of MPcs **1Me** and **1** was also confirmed by an absence of C≡N peaks between 2230 cm^{-1} and 2240 cm^{-1} which represents phthalonitrile precursors.

^{1}H NMR of **1Me** and **1** complex varied only by the appearance of a broad singlet peak at 9.10 ppm for **1** that is absent in **1Me**, thus confirms the presence of hydroxyl groups and the successful hydrolysis of **1Me** to **1**. The Pc-core aromatic protons of **1Me** were between 7.29 ppm and 8.31 ppm all integrating to 12 protons while the other protons resulted from the aromatic ring of substituents: 7.32 ppm (2 protons) and 7.62 ppm (2 protons), the methoxy group (3.75 ppm, 3 protons) and the *tert*-butyl groups (1.78 ppm, 27 protons), all accounting to 46 protons contained on **1Me** complex. Complex **1** gave a broad singlet peak at 9.10 ppm which confirms the presence of carboxylic acid after hydrolysis of **1Me**.

The aromatic peaks of complex **1** were indicated by the presence of a multiplet peak at 8.29 - 8.16 ppm, a singlet at 7.81 ppm and another singlet at 7.97 ppm which completes all 12 protons of the Pc core aromatic rings. The aromatic ring of substituent groups gave a doublet of doublets (7.53 ppm) which integrated to four protons that completes the aromatic ring of the substituent. The *tert*-butyl groups gave a sharp singlet peak at 1.75 ppm which integrated to 27 protons, thus completing the 44 protons of complex **1**. Mass spectra of complex **1Me** and **1** gave masses of 944 and 930, respectively which is four protons less than the calculated mass $[M - 4H]^-$ for **1Me** and one proton more than the calculated mass $[M+1H]^+$ for **1**. The elemental analysis of MPcs **1Me** and **1** gave percentages that in close relation to the analytically calculated percentages.

3.2.2 Zinc (II) 2-mono-(4-oxy cinnamic acid) phthalocyanine.

Complex **3** was synthesized from a mixed condensation reaction of 4-(3,4-dicyanophenoxy) cinnamic acid (**10**) and dicyanobenzene (**12**) in the presence of pentanol, DBU and zinc chloride, Scheme 3.3. The mole ratios of phthalonitriles were 1.5 moles of **10** to 2.5 moles of **12**. The reaction was carried out under argon atmosphere.

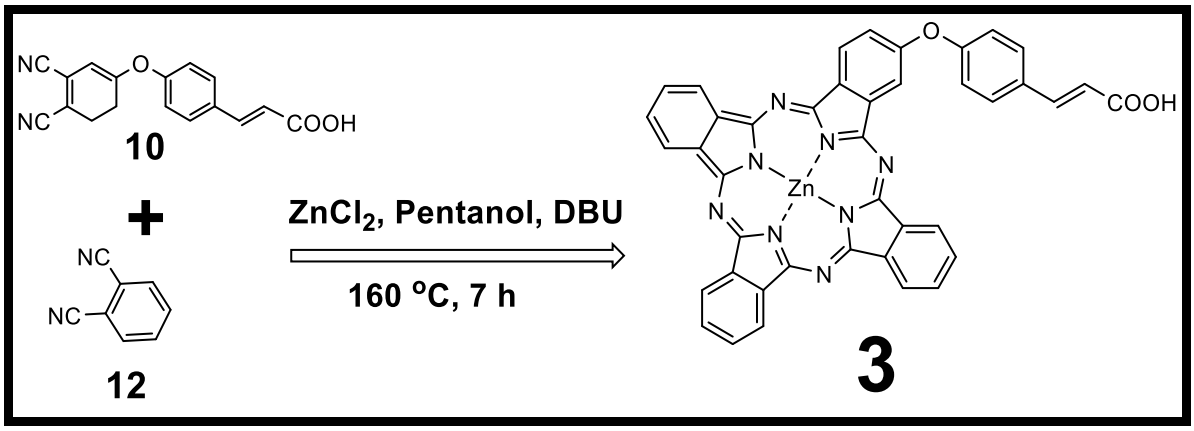

Scheme 3.3. Synthesis of zinc (II) 2-mono-(4-oxy cinnamic acid) phthalocyanine.

FTIR of complex **3** showed stretching peaks at 3090 cm^{-1} and 1712 cm^{-1} corresponding to the hydroxyl group and the carbonyl group of the carboxylic group of **3,** Fig 3.1. The IR peaks of the Pc core were indicated by the aromatic carbon-carbon (Ar-C=C) peaks at 1475 cm^{-1} and the carbon-nitrogen (C-N) peaks at 1233 cm^{-1}. The successful synthesis of complex **3** was also confirmed by an absence of C≡N peaks at 2232 cm^{-1} which represents phthalonitriles (precursors). ^{1}H NMR spectra of complex **3** is illustrated in Fig 3.2. Complex **3** showed a broad singlet peak at 12.45 ppm indicating the carboxylic proton which integrated into a single

proton. The aromatic protons of the Pc-core were between 8.13 -7.43 ppm, with a multiplet at 7.91- 7.77 ppm which integrated to eight protons, a doublet at 8.13 ppm and 7.62 ppm that integrated to four protons together, a multiplet at 7.50 - 7.43 ppm which integrated to three protons together. The substituents had double of a doublet peaks at 7.22 arising from aromatic ring which integrated into four protons. The unsaturated carbons of substituents gave two singlet peaks at 6.57 ppm and 6.51 ppm which both integrated into two protons, completing the total 22 protons of complex **3**. Mass spectra of complex **3** gave mass of 742, which is two protons more than the calculated mass $[M + 2H]^+$. The elemental analysis of **3** gave percentages that is close to the analytically calculated percentages, hence confirming the successful synthesis and characterization of **3**.

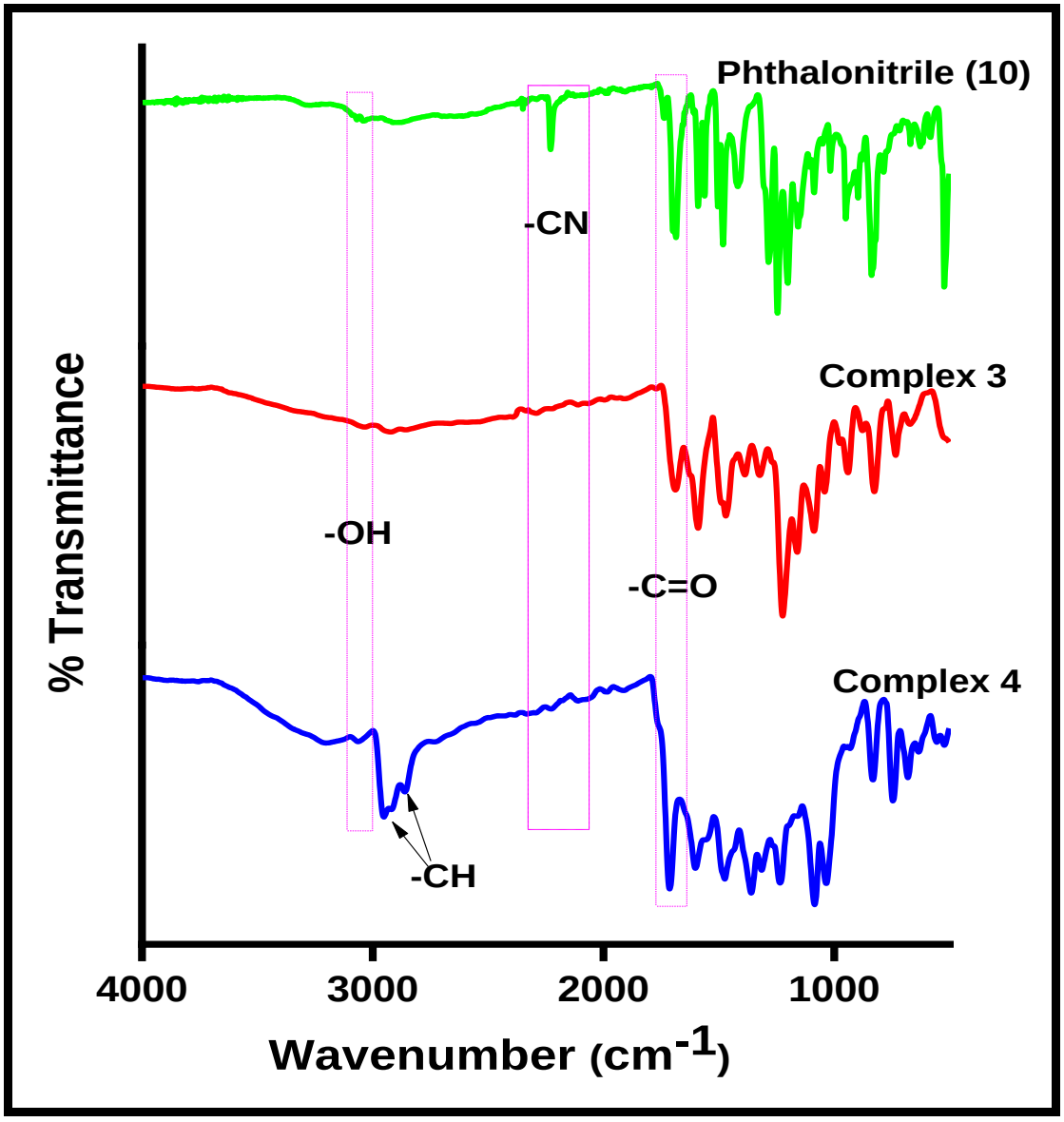

Fig 3.1. FTIR spectra of MPcs **3** and **4** and the phthalonitrile (**10**) precursor.

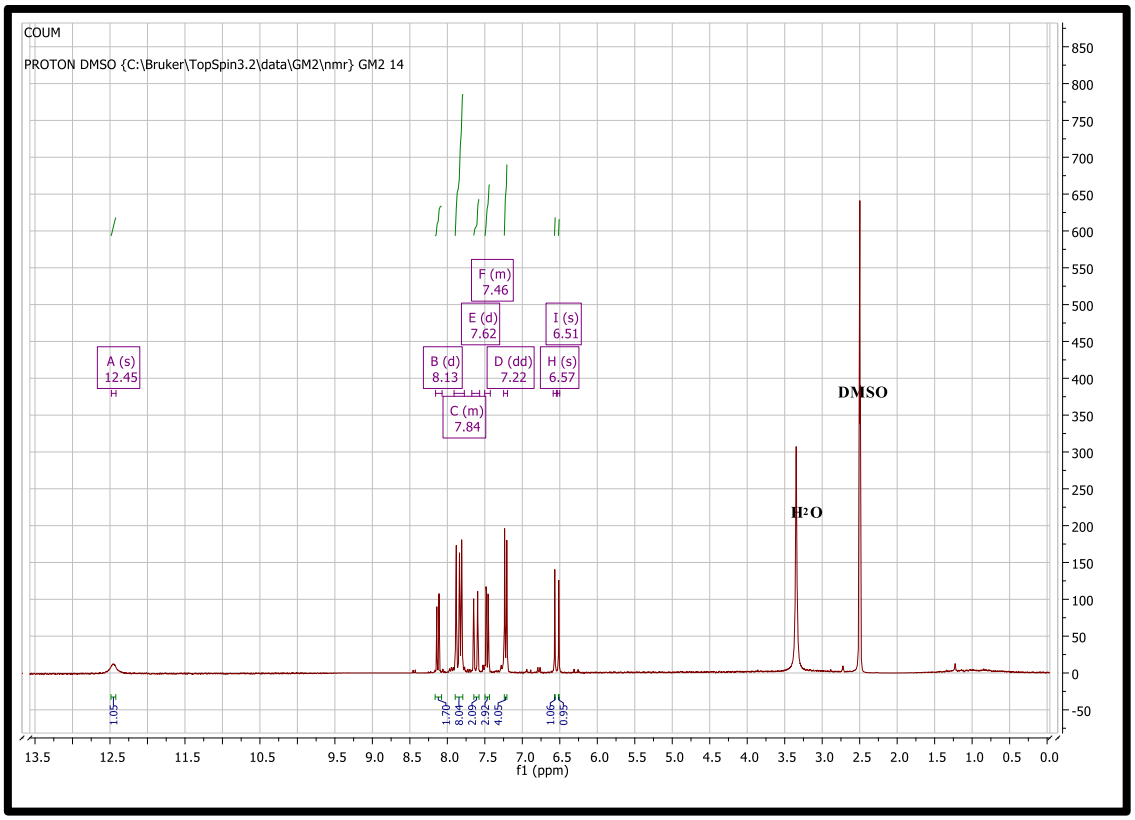

Fig 3.2. ^{1}H NMR spectra of complex **3** in deuterated DMSO.

3.2.3 Zinc (II) tris (*tert*-butyl)-2-(4-oxy cinnamic acid) phthalocyanine.

The synthesis of complex **4** was achieved by a reaction of 4-(3,4-dicyanophenoxy) cinnamic acid (**10**) and 4-(*tert*-butyl) phthalonitrile (**11**) in the presence of pentanol, DBU and zinc chloride under an inert environment, Scheme 3.4. The mole ratios of phthalonitriles were 1 mole of **10** to 4 moles of **11**.

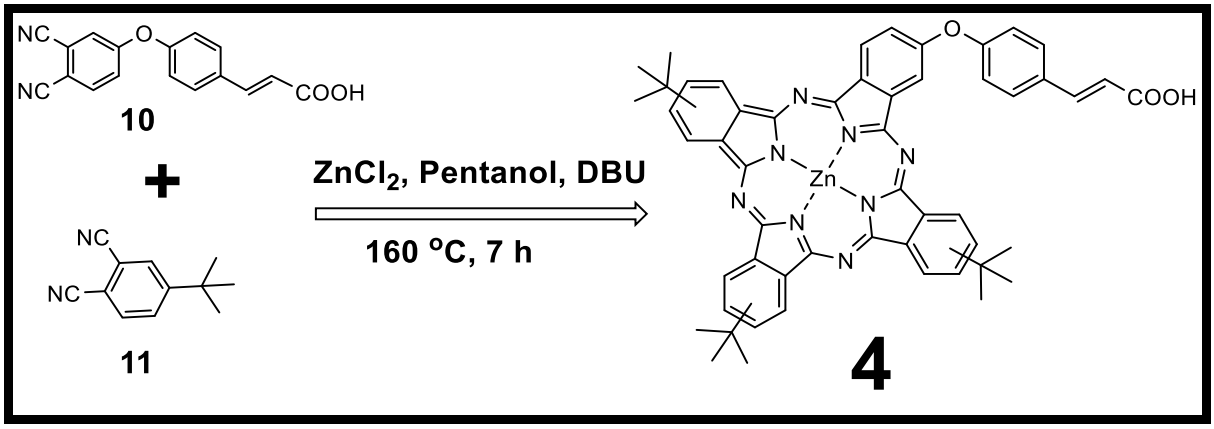

Scheme 3.4. Synthesis of zinc (II) tris-(*tert-butyl*)-2-(4-oxy cinnamic acid) phthalocyanine.

FTIR of complex **4** showed the absence of a nitrile peak (C≡N) at ~2230 cm^{-1} indicating the complete cyclotetramerization of precursors (phthalonitrile), Fig 3.1. The carboxylic functional group of complex **4** was indicated by the broad hydroxyl stretching peaks at 3075 cm^{-1} and the vibrational carbonyl peak at 1710 cm^{-1}, Fig 3.1. The aromatic carbons of the Pc core and the substituent phenyl groups were observed at 1488 cm^{-1}, while the unsaturated carbons of the Pc core and the cinnamic acid substituent were observed at 1604 cm^{-1}. An ether stretching peak was also observed at 1235 cm^{-1} completing the functional groups of chemical structure

of complex **4**. ^{1}H NMR of complex **4** showed a hydroxyl proton peak of the carboxylic acid at 12.95 ppm, *tert*-butyl protons at 1.35 ppm (27 protons) and the Pc aromatic protons resonating as multiplets at 8.42 – 8.10 ppm and 7.87 – 7.51 ppm integrating to 12 protons. The aromatic protons of the cinnamic acid substituent were observed as two doublets at 7.22 ppm and 7.15 ppm while the alkene double bond protons showed two singlet peaks at 7.01 ppm and the other upfield at 7.38 ppm deshielded by the carboxylic acid. The *tert*-butyl substituent signals were observed at 1.35 as a singlet peak that integrated into 27 protons, hence completing the proton signals of complex **4**. MALDI-TOF mass to charge ratio (m/z) was found to be 907.69 for complex **4**, which was close to the calculated mass of 908 amu for complex **4**, Fig 3.3. The elemental analysis of complex **4** gave values close to those of the analytically calculated percentages.

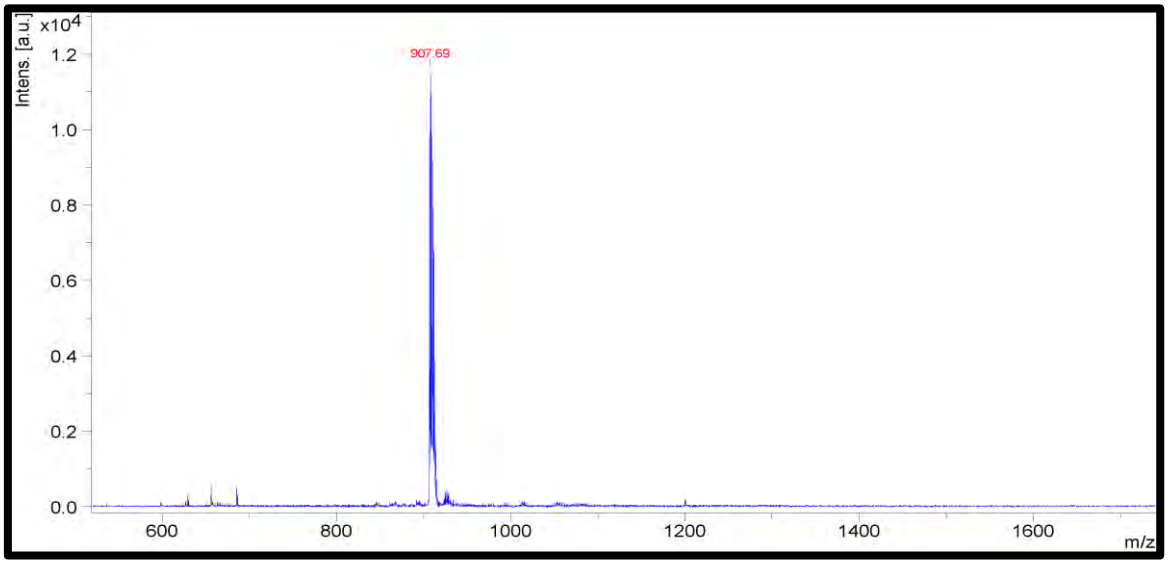

Fig 3.3. MALDI-TOF Mass spectra of complex **4** depicting the mass to charge ratio (m/z) of 907.69.

3.2.4 Zinc (II) tris-(4-*tert*-butyl phenoxy)-2-(4-oxy cinnamic acid) phthalocyanine.

Complex **5** was synthesized from mixed condensation reaction of 1 mole 4-(3,4-dicyanophenoxy) cinnamic acid (**10)** and 4 moles 4-(4-(*tert*-butyl)phenoxy) phthalonitrile (**13)** in the presence of zinc chloride, pentanol and DBU. The reactions were carried out in an inert atmosphere, Scheme 3.5.

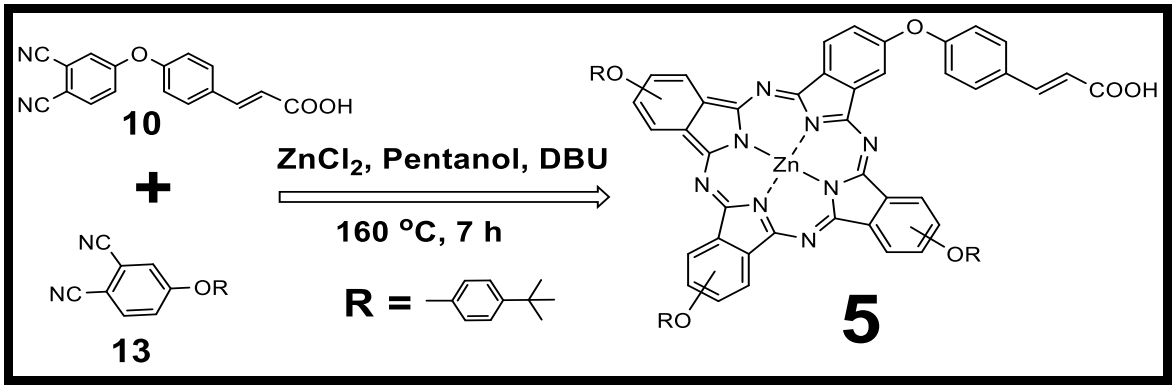

Scheme 3.5. Synthesis of zinc (II) tris-(4-*tert*-butyl phenoxy)-2-(4-oxy cinnamic acid) phthalocyanine.

FTIR showed stretching peaks at 3061 cm^{-1} and 1711 cm^{-1} for the hydroxyl and carbonyl carbon group of the carboxylic acid group, respectively. The aromatic carbons (Ar-C=C) of benzene rings together with the unsaturated carbon (C=C) showed stretching peaks at 1486 cm^{-1} and 1590 cm^{-1}, respectively. The ether bond (Ar-O-Ar) was observed at 1229 cm^{-1} while the CH_3 of *tert*-butyl groups were observed as two sharp stretching peaks at 2949 cm^{-1} and 2859 cm^{-1}.

^{1}H NMR of complex **5** showed the carboxylic acid proton signal as a singlet at 11.29 ppm, *tert*-butyl protons peak were observed at 1.31 ppm which integrated to 27 protons, aromatic protons of the Pc ring were observed as two multiplets at 8.38-8.20 ppm and 7.48-7.33 ppm which integrated to 6 protons each, the phenyl protons of the substituents were observed as a multiplet with 12 protons at 8.02-7.73 ppm and also as a doublet of doublets with 4 protons at 7.52 ppm, the alkene double bond protons of the cinnamic acid completed the protons of complex **5** with a doublet at 7.13 ppm which integrated to 2 protons.

MALDI-TOF mass to charge ratio (m/z) was found to be 1186 which is one proton extra to the calculated atomic mass unit (amu) of 1185 for complex **5.** The elemental analysis of complex **5** gave values close to those of the analytically calculated percentages, confirming the elemental structure of complex **5**. The elemental analysis results of complex **5** are in agreement with observations that MPcs are often isolated as hydrates [115].

3.2.5 Zinc (II) and indium (III) chloride 2(3), 9(10), 16(17), 23(24)-tetrakis-(4-oxy cinnamic acid) phthalocyanine.

Scheme 3.6 illustrates the synthesis of zinc (II) (**6**) and indium (III) chloride (**7**) 2(3), 9(10), 16(17), 23(24)-tetrakis-(4-oxy cinnamic acid) phthalocyanines by the cyclotetramerization of 4-(3,4-dicyanophenoxy) cinnamic acid (**10**) in the presence of pentanol, metal salts (zinc (II) chloride for **6** and indium (III) chloride for **7**) and DBU under an inert environment.

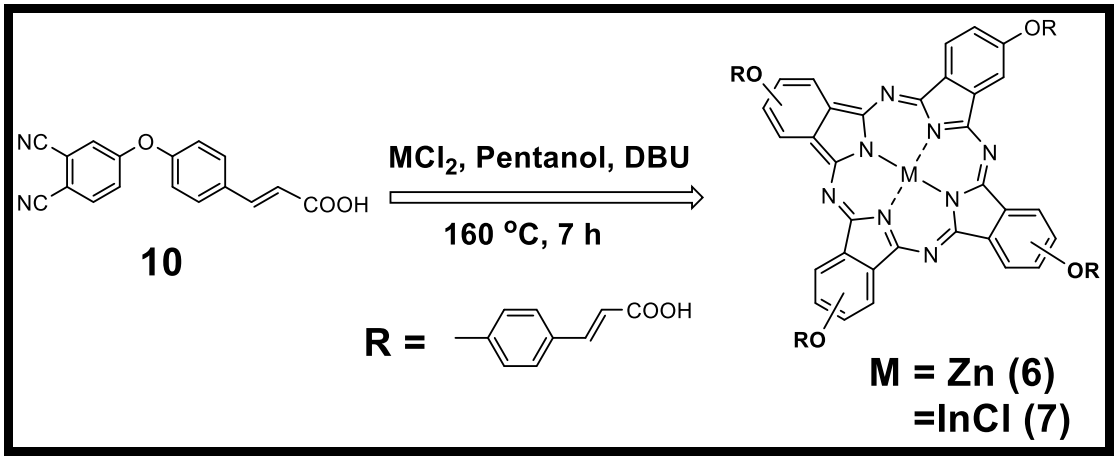

Scheme 3.6. Schematic representation of zinc (II) and indium (III) chloride 2(3), 9(10), 16(17), 23(24)-tetrakis-(4-oxy cinnamic acid) phthalocyanines.

FTIR showed vibrational bands at 1694 cm^{-1} and 1712 cm^{-1} corresponding to –COOH carbonyl peak for **6** or **7,** respectively. The carboxylic group moieties also showed broad hydroxyl stretching bands at 3045 cm^{-1} and 3030 cm^{-1} for **6** and **7**, respectively. Aromatic saturated carbons (C=C) of MPcs were indicated by the stretching bands at 1497 cm^{-1} for **6** and 1489 cm^{-1} for **7**, while the unsaturated carbons (C=C) showed peaks at 1610 cm^{-1} for **6** and 1628 cm^{-1} for **7**. The ether link

(Ar-O-Ar) between the ring substituents and the Pc macrocycle was confirmed by the peak at 1232 cm^{-1} and 1228 cm^{-1} for **6** and **7**, respectively. MALDI TOF mass spectra gave the expected atomic masses of MPcs. ^{1}H NMR showed carboxylic acid proton singlet signals at 12.36 ppm for **6** and 12.31 ppm for **7**, integrating to four protons for both MPcs. The aromatic proton signals for **6** were between 8.73-7.96 ppm for the Pc core and 7.91-7.49 ppm for the phenyl ring substituents. The deshielded unsaturated carbon protons (C=C) showed signals between 6.88 - 6.38 ppm, which completed the chemical protons of **6,** Fig 3.4. Elemental analysis of **7** gave percentages close to the analytically calculated values, while **7** gave percentages that indicated the presence of hydrates [115].

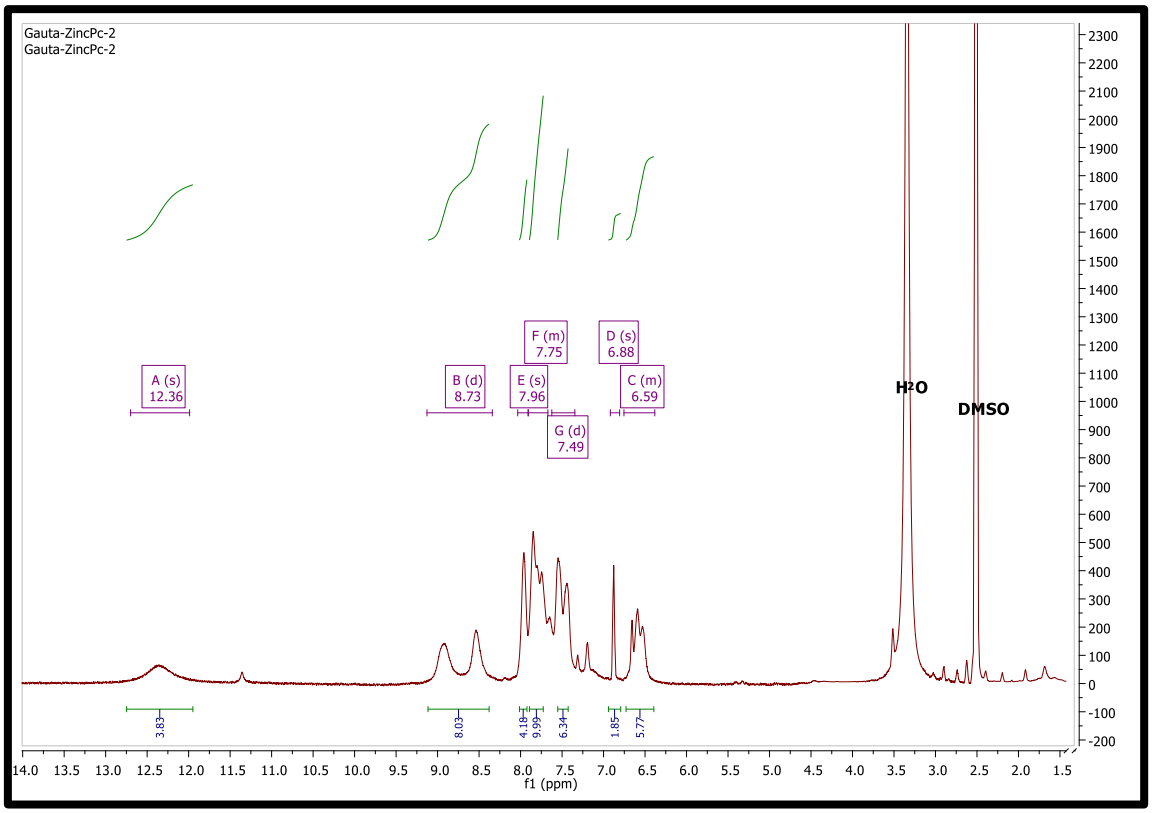

Fig 3.4. ^{1}H NMR spectra of complex **6** in deuterated DMSO.

3.2.6 Electronic absorption spectra of MPcs.

MPcs showed an electronic absorption spectra which are typical of MPcs in DMSO, with single Q-bands with maxima at 677 nm for **1**, 674 nm for **2**, 675 nm for **3**, 679 nm for **4**, 682 nm for **5**, 679 nm for **6** and 689 nm for **7** while the B-band was observed at ca 350 nm for all MPcs, Table 3.1 and Fig 3.5. There was a slight red shifting of the Q-band for **1** compared to **2**, both carboxy phenoxy MPcs (**1** and **2**). The bulky *tert*-butyl groups of MPcs **1**, **4** and **5** form distortions of the Pc ring which results in red shifting of the Q-bands [116,117] when compared to **2** and **3**, Table 3.1.

Complex **7** shows a broadening of the vibrational band area which is typical of H aggregation in phthalocyanines [11]. The axial ligand, chlorine (Cl) of **7** is expected to reduce the π- π interaction of MPc, but this was not the case. The Q-band maxima of InTCAPc (**7**) was more red-shifted as compared to ZnTCAPc (**6**), Table 3.1. The red-shifting of the Q-band for **7** containing In as compared to **6** and other ZnPcs (**1-5**) results from the higher π-electron density and the lower energy gap (ΔE) between the highest occupied molecular orbital (HOMO) and lowest unoccupied molecular orbital (LUMO) that is caused by weakening of the central metal to nitrogen (M-N) bond of MPcs in the presence of a heavier central metal [118–120], Table 3.1.

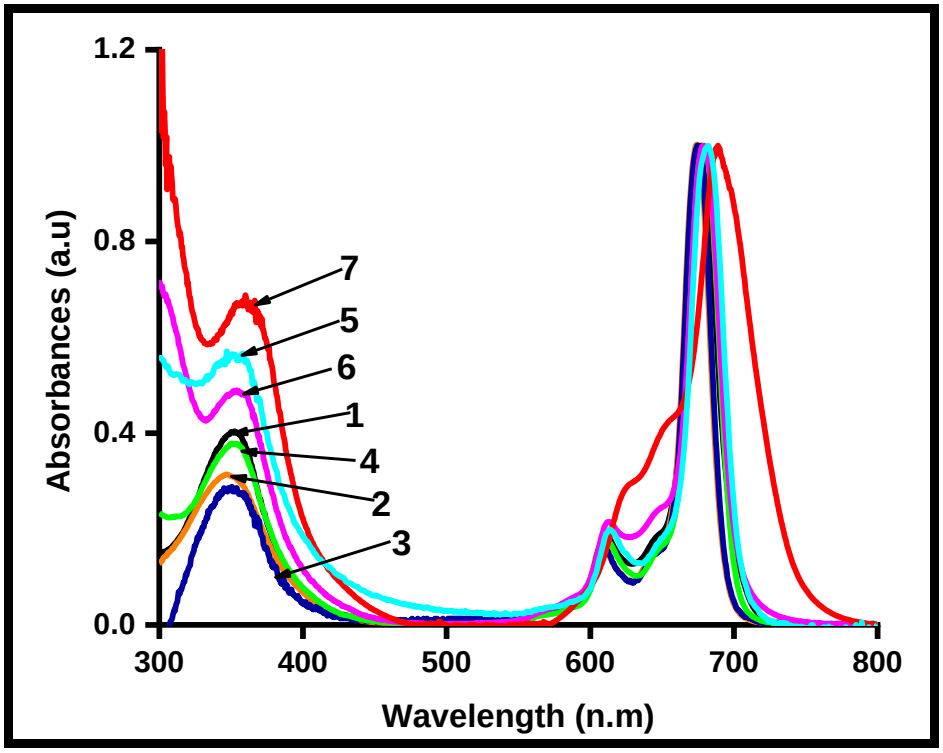

Fig 3.5. Normalized electronic absorption spectra of MPcs (**1-7**) in DMSO.

Table 3.1. Spectral properties of MPcs in DMSO.

Complex	Q-band (λ_{max}/nm)
1	677
2	674
3	675
4	679
5	682
6	679
7	689

3.3 CONJUGATION OF MPCS.

3.3.1 AMNPs conjugates.

The synthesis of AMNPs was achieved by co-precipitation of iron (II) and iron (III) salts in the presence of 25% ammonium solution and water, Scheme 3.7. TEOS was used to coat the MNPs with silica to achieve a hydrophilic surface that will allow for the addition of NH_2 by coating with APTES.

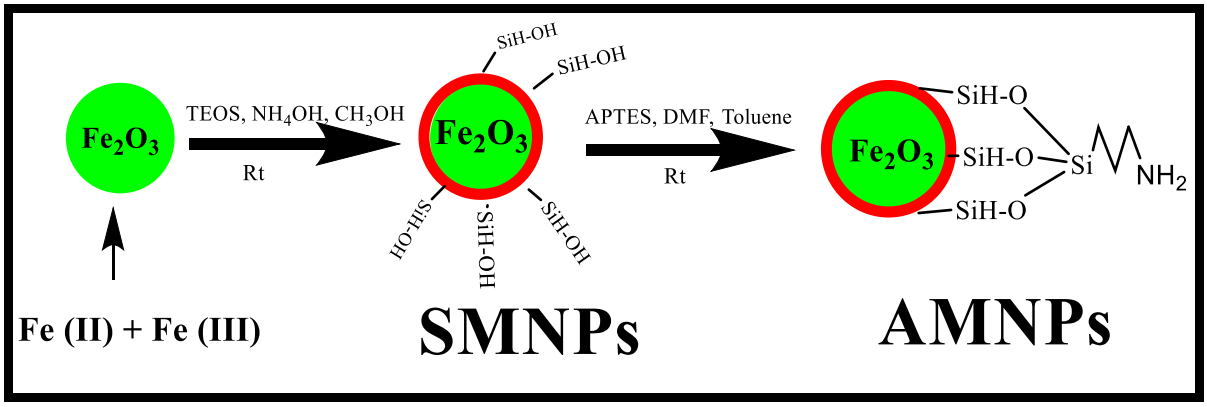

Scheme 3.7. Synthesis of amino functionalized magnetic nanoparticles (AMNPs).

Scheme 3.8 illustrates the covalent linkage of MPcs **1** - **4**, **6** and **7** onto the surface of AMNPs through an amide bond using DCC and NHS as the coupling agents (using **3** for illustrative purposes). Asymmetric MPcs **1** - **4** are only able to link through one attachment side while symmetrical MPcs **6** and **7** have more than one point of attachment. Activation of -COOH groups for **6** and **7** is controlled by number of moles of DCC and NHS to activate only one group in order to avoid chain reactions with AMNPs. The number of Pc molecules bonded to the AMNPs was determined following literature methods, but using absorption instead of

fluorescence [121]. This involves using the Q-band absorbance intensity of a known mass of the conjugate (MPc-AMNP) dissolved in a known volume to determine the mass ratio of the MPcs in the conjugate. Table 3.2 shows a loading of 4.16 μg/mg of **1** in **1**-AMNPs, 3.19 μg/mg of **2** in **2**-AMNPs, 3.42 μg/mg of **3** in **3**-AMNPs, 6.56 μg/mg of **4** in **4**-AMNPs, 4.81 μg/mg of **6** in **6**-AMNPs and 6.43 μg/mg of **7** in **7**-AMNPs. The difference in the amount of MPcs per milligram of MPc-AMNPs conjugate could be as a result of the differences in the dispersion of nanoparticles in MPcs solution [122].

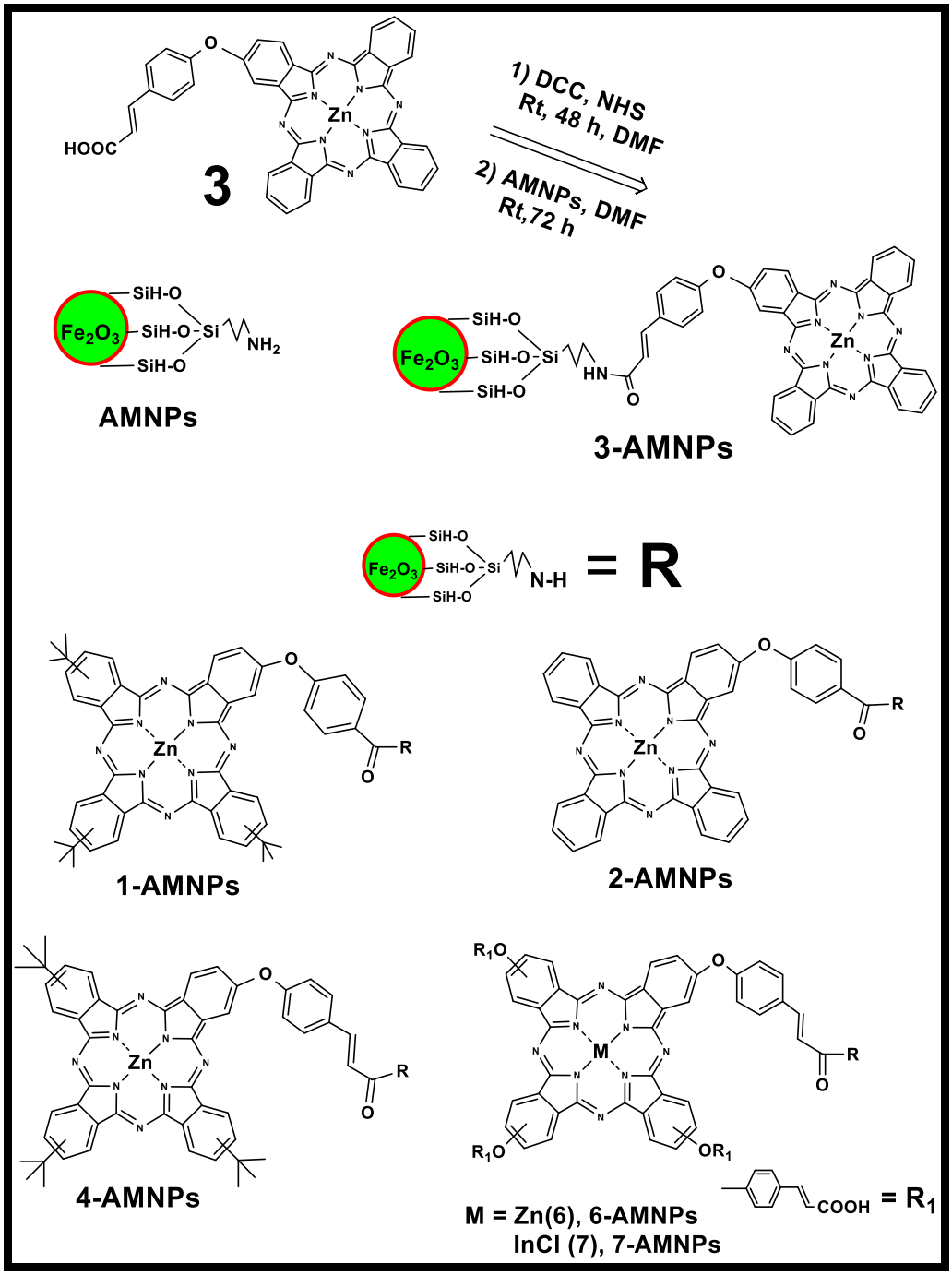

Scheme 3.8. Schematic illustration of the amide bond linkage of complex **3** to AMNPs. **1**-AMNPS, **2**-AMNPs, **4**-AMNAPs, **6**-AMNPs and **7**-AMNPs were also prepared under the same reaction conditions.

3.3.1.1 FTIR analysis.

The covalent linkage between MPcs and AMNPs was achieved through an amide bond between the COOH groups of MPcs and the NH_2 of AMNPs. FTIR spectra depicting the peaks of interest for amide linked MPc-AMNPs conjugates are illustrated on Fig 3.6. The amide bond between the MPcs and the AMNPs was confirmed by the appearance of an amide bend (N-H) and the amide carbonyl stretching bend on FTIR spectra of MPc-AMNPs.

The amide bend (NH) for the conjugates was observed at 1594 cm^{-1} for **7**-AMNPs, 1591 cm^{-1} for **6**-AMNPs, 1569 cm^{-1} for **4**-AMNPs, 1540 cm^{-1} for **3**-AMNPs, **2**-AMNPs and **1**-AMNPs while the amide carbonyl stretching bends were observed at 1654 cm^{-1} for **7**-AMNPs, 1655 cm^{-1} for **6**-AMNPs, 1648 cm^{-1} for **4**-AMNPs, 1640 cm^{-1} for **3**-AMNPs, **2**-AMNPs and **1**-AMNPs, Fig 3.6. MPc-AMNPs also had a very sharp and strong peak at 1034 cm^{-1} indicative of the siloxane band resulting from the tetraethyl othorsilicate and amino functionality coating on MNPs. The appearance of an amide bond peaks on the infrared spectra provided evidence for the successful linkage of MPcs to AMNPs.

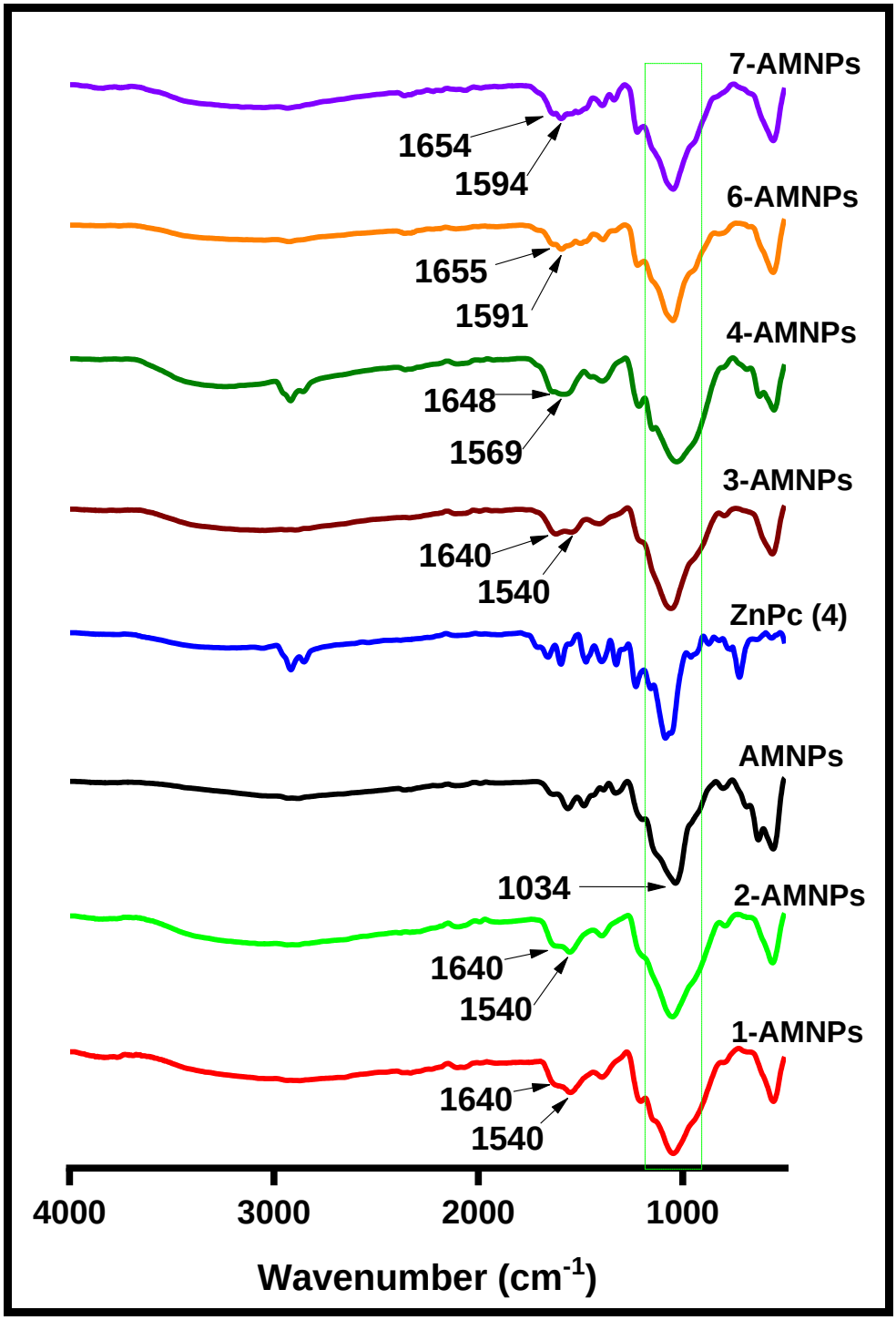

Fig 3.6. FTIR spectra of chemically linked MPc-AMNPs conjugates. Complex **4** was used as a representative of MPcs.

3.3.1.2 TEM micrographs.

TEM images of AMNPs reflected spherically shaped nanoparticles with size range of ≈ 15 nm as shown on Fig 3.7A and its corresponding histogram. The magnetic nature of the particles makes them to be attracted to each other forming clusters, Fig 3.7A. Linking MPcs to AMNPs resulted in an increase in size together with the presence of sheet like structures which can be attributed to the MPcs linked on the surface of the nanoparticles, Fig 3.7B with **4**-AMNPs as an example. The same size increase and sheet like structure were also observed on TEM images of MPc-AMNPs (**1**-AMNPs, **2**-AMNPs, **3**-AMNPs, **4**-AMNPs, **6**-AMNPs and **7**-AMNPs) conjugates compared to AMNPs alone, Table 3.2. The increase in size is due to the interactions between the Pcs on adjacent NPs via π-π stacking since Pcs may occur leading to aggregation. Pcs are known for their π-π stacking to form H aggregates [11].

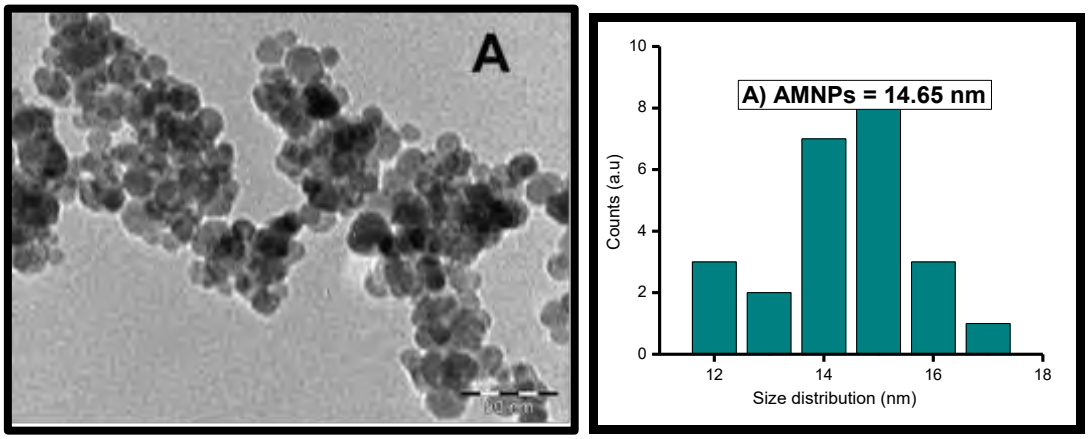

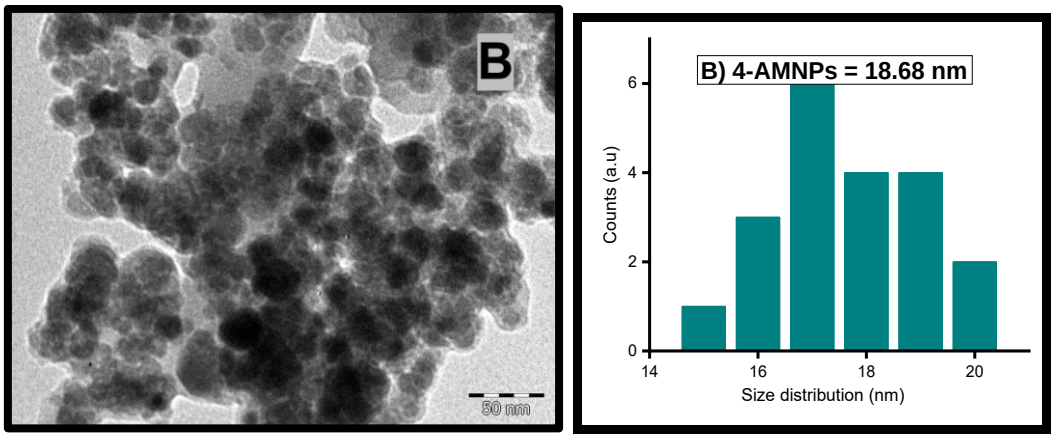

Fig 3.7. TEM micrographs and histograms of A) AMNPs and B) **4**-AMNPs (used for illustration).

3.3.1.3 Energy dispersive x-ray spectroscopy (EDX).

EDX spectra of AMNPs depicted an intense peak of Fe, Si, C and N corresponding to the iron rich nanoparticles and the APTES coating that contains silicon, carbon and nitrogen from the amino groups, Fig 3.8A. The presence of these elements confirms the elemental composition of the as synthesized AMNPs. Incorporation of MPcs on the surface of AMNPs were confirmed by the appearance of Zn as the central metal for MPcs **1** - **4** and **6** while **7** showed In, Fig 3.8B using **3**-AMNPs for illustrative purpose. The EDX spectra of MPc-AMNPs were almost identical. The other elements (C, N and O) were common between the NPs and the MPcs.

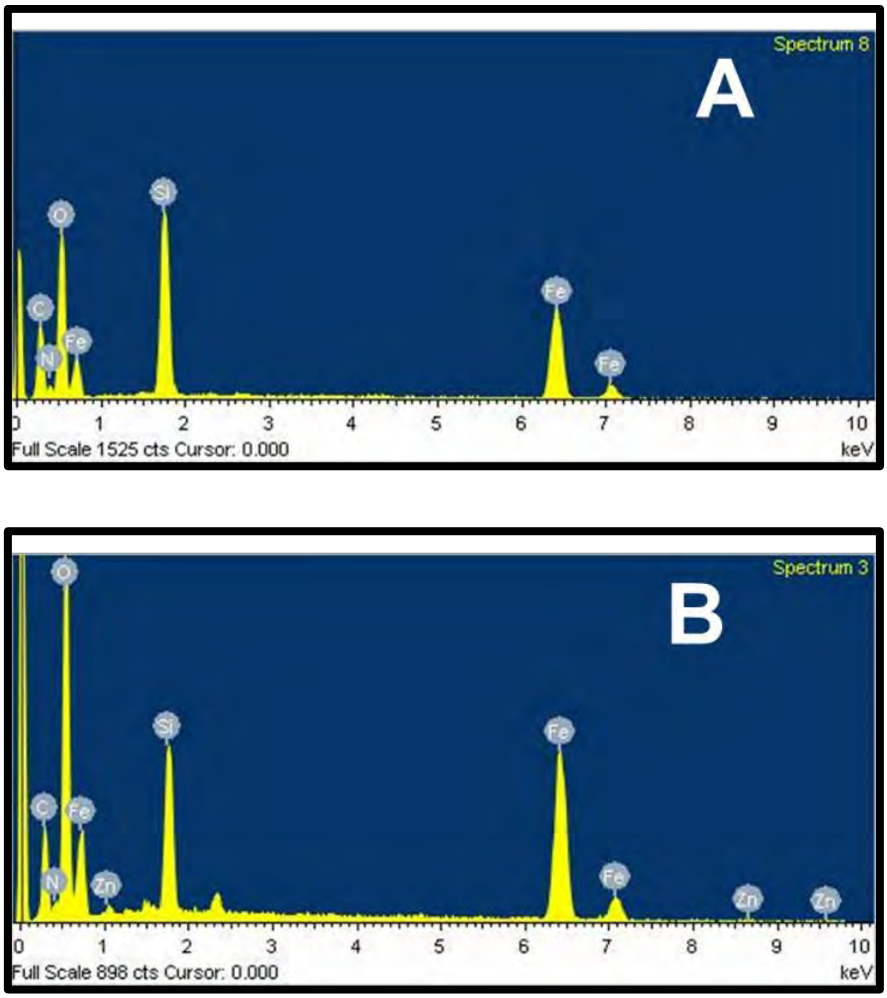

Fig 3.8. EDX micrographs depicting the elemental compositions of A) AMNPs and B) **3**-AMNPs (used for illustration).

3.3.1.4 X-ray diffraction (XRD) spectroscopy.

XRD spectroscopy was used to show the changes in the crystal structure of the AMNPs upon linkage of MPcs. The XRD patterns of MPcs (complex **1** used as an example of MPcs) and the conjugates (**1**-AMNPs, **2**-AMNPs, **3**-AMNPS, **4**-AMNPs, **6**-AMNPs and **7**-AMNPs) are illustrated in Fig 3.9.

The crystal structure of AMNPs have a face centered cubic structure at diffraction peaks at 2θ = 30°, 36°,43°, 54°,57° and 63°, corresponding to hkl Milner indices of 220, 311, 400, 422, 511 and 440, respectively, Fig 3.9. These indices indicates the formation of fully crystalline iron oxide with a cubic structure, consistent with the standard data of magnetite (JCPDS Card no. 00-019-0629) [123]. After conjugation, the AMNPs diffraction peaks were clearly observable on the pattern of **1-**AMNPs, **2-**AMNPs, **3**-AMNPs, **4**-AMNPs, **6**-AMNPs and **7**-AMNPs.

The XRD patterns of MPc-AMNPs conjugates also showed the MPcs diffraction peak at 2θ = 15°, Fig 3.9 using complex **1** as an example. The broad peak near 2θ = 15° [124] is typical of the amorphous nature of phthalocyanine, showing the incorporation of MPcs on the nanoparticles surface. The Debye-Scherrer equation (3.1) was used to determine the sizes of AMNPs and their conjugates [125].

$$d = \frac{k\lambda}{\beta Cos\theta} \quad \text{.....3.1}$$

where d is the crystal size, λ is the wavelength of the X-ray source (0.1541 nm), k is an empirical constant equal to 0.9, β is the full width at half maximum of the diffraction peak and θ is the diffraction angle of the crystal orientation peak.

Table 3.2 lists the sizes of conjugates (**1**-AMNPs, **2**-AMNPs, **3**-AMNPs, **4**-AMNPs, **6**-AMNPs and **7**-AMNPs) and the AMNPs. The size of AMNPs increased following conjugation of MPcs due to aggregation as discussed above, Table 3.2.

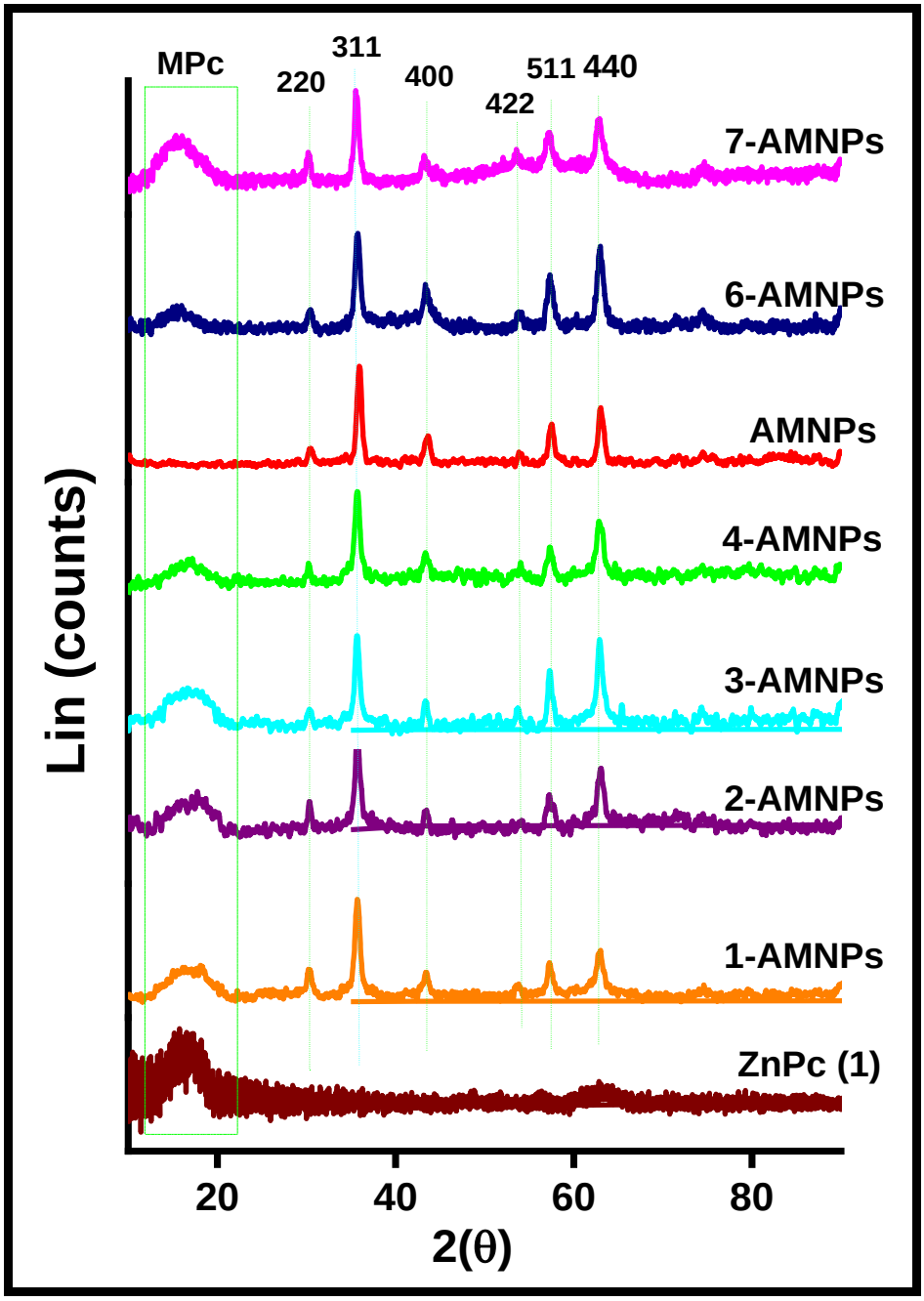

Fig 3.9. XRD spectra of AMNPs and MPc-AMNPs conjugates. Complex **1** was used as a representative of MPcs.

3.3.1.5 Dynamic light scattering (DLS).

DLS results of AMNPs and MPc-AMNPs are illustrated on Fig 3.10A and B (using **6**-AMNPs for illustration). There was an increase in size of AMNPs following incorporation of MPcs (**1**- **4**, **6** and **7**) on the surface of nanoparticles, as also observed for the XRD and TEM, Table 3.2. The polydispersity index (PDI) values of AMNPs and MPc-AMNPs conjugates were below 0.3 indicating a good dispersion and low particle size distribution, Table 3.2. PDI values below 0.7 indicate a lower particle size distribution [126]. The sizes determined by DLS have been reported to be larger than those determined by other methods since DLS sizes tend to be skewed toward larger particles [127], hence DLS values are in most cases larger than those found from XRD and TEM, Table 3.2.

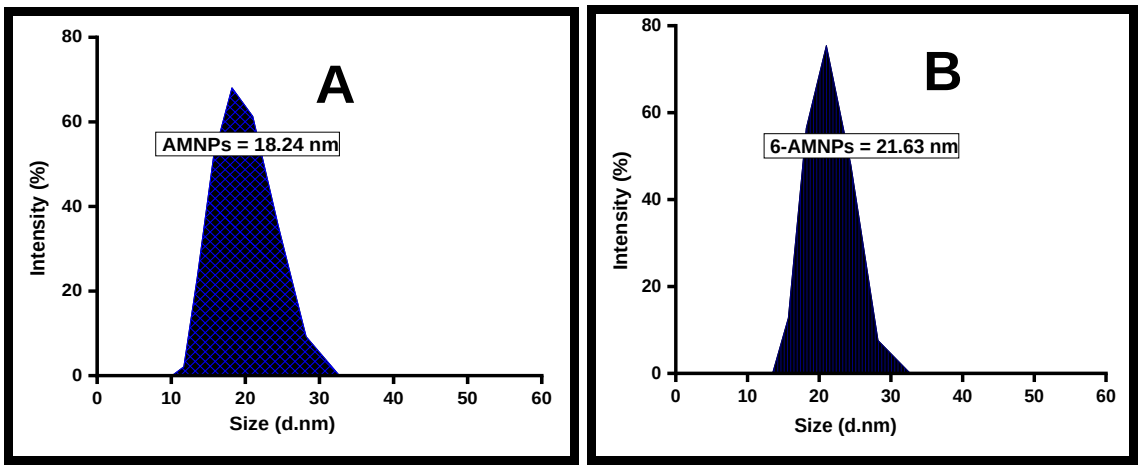

Fig 3.10. DLS spectra depicting the hydrodynamic sizes of A) AMNPs and B) **6**-AMNPs in DMSO.

Table 3.2. Summary of average sizes of nanoparticles and their conjugates as studied using DLS, XRD and TEM.

NPs/ Conjugates	Loading ($\mu g/mg$ (Pc/NPs))	DLS (nm) (PDI)	XRD (nm)	TEM (nm)
AMNPs	-	15.15 (0.145) 16.45[a] (0.186) 18.24[b] (0.154)	15.35 14.93[a] 16.45[b]	13.89 14.65[a] 15.23[b]
1-AMNPs	4.16	17.45 (0.274)	19.31	16.20
2-AMNPs	3.19	18.15 (0.241)	17.56	15.85
3-AMNPs	3.42	17.46 (0.217)	18.15	16.28
4-AMNPs	6.56	21.20[a] (0.292)	18.52[a]	18.68[a]
6-AMNPs	4.81	21.63[b] (0.289)	18.78[b]	17.56[b]
7-AMNPs	6.43	24.76 [b] (0.278)	20.23 [b]	18.02 [b]
Cys-AgNPs	-	13.98 (0.126)	11.88	11.68
3-cys-AgNPs	5.76	17.64 (0.188)	15.73	16.23
4-cys-AgNPs	5.34	17.92 (0.184)	14.02	13.93
5-cys-AgNPs	6.56	18.24 (0.219)	16.87	17.55
6-cys-AgNPs	6.12	18.65 (0.247)	17.08	17.15

Three batches of AMNPs were synthesized. [a] and [b] denote the second and third batch, respectively with their MPc-AMNPs conjugates.

3.3.1.6 Electronic absorption spectra of MPc-AMNPs.

Fig 3.11 shows the electronic absorption of MPc-AMNPs, AMNPs and complex **3** (used as an example for MPcs) in DMSO.The AMNPs alone depicted an absorption spectrum that have a slight peak at 385 nm, Fig 3.11. There was broadening of the B-band below 550 nm for the conjugates due to the presence of AMNPs. There were no significant changes in Q-band maxima for **4**-AMNPs compared to **4**, **3**-AMNPs compared to **3** and **2**-AMNPs compared to **2**, Table 3.3. The slight blue shift of **1**-AMNPs = 673 nm compared to **1** = 677 nm can be attributed to the electron deficiency induced on the Pcs upon coordination with NPs as reported before [128]. The observed red shift in the Q–band wavelength of the conjugates (**6**–AMNPs and **7**–AMNPs) compared to the MPcs alone (**6** and **7**) could be attributed to the AMNPs causing perturbation on the electronic structure of the Pc molecule [129].

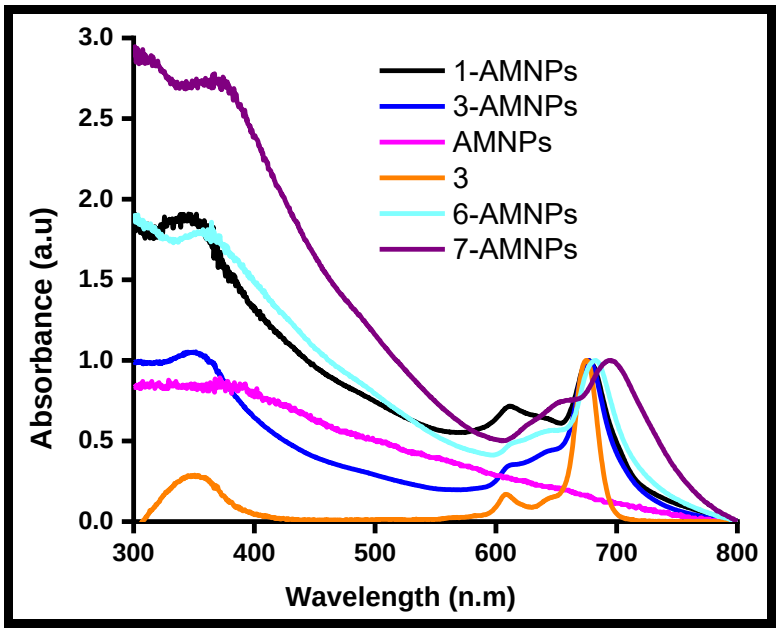

Fig 3.11. Normalized electronic absorption spectra of MPc-AMNPs conjugates in DMSO. **2**-AMNPs and **4**-AMNPs were omitted for clarity.

Table 3.3. Spectral properties of MPcs and their conjugates in DMSO.

Complex	Q-band (λ_{max}/nm)
1	677
1-FA	679 (685)
1/FA mixed	677
1-AMNPs	673
2	674
2-FA	675 (690)
2/FA mixed	675
2-AMNPs	676
3	675
3-FA	675 (690)
3-AMNPs	676
3-cys-AgNPs	676
4	679
4-AMNPs	680
4-cys-AgNPs	680
5	682
5-cys-AgNPs	682
6	679
6-AMNPs	682

6-cys-AgNPs	682
7	689
7-AMNPs	695

Values in brackets indicates the Q-band of linked MPc-FA in water

3.3.2 AgNPs conjugates.

The synthesis of L-cysteine capped silver nanoparticles (cys-AgNPs) was achieved by reacting silver acetate ($AgC_2H_3O_2$) with diphenyl ether in the presence of oleylamine (OLM) and oleic acid (OA). L-cysteine was then added to the reaction mixture to result in the cysteine functionalized AgNPs (cys-AgNPs), Scheme 3.9. The as synthesized cys-AgNPs were characterized with FTIR, DLS, TEM and XRD to confirm the functional groups, size, shape, and the crystal structure of the nanoparticles.

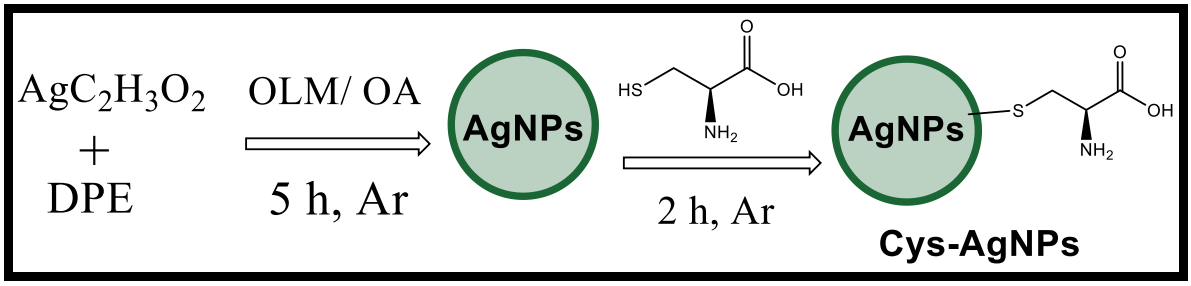

Scheme 3.9. Synthesis of L-cysteine capped silver nanoparticles (cys-AgNPs).

Cinnamic acid ZnPcs **3**-**6** were linked to cys-AgNPs through an amide bond for comparison with AMNPs. Scheme 3.10 illustrates the schematic representation of the amide bond reaction between complex **5** and cys-AgNPs to form **5**-cys-AgNPs (as an example). The same procedure was used to link **3**, **4** and **6** to cys- AgNPs to obtain **3**-cys-AgNPs, **4**-cys-AgNPs and **6**-cys-AgNPs. Activation of the carboxyl group of asymmetric (**3 - 5**) and symmetrical (**6**) MPcs was achieved by controlling the moles of DCC and NHS, as previously described for AMNPs. Loading of MPcs on the nanoparticle surface was determined by using the Q-band intensity of the conjugate as described in literature [121]. Table 3.2 shows a loading of 5.76 µg/mg, 5.34 µg/mg, 6.56 µg/mg, and 6.12 µg/mg corresponding to the amount of MPcs **3**, **4**, **5** and **6** in **3**-cys-AgNPs, **4**-cys-AgNPs, **5**-cys-AgNPs and **6**-cys-AgNPs, respectively. The slight difference in the loading amounts of MPcs on the surface of nanoparticles could be due to the differences in the dispersions of the cys-AgNPs in solutions as stated above [122].

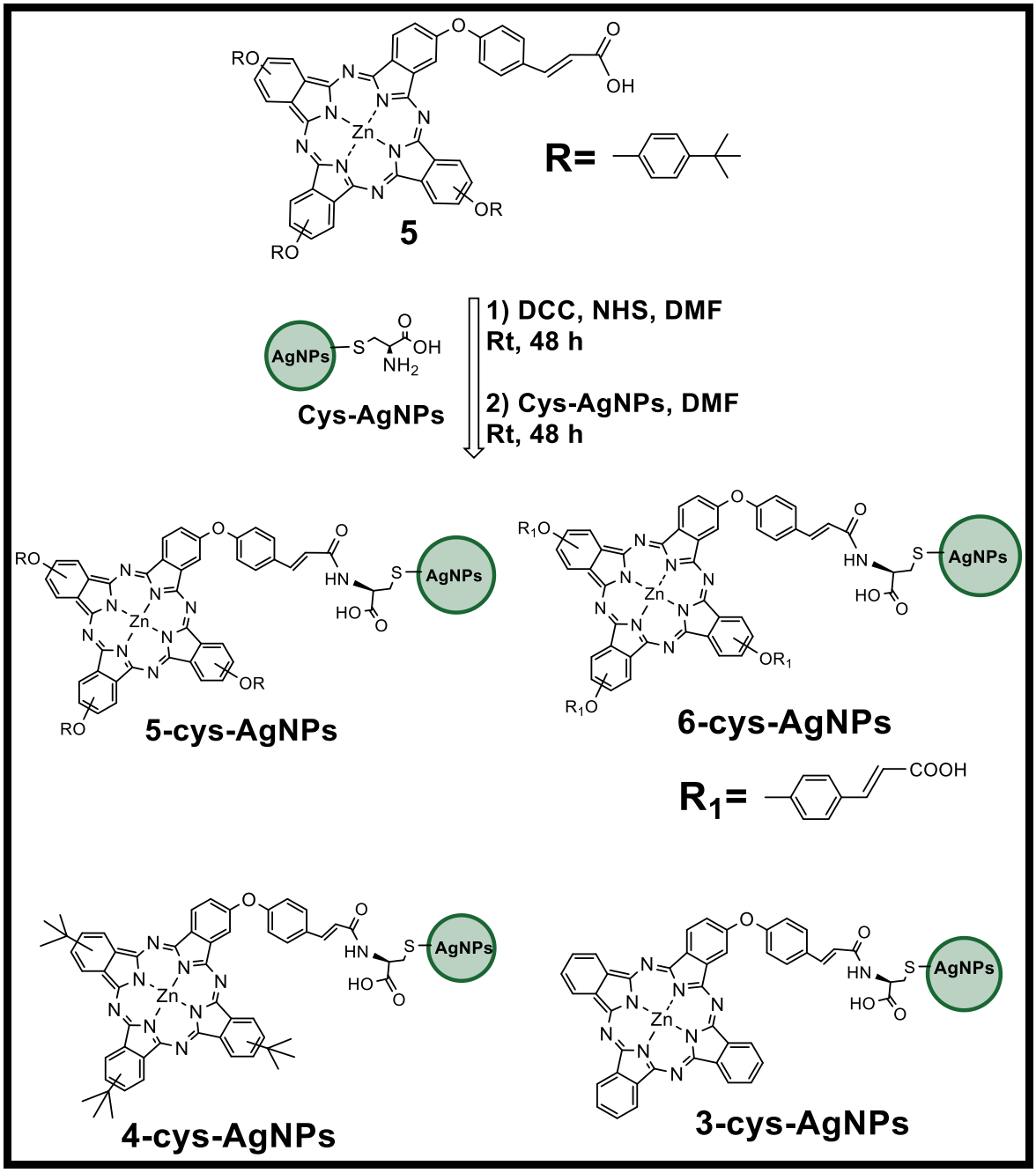

Scheme 3.10. Covalent bond linkage of complex **5** to cys-AgNPs to yield **5**-cys-AgNPs (as an example). The same reaction conditions were used to prepare **3**-cys-AgNPs, **4**-cys-AgNPs and **6**-cys-AgNPs from their respective MPcs.

3.3.2.1 FTIR spectra.

Fig 3.12 Illustrates the FTIR spectra of MPc-AgNPs in comparison to cys-AgNPs and complex **5** (as an example). The covalent linkage between the -COOH groups of MPcs (**3** - **6**) and the NH_2 of cysteine capped AgNPs was confirmed by the appearance of amide peaks on the IR of MPc-AgNPs conjugates. The N-H bending and carbonyl carbon stretching peaks of an amide bond were observed at 1585 cm^{-1} and 1685 cm^{-1} for **3**-cys-AgNPs, 1587 cm^{-1} and 1646 cm^{-1} for **4**-cys-AgNPs, 1536 cm^{-1} and 1642 cm^{-1} for **5**-cys-AgNPs, 1585 cm^{-1} and 1674 cm^{-1} for **6**-cys-AgNPs, respectively, Fig 3.12. Conjugates also showed amide stretching peaks at 3319 cm^{-1} for **3**-cys-AgNPs, 3285 cm^{-1} for **4**-cys-AgNPs, 3286 cm^{-1} for **5**-cys-AgNPs and 3312 cm^{-1} for **6**-cys-AgNPs.

Secondary amino groups show one stretching peak in the NH region (3300 -3500 cm^{-1}) for the conjugates while primary amino shows two stretching peaks as observed for cys-AgNPs alone in the NH region. The presence of NH bends and the amide stretching peaks confirms the amide bond linkage between the NH_2 group of cys-AgNPs and the COOH groups of MPcs **3** - **6** to form the new conjugates **3**-cys-AgNPs, **4**-cys-AgNPs, **5**-cys-AgNPs and **6**-cys-AgNPs.

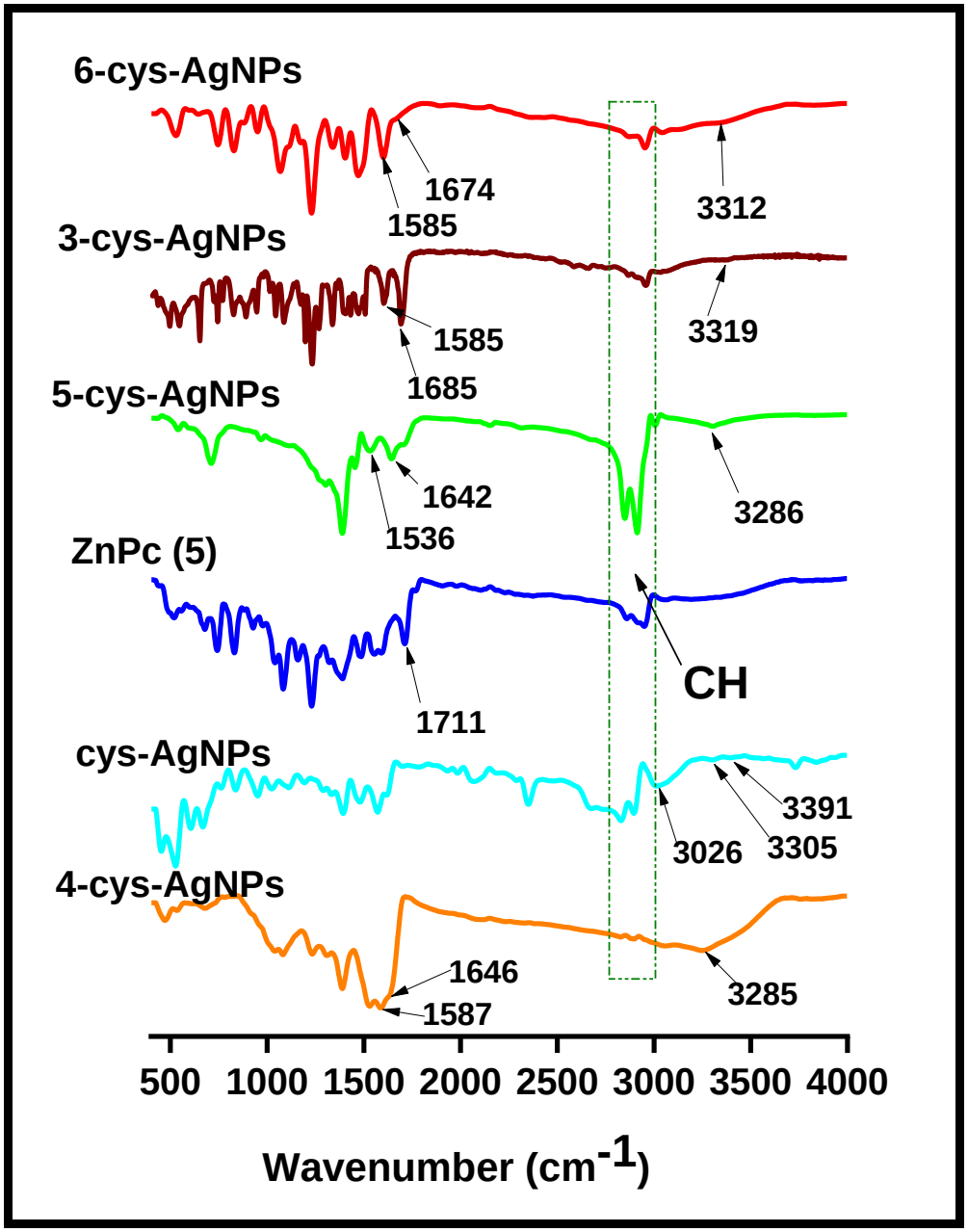

Fig 3.12. FTIR spectra of MPc-AgNPs with cys-AgNPs and complex **5** (as an example).

3.3.2.2 Transmission electron microscope (TEM) analysis.

TEM micrographs and histograms depicting the shape and average size distribution of cys-AgNPs and MPc-AgNPs conjugates are illustrated on Fig 3.13A and B using **5**-cys-AgNPs as an example. Cys-AgNPs alone had a spherical shape with an average size distribution of 11.68 nm, Fig 3.13A and Table 3.2. Fig 3.13B (**5**-cys-AgNPs for representation of MPc-AgNPs) showed sheet like structures on the TEM micrographs due to the conjugation of MPcs. The same sheet-like structures were also observed for **3**-cys-AgNPs, **4**-cys-AgNPs, **6**-cys-AgNPs and with MPc-AMNPs conjugates. A size increase was also observed on the conjugates as compared to the nanoparticles alone, Table 3.2. The increase in size could be attributed to MPcs forming aggregates [11] on the nanoparticle surface, as already explained for AMNPs.

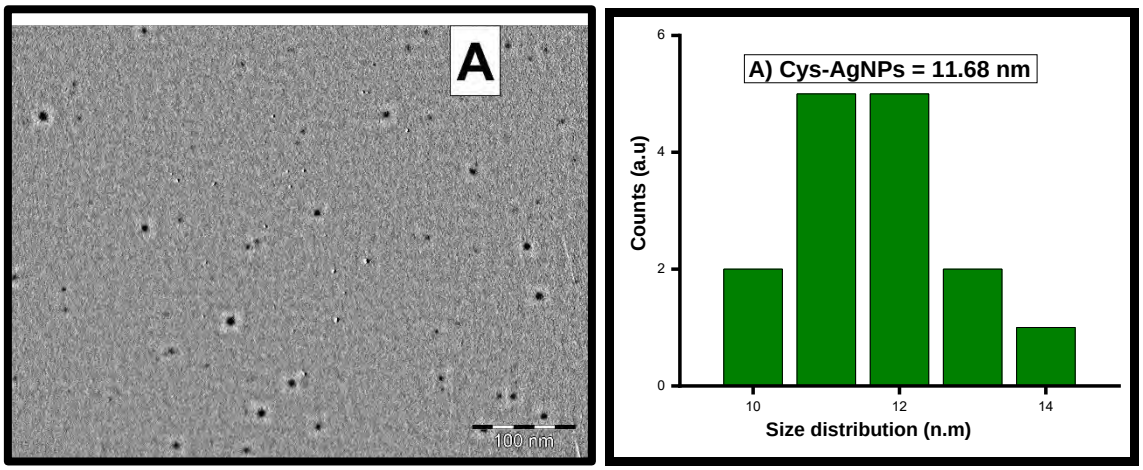

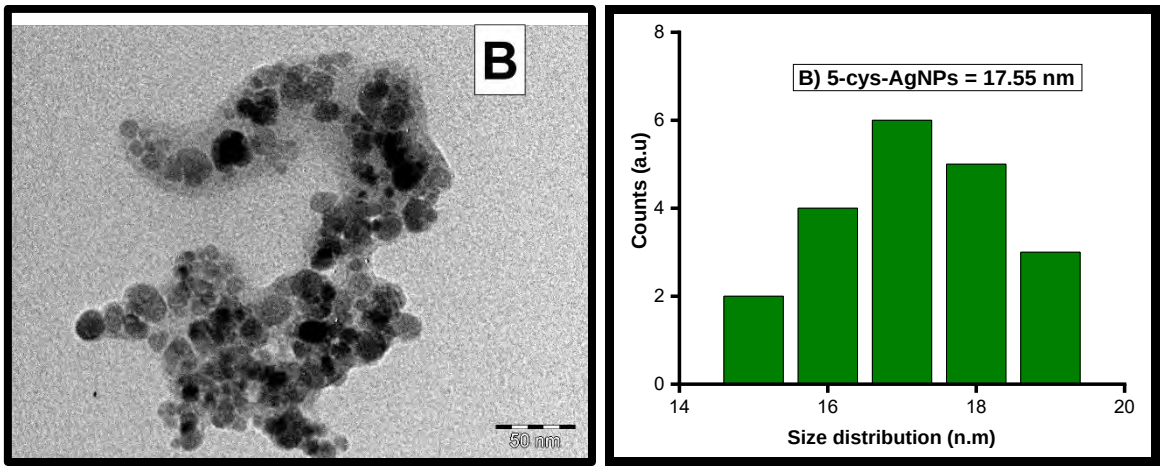

Fig 3.13. TEM images and histograms depicting the shape and average sizes of A) cys-AgNPs and B) **5**-cys-AgNPs (for representative purpose).

3.3.2.3 Energy dispersive X-ray (EDX) Spectroscopy.

EDX micrographs of nanoparticles (cys-AgNPs) and the MPc-AgNPs are illustrated on Fig 3.14 using A) cys-AgNPs and B) **4**-cys-AgNPs for illustrative purposes. **5**-cys-AgNPs **3**-cys-AgNPs and **6**-cys-AgNPs also showed a similar trend with elemental composition. Cys-AgNPs showed an intense peak of Ag, S, C and N corresponding to the silver of AgNPs and sulfur, carbon, and nitrogen of L-cysteine capped ligand, respectively. ZnPc conjugates: **5**-cys-AgNPs, **4**-cys-AgNPs, **3**-cys-AgNPs and **6**-cys-AgNPs showed an additional Zn corresponding to the central metal of MPcs, Fig 3.14B using **4**-cys-AgNPs for illustration. Carbon peak was more intense for conjugates due to the carbon structure of MPcs, Fig 3.14B. The peaks of Zn, in addition to Ag, S, C and N on the conjugates, confirms the elemental composition and incorporation of ZnPcs on the surface of cys-AgNPs.

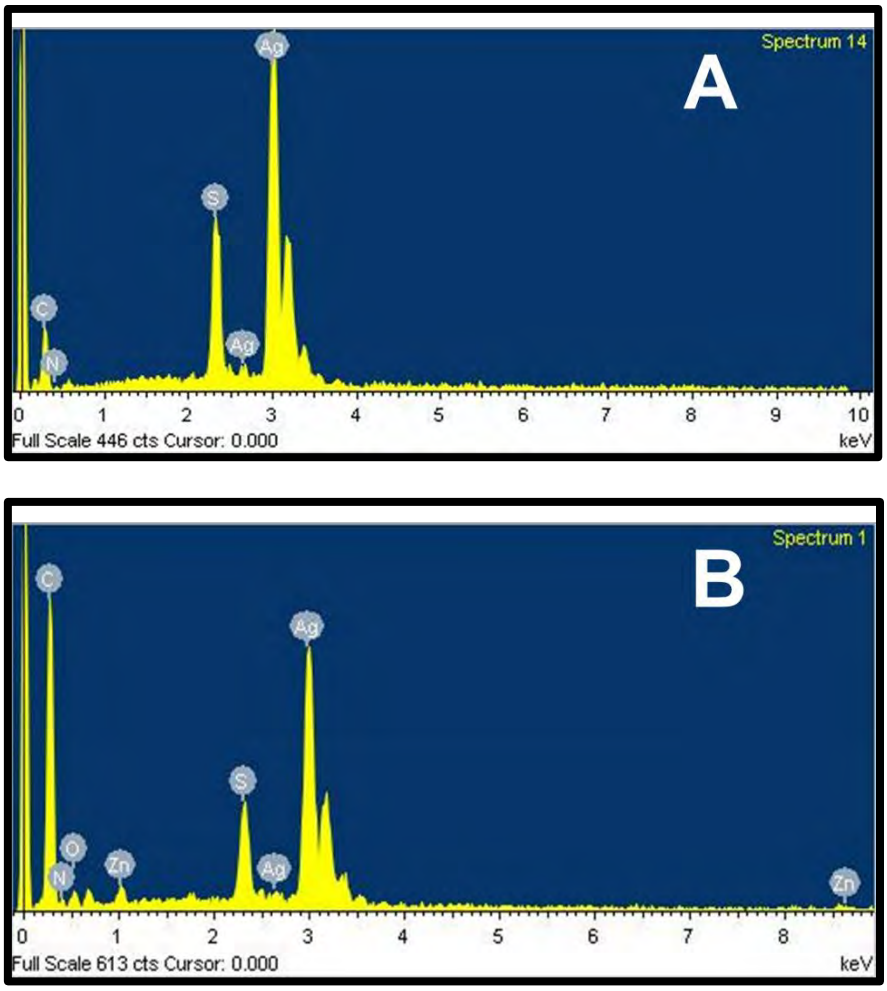

Fig 3.14. EDX micrographs illustrating the atomic composition of A) cys-AgNPs and B) **4**-cys-AgNPs (for illustrative purposes).

3.3.2.4 X-ray diffraction (XRD) spectroscopy.

Fig 3.15 shows the crystal peaks of cys-AgNPs in comparison with MPc-AgNPs conjugates. Cys-AgNPs showed face centered cubic (FCC) crystal peaks at 2θ = 38.4°, 44.7°, 64.9°, 77.6° and 81.0° corresponding to 111, 200, 220, 311 and 222 crystal planes of metallic silver. The lattice planes matches the known face centered cubic crystal peaks of metallic silver (JCPDS Card No. 04-0783) [130]. The ZnPc

alone (using **5** as an example) shows a broad peak at 2θ = 15° due to the amorphous nature of the complex [124], as stated above. A Debye-Scherrer Equation 3.1 [125] was used to determine the size diameter of cys-AgNPs alone and when conjugated to MPcs **3** - **6**. XRD sizes increased from cys-AgNPs = 11.88 nm to **3**-cys-AgNPs = 15.73 nm, **4**-cys-AgNPs = 14.02 nm, **5**-cys-AgNPs =16.87 nm and **6**-cys-AgNPs = 17.08 nm after conjugating of MPcs to cys-AgNPs, Table 3.2. As stated above, Pc molecules are known to form aggregates through π-π stacking [11]. The size increase of conjugates compared to nanoparticle alone could be due to the aggregates of Pc molecules on the surface or on adjacent nanoparticles.

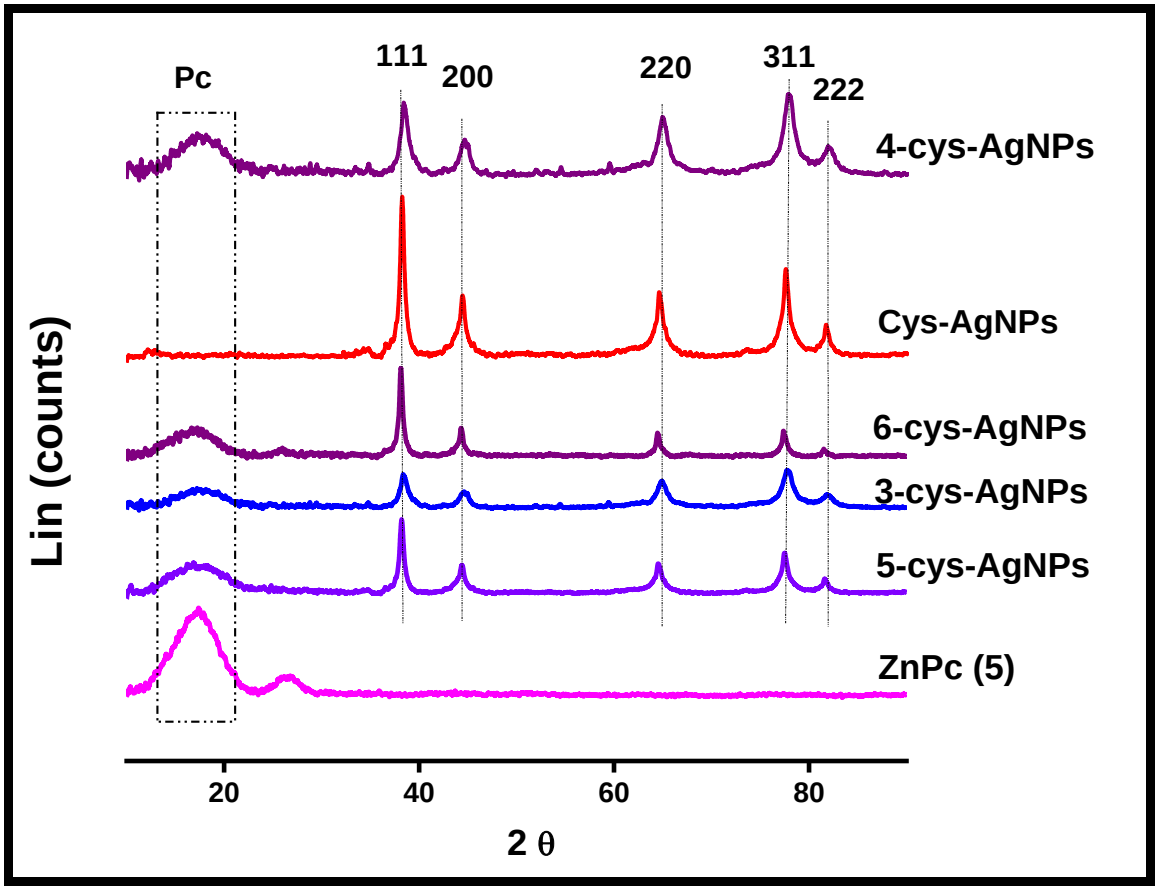

Fig 3.15. XRD patterns of cys-AgNPs and MPc-AgNPs. Complex **5** was used as an example for MPcs.

3.3.2.5 Dynamic light scattering (DLS).

DLS was used to investigate the size distributions of cys-AgNPs together with its MPc-AgNPs conjugates, Fig 3.16. The results indicate an increase in size distribution from 13.98 nm for cys-AgNPs to 17.64 nm for **3**-cys-AgNPs, 17.92 nm for **4**-cys-AgNPs, 18.24 nm for **5**-cys-AgNPs and 18.65 for **6**-cys-AgNPs, Table 3.2, Fig 3.16B (**6**-cys-AgNPs as an example). As stated above, the increase in size on conjugation of MPcs is due to aggregation of MPcs on the nanoparticle surface. The polydispersity index (PDI) of nanoparticles and conjugates were all below 0.3 indicating a good size distribution of cys-AgNPs and MPc-AgNPs. PDI values below 0.7 indicate a lower particle size distribution [126] as in the case of nanoparticles and conjugates. Larger sizes reported through DLS are somewhat expected as compared to sizes reported from other techniques [127], as explained above with AMNPs.

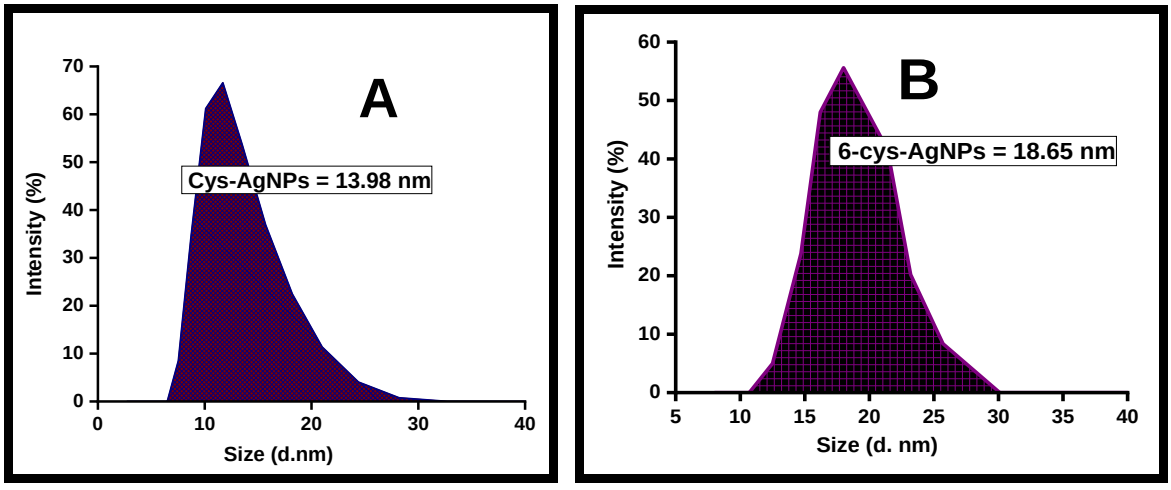

Fig 3.16. DLS micrographs depicting the average size distributions of A) cys-AgNPs (13.98 nm) and B) **6**-cys-AgNPs (18.65 nm) in DMSO.

3.3.2.6 Electronic absorption spectra of MPc-AgNPs conjugates.

Fig 3.17 shows the absorption spectra of MPc-AgNPs in comparison with cys-AGNPs and complex **4** (for representation of MPcs) in DMSO. There was no significant shift in the Q-band of MPc-AgNPs conjugates compared to their MPcs, Table 3.3. Cys-AgNPs alone showed a weak peak at ca. 480 nm due to the surface plasmon resonance (SPR) of metallic AgNPs, Fig 3.17. Linking MPcs to cys-AgNPs resulted in the broadening of the absorption spectra below 550 nm for MPc-AgNPs conjugates due to the SPR band of AgNPs, Fig 3.17.

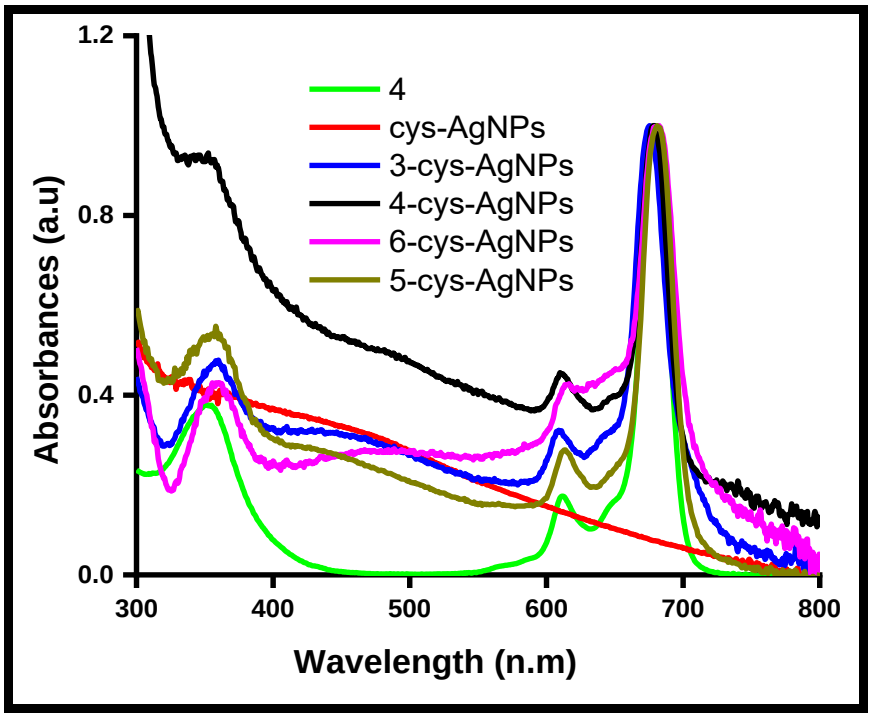

Fig 3.17. Normalized electronic absorption spectra of MPc-AgNPs in DMSO.

3.3.3 Folic acid conjugates.

The conjugation of MPcs **1** - **3** to folic acid (FA) was achieved through an amide bond by linking the COOH of MPcs to NH_2 of FA. Activation of the COOH was achieved using coupling reagents DCC and DMAP, followed by addition of FA to form the covalent amide link between MPcs and FA, Scheme 3.11 using **3** as an example. FTIR, MALDI-TOF, NMR and elemental analysis were used to confirm the chemical linkage of MPcs **1** - **3** to FA. Physically mixtures were also prepared by mixing 2 moles of **1** or **2** with 1 mole FA.

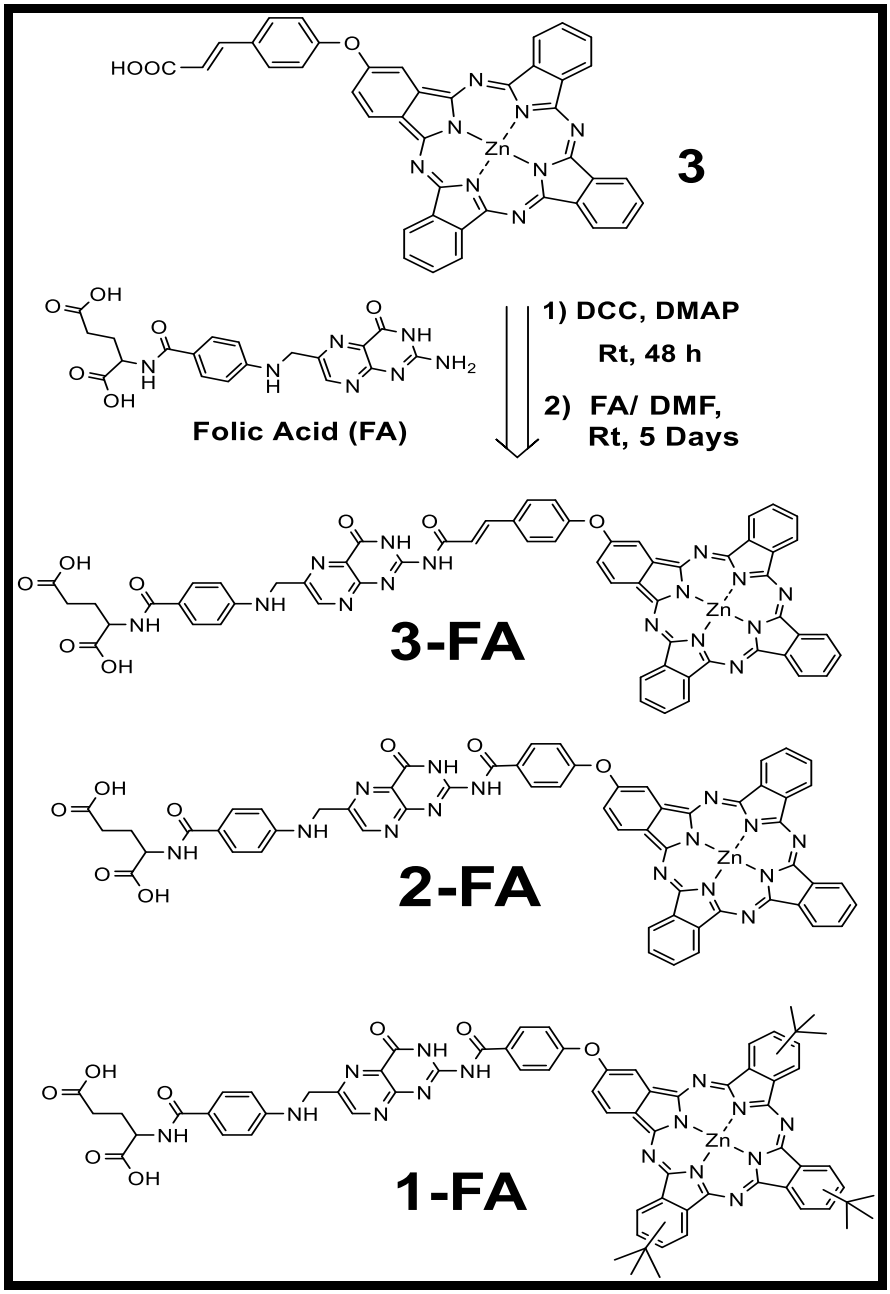

Scheme 3.11. Amide bond linkage between the COOH group of **3** (as an example) and the NH_2 group FA to afford chemically linked **3**-FA. **2**-FA and **1**-FA were also prepared under the same conditions. Rt = room temperature.

The IR spectra of **1**-FA, **2**-FA and **3**-FA showed amide bond (N-H) vibration bends at 1609 cm^{-1}, 1607 cm^{-1} and 1602 cm^{-1}, respectively, Fig 3.18. Primary amino groups are known to show two peaks between 3300-3500 cm^{-1} while secondary amino groups only have one. The disappearance of the two peaks (N-H) on IR for linked conjugates **1**-FA, **2**-FA and **3**-FA is because of chemical bonding between the carboxyl group of MPcs to the amino group of FA. The appearance of a single peak at 3330 cm^{-1} for **3**-FA, 3310 cm^{-1} for **2**-FA and 3334 cm^{-1} for **1**-FA confirms the chemical bonding and formation of an amide bond between the FA-NH_2 and the COOH of MPcs. The amide bond is also indicated by the carbonyl peaks at 1650 cm^{-1} for **3**-FA, 1690 cm^{-1} for **2**-FA and 1693 cm^{-1} for **1**-FA, Fig 3.17. The mass spectra of the conjugates **1**-FA, **2**-FA and **3**-FA gave the masses close to the analytically calculated masses. **1**-FA have an atomic mass unit of 1305 while MALDI-TOF m/z gave 1304 which is one proton less of the analytically calculated amu for **1**-FA. **2**-FA have an analytically calculated mass of 1137 while the MALDI-TOF m/z gave 1138 which is 1 proton extra to the atomic mass unit (amu) of the **2**-FA complex, Fig 3.19 (as an example). **3**-FA have an atomic mass unit of 1163 while the MALDI-TOF m/z recorded 1162, which is one proton less than the calculated mass of the complex.

^1H NMR spectra for **3**-FA, **2**-FA, and **1**-FA in DMSO-d_6 was obtained. The full integration of peaks for **3**-FA, **2**-FA and **1**-FA was difficult to achieve due to overlapping peaks, hence only key peaks were integrated, figure not shown. FA-NH_2 protons alone have a doublet at 6.64 ppm in DMSO-d_6. The upfield chemical shifts of the FA-NH_2 protons from a doublet at 6.64 of FA alone to a singlet peak at

6.91 for NH **3**-FA, 6.94 ppm for NH of **2**-FA and 6.96 for NH of **1**-FA is indicative of the formation of an amide bond with Pc-COOH. The two protons for the carboxylic substituents of FA are retained even in the conjugates but are shifted to 12.04 ppm for **3**-FA, 11.67 ppm for **2**-FA and 11.53 ppm for **1**-FA. The aromatic peaks of **3**-FA, **2**-FA and **1**-FA were observed at chemical shifts between 6.65 ppm to 8.25 ppm for all the MPc-FA conjugates. The shifts in the NMR signal especially for NH protons are an indication of a change in environment, indicating chemical bonding. Elemental analysis of conjugates **1**-FA, **2**-FA and **3**-FA gave atomic percentages close to the analytically calculated values. The elemental analysis results for **1**-FA and **3**-FA agree with observations that Pcs are often isolated as hydrates [115].

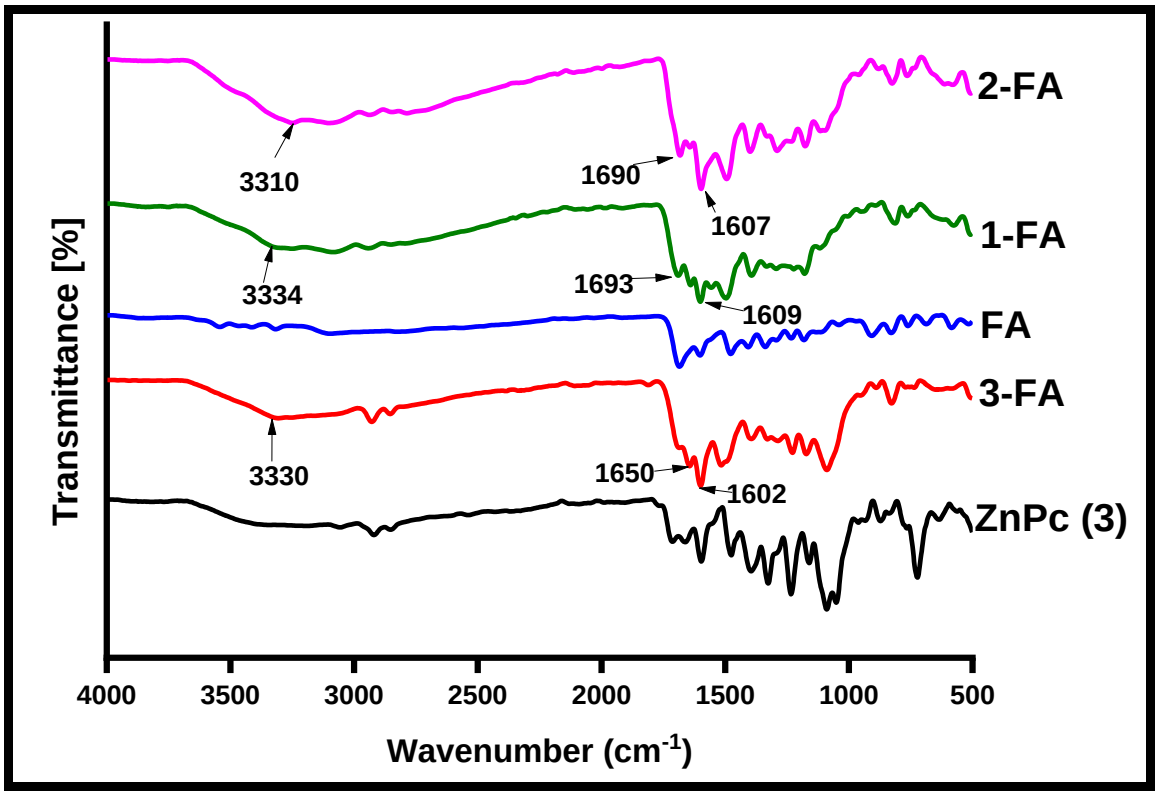

Fig 3.18. FTIR spectra of amide linked MPc-FA conjugates **1**-FA, **2**-FA and **3**-FA.

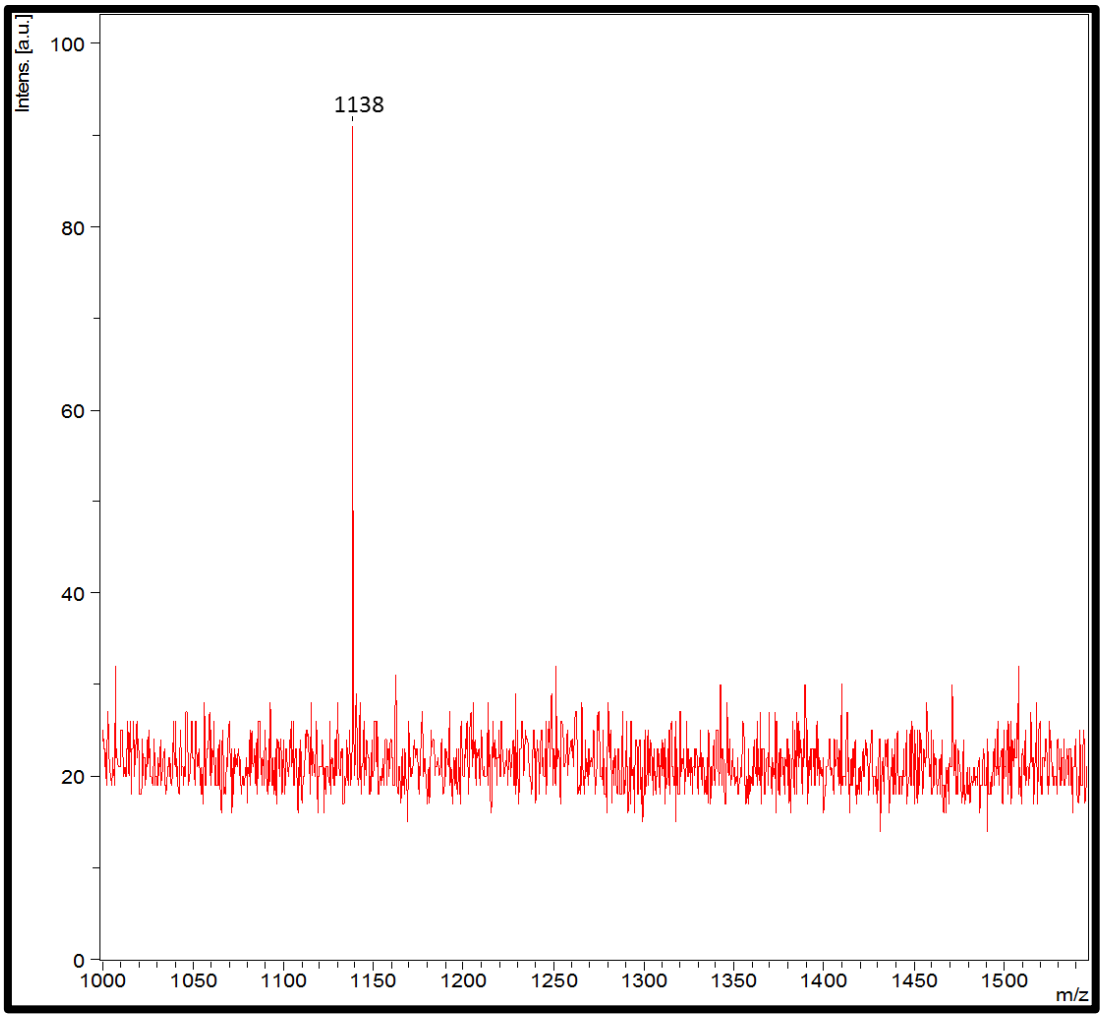

Fig 3.19. MALDI TOF- mass spectra of **2**-FA for illustrative purposes of MPc-FA conjugates.

The Uv/vis absorption spectroscopy was used to study the electronic absorption behavior of complexes in water and DMSO, Fig 3.20. Chemically linked **3**-FA, **2**-FA and **1**-FA were found to be water soluble whereas the physical mixtures (**2**/FA and **1**/FA) were not water soluble. MPcs **1 - 3** are insoluble in water, but upon linkage to FA, the molecules become water soluble, hence the Uv/Vis spectra and singlet oxygen quantum yield for **3**-FA, **2**-FA and **1**-FA were also performed in water since

water solubility is essential for biological applications. The Pc core of **1** - **3** are hydrophobic in nature, their covalent linkage to hydrophilic FA moiety also improves their amphiphilic properties [131].There was an insignificant change in the Q-band of **1**-FA compared to **1, 2**-FA compared to **2** and **3**-FA as compared to **3** in DMSO, Table 3.3. FA has a single absorption peak at 350 nm, Fig 3.20. Upon mixing or linking of MPcs to FA, there was a significant broadening of the B-band caused by the presence of FA in both DMSO and water, Fig 3.20A and B.

The absorption spectra of **1**-FA, **2**-FA and **3**-FA in water shows the broad and split Q-bands. The broad and split Q-bands of MPc-FA in water result from aggregation, typical of Pc complexes through π-π stacking [11,132]. The high energy component of the Q-band result from aggregates while the low energy one is due to the monomer [132], Fig 3.20B. The lower intensity of the Q-band of **1**-FA, **2**-FA and **3**-FA in water is due to aggregation of complexes that is known to lower photoactivity of the molecules through dissipation of energy by the aggregates [133]. The monomer peak was observed at 685 nm for **1**-FA, 690 nm for both **2**-FA and **3**-FA in water, Table 3.3. The Q-band maxima in water are more red-shifted as compared to in DMSO, Table 3.3. The increase in polarity of the solvent has been demonstrated to cause red shifting of the Q-band [134], hence the red shifting of the monomer peak of the Q-band of **1**-FA, **2**-FA and **3**-FA in water compared to DMSO, Table 3.3.

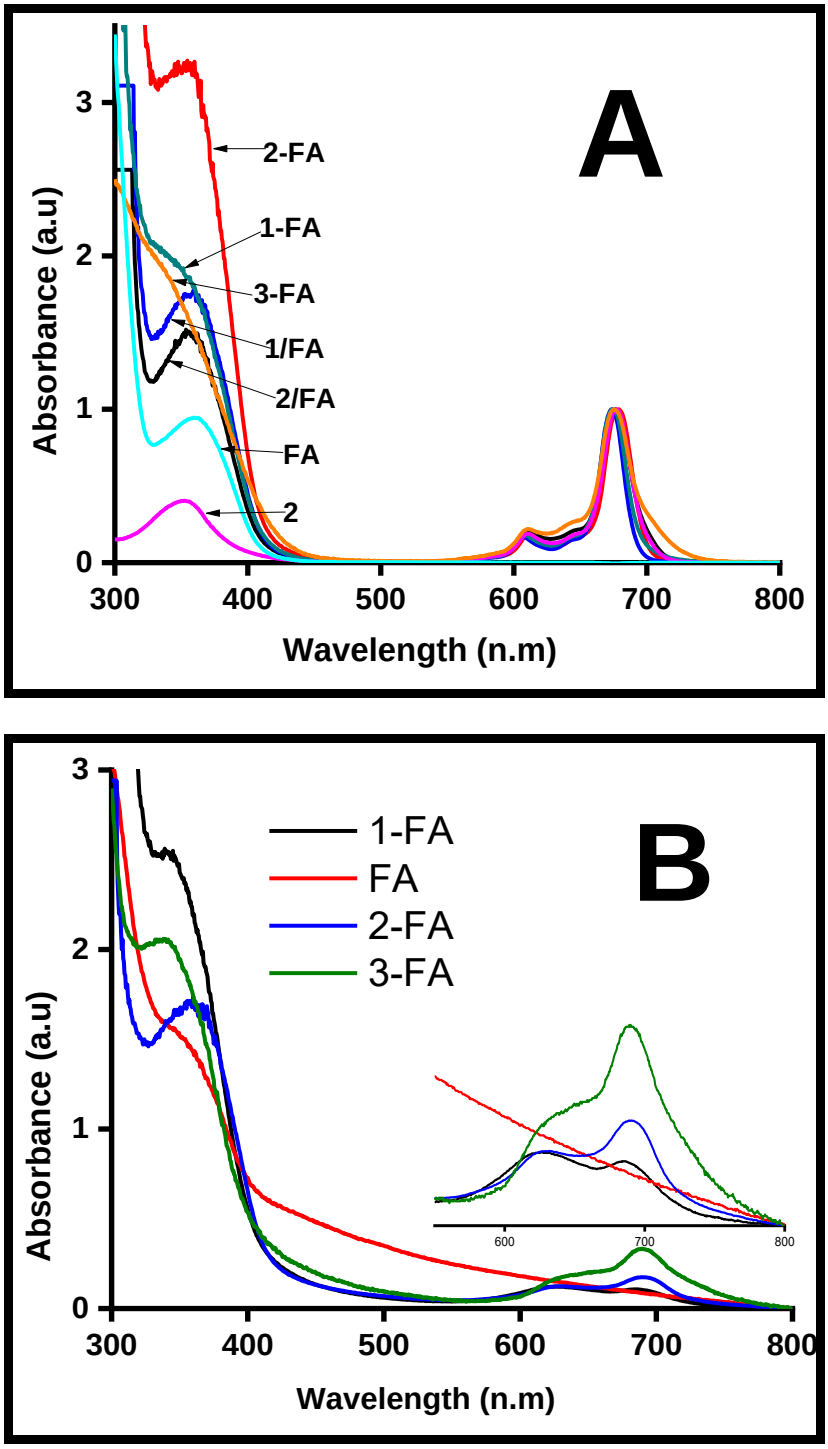

Fig 3.20. Normalized electronic absorption spectra of MPc-FA conjugates in A) DMSO and B) Water.

3.4 SUMMARY.

Asymmetric (**1**-**5**) and symmetrical MPcs (**6**-**7**) were successfully synthesized from cyclotetramerization reaction of phthalonitrile precursors as confirmed using Uv/vis spectroscopy, FTIR, NMR, Mass spectrometry and elemental analysis. MPcs were further linked to magnetic nanoparticles (AMNPs), silver nanoparticles (cys-AgNPs) and folic acid through an amide bond that was confirmed using FTIR. Linking MPcs to FA improved the solubility of MPcs in water. There was an increase in size of nanoparticles after linking MPcs on the surface of nanoparticles, this was confirmed using TEM, DLS and XRD. UV/Vis absorptions of MPcs and conjugates (MPc-AMNPs, MPc-AgNPs and MPc-FA) showed a monomeric Q-band in DMSO while the B-band broadened in the presence of AMNPS, AgNPs or FA. Linked MPc-FA conjugates showed red-shifted and split Q-bands in water due to solvent polarity and aggregation of MPcs, respectively. The water solubility of MPc-FA and the nano-sized MPc-AMNPs and MPc-AgNPs offers a great advantage in biological applications such as PDT and PACT.

CHAPTER 4

PHOTOPHYSICAL AND PHOTOCHEMICAL PROPERTIES

This chapter discusses the photophysical and photochemical properties; fluorescence quantum yield (Φ_{F}) and lifetimes (τ_F), triplet quantum yields (Φ_T) and lifetimes (τ_T) and the singlet oxygen quantum yield (Φ_Δ) of MPcs alone and when conjugated to folic acid, silver or magnetic nanoparticle

4.1 FLUORESCENCE QUANTUM YIELD AND LIFETIMES.

Fig 4.1A and B shows the absorption, excitation, and emission spectra of complex **6** and **6**-cys-AgNPs in DMSO. The Q-band maxima of the absorption and excitation spectra were about the same and mirror images of the emission spectra for both **6** (Fig 4.1A) and **6**-cys-AgNPs (Fig 4.1B). The similarity of the Q-band maxima of the absorption and excitation shows that the nuclear configurations of the ground and excited states are similar and not affected by excitation in DMSO. The same spectra were observed for all other MPcs and their conjugates.

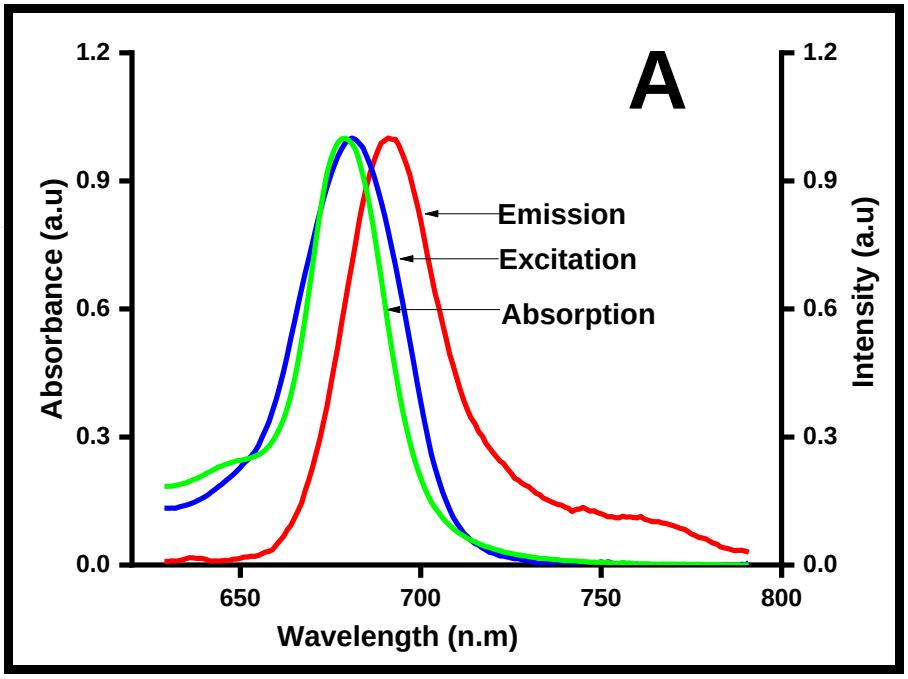

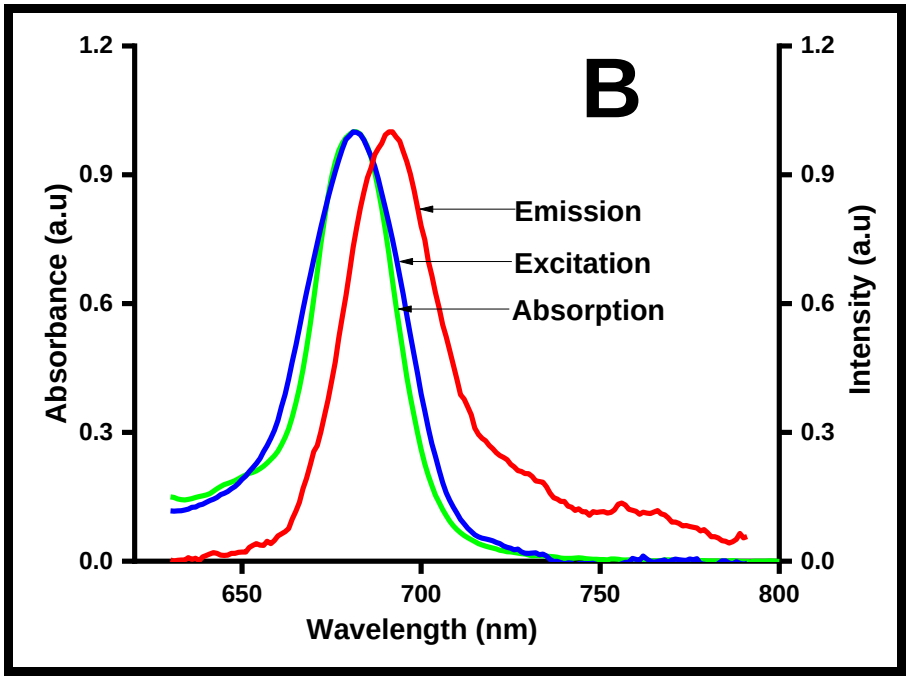

Fig 4.1. Normalized absorption, emission, and excitation of A) ZnTCAPc (**6**) and **6**-cys-AgNPs (as an example) in DMSO.

The fluorescence quantum yields (Φ_F) and lifetimes (τ_F) of MPcs and their conjugates were determined in DMSO using a comparative method with unsubstituted ZnPc ($\Phi_F = 0.20$) in DMSO [98] employed as a standard. Equation 1.1 was used to calculate the Φ_F of MPcs and their conjugates. The Φ_F values were slightly lower compared to that of ZnPc standard, Table 4.1. The fluorescence lifetimes (τ_F) of MPcs and conjugates were recorded on the time correlated single photon counting (TCSPc) setup. All MPcs and conjugates gave a single fluorescence lifetime. τ_F refers to the average time a molecule spends in the excited state before its fluorescence to the ground state. A typical fluorescence decay curve is illustrated in Fig 4.2 (using **1**-AMNPs as an example). The effect of symmetry and

substituents, central metal, metal nanoparticles and folic acid on the Φ_F and τ_F of MPcs are discussed next.

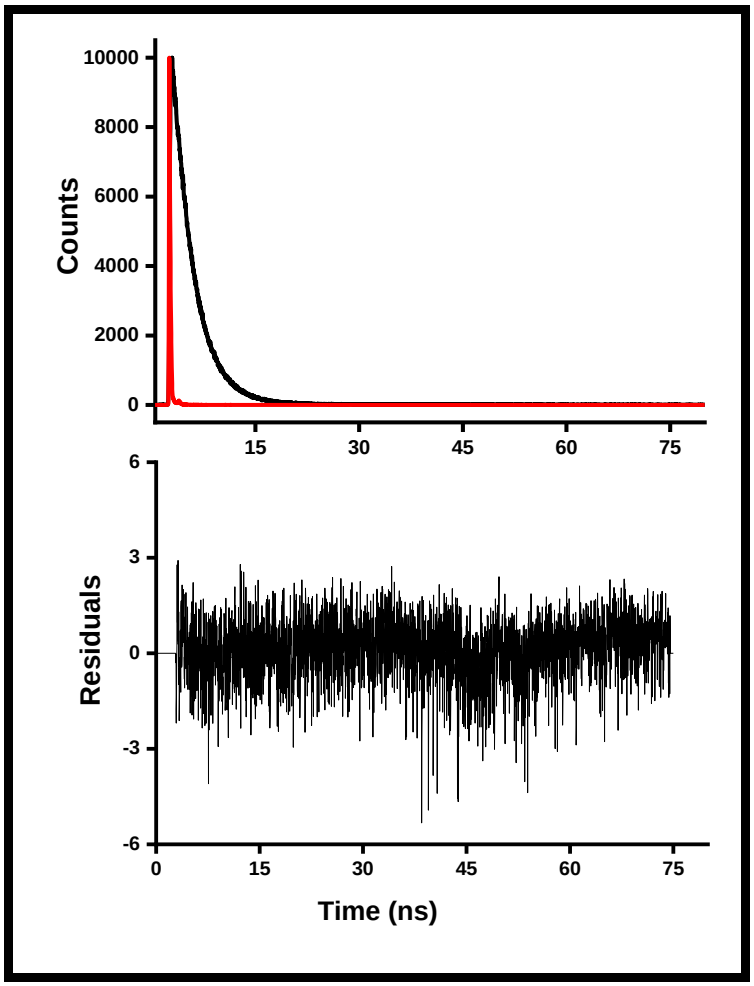

Fig 4.2. Fluorescence decay curve of **1**-AMNPs in DMSO.

Table 4.1. Fluorescence quantum yield and lifetimes of MPcs and conjugates in DMSO.

Complex	Φ_F ± 0.02	τ_F (ns)
1	0.15	3.03
1-FA	0.11	3.02
1/FA mixed	0.17	3.07
1-AMNPs	0.11	3.62
2	0.16	3.14
2-FA	0.13	3.07
2/FA mixed	0.18	3.07
2-AMNPs	0.14	3.02
3	0.18	3.06
3-FA	0.11	2.93
3-AMNPs	0.086	4.66
3-cys-AgNPs	0.08	3.07
4	0.11	3.03
4-AMNPs	0.06	2.95
4-cys-AgNPs	0.05	2.96
5	0.10	2.92
5-cys-AgNPs	0.07	2.99
6	0.13	2.90
6-AMNPs	0.02	2.83

6-cys-AgNPs	0.10	2.77
7	0.05	2.93
7-AMNPs	<0.01	2.83

4.1.1 Effect of metal nanoparticles.

Magnetic nanoparticles (AMNPs) and silver nanoparticles (cys-AgNPs) were both linked to MPcs through an amide bond. MPcs **1** - **4**, **6** and **7** were linked to AMNPs to result in conjugates **1**-AMNPs, **2**-AMNPs, **3**-AMNPs, **4**-AMNPs, **6**-AMNPs and **7**-AMNPs. MPcs **3** - **6** were in addition linked to cys-AgNPs to result in conjugates **3**-cys-AgNPs, **4**-cys-AgNPs, **5**-cys-AgNPs and **6**-cys-AgNPs. Both cys-AgNPs and AMNPs are made up of heavy atoms Ag and Fe, respectively. Heavy atoms (heavy atom effect) encourage spin orbit coupling and population of excited molecules to the triplet excited state through intersystem crossing (ISC), hence the decrease of Φ_F for all MPc-AgNPs and MPc-AMNPs as compared to MPcs alone**,** Table 4.1**.**

There was no significant difference in the Φ_F of **4**-cys-AgNPs compared to **4**-AMNPs and **3**-cys-AgNPs compared to **3**-AMNPs. **6**-AMNPs = 0.02 recorded a lower Φ_F compared to **6**-cys-AgNPs = 0.10, Table 4.1. The paramagnetic nature of AMNPs also influences spin-orbit coupling which further increases the ISC efficiency of the molecules, hence decreasing the Φ_F values of MPcs [135] when linked to AMNPs as is case for **6**-AMNPs compared to **6**-cys-AgNPs, when both are linked to heavy atoms

of nanoparticles. This was not observed for **3** and **4** when linked to both AMNPs and Cys-AgNPs, Table 4.1.

Fluorescence quantum yield and lifetimes have a direct relationship as depicted by a decrease of Φ_F and a shortening of τ_F for MPcs **2**, **4, 6** and **7** with respect to their AgNPs and AMNPs conjugates, Table 4.1. MPcs **1**, **3** and **5** recorded lengthening of τ_F when linked to AMNPs (**1**-AMNPs and **3**-AMNPs) or cys-AgNPs (**5**-cys-AgNPs) even though they had decreased Φ_F. There was no difference in the τ_F of **3**-cys-AgNPs = 3.06 compared to **3** = 3.07. It has been demonstrated that fluorophores (Pc) near metallic particles such as AgNPs and AMNPs may show an unusual fluorescence behaviour (an increased in Φ_F with a shortening of τ_F, or *vice versa*) due to the influence of photonic mode density (PMD) near the fluorophore [136]. In this study, the unusual fluorescence behavior resulted in a decrease in Φ_F with a lengthening of τ_F as in the case of **1**-AMNPs compared to **1**, **3**-AMNPs compared to **3** and **5**-cys-AgNPs compared to **5,** Table 4.1.

4.1.2 Effect of folic acid.

MPcs **1** - **3** were conjugated to folic acid through covalent linkage and as physical mixtures. The covalently linked conjugates are denoted as **1**-FA, **2**-FA and **3**-FA, Scheme 3.11 while the physically mixed conjugates are denoted as **1**/FA and **2**/FA (not done for **3**). **3**-FA = 0.11 had a lower Φ_F compared to **3** = 0.18 while **2**-FA = 0.13 and **1**-FA = 0.11 gave a slightly lower Φ_F compared to **2** = 0.16 and **1** = 0.15, respectively.

For the physical mixtures **1**/FA and **2**/FA, Φ_F did not change within experimental error when compared to their parent MPcs **1** and **2,** respectively. A Lower Φ_F is desirable as it may indicate that a higher percentage of excited molecules populate the excited triplet state through intersystem crossing reducing fluorescence [137].

Decreases and increases in Φ_F when MPcs are in the presence of FA [49,138,139] have been previously reported. It has been reported that following photoexcitation of FA rapid quenching of its singlet excited states by intramolecular electron transfer occurs [140], which could also result in the quenching of the singlet excited states of phthalocyanines when linked to FA. This fast quenching would not occur when the FA and MPcs are physically mixed (where there is less proximity) and not linked, hence Φ_F decreases for linked MPc-FA and no decrease for physical mixtures **1**/FA and **2**/FA.

The τ_F shortened with a decrease in Φ_F for linked MPc-FA conjugates (**1**-FA, **2**-FA and **3**-FA) compared to MPcs **1 - 3**, as expected, Table 4.1. For mixed conjugates (**1**/FA and **2**/FA) compared to their MPcs (**1** and **2**), τ_F lengthened for **1**/FA and shortened for **2**/FA where there was an insignificant increase of Φ_F for **1**/FA and **2**/FA compared to **1** and **2**, respectively. The τ_F of mixed conjugates (**1**/FA and **2**/FA) were the same in relation to their similar Φ_F, Table 4.1.

4.1.3 Effect of symmetry and substituents.

Both symmetrical and asymmetric MPcs were synthesized in this study with target substituents as carboxy phenoxy (**1** - **2**) and cinnamic acid (**3** - **7**). Complex **3** (Φ_F = 0.18) with only cinnamic acid as its substituent had the largest Φ_F followed by **2** (Φ_F = 0.16) with only carboxy phenoxy substituent. MPcs **4** - **7** have other substituents in their rings and recorded lower Φ_F compared to **2** and **3**, Table 4.1. It is likely that the substituents of **4** (*tert*-butyl), **5** (*tert*-butyl phenoxy), **6** and **7** (tetra cinnamic acids) could have quenched the fluorescence resulting in a lower fluorescence quantum yield. MPcs **1** and **2** (both with carboxy phenoxy) recorded no difference on their Φ_F.

4.1.4 Effect of central metal.

Zinc and indium were used as central metals on MPcs **6** and **7**, respectively. Complex **7** recorded a low Φ_F of 0.05 as compared to **6** = 0.13. Indium is a heavier atom than zinc, hence heavy atom effect took precedence increasing the population of molecules to the excited triplet state through intersystem crossing (ISC) [135], which resulted in the very low Φ_F of **7** compared to **6**. Table 4.1. There was no major difference in the τ_F values of **6** = 2.90 ns compared to **7** = 2.93 ns.

4.2 TRIPLET QUANTUM YIELD AND LIFETIMES.

The triplet quantum yields (Φ_T) and lifetimes (τ_T) of MPcs and their conjugates were determined using a comparative method with unsubstituted ZnPc (Φ_T = 0.65 in DMSO) [100] as a standard. Equation 1.2 was used to calculate the Φ_T values of MPcs and their conjugates. The residence time of molecules in the excited state were determined by the triplet lifetime of complexes [141,142]. A typical triplet decay curve of MPcs in DMSO is illustrated in Fig 4.3 with complex **4** for representation purposes. Table 4.2 summarizes the triplet quantum yields and lifetimes of MPcs and their conjugates with comparison to their fluorescence quantum yields.

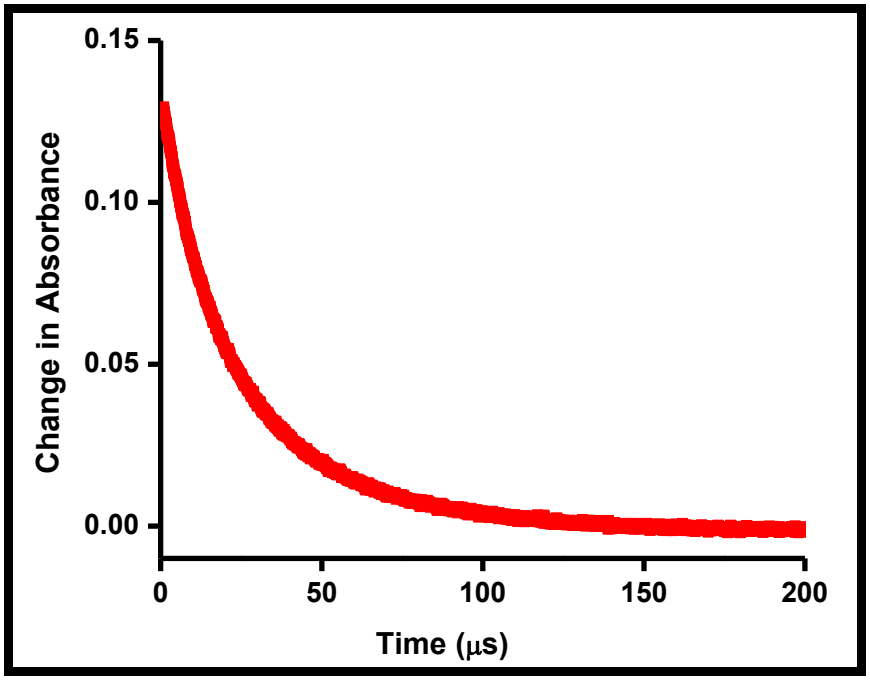

Fig 4.3. Triplet decay curve of complex **4** in DMSO.

Table 4.2. Triplet quantum yield and lifetimes of MPcs and conjugates in DMSO.

Complex	Φ_T ± 0.05	τ_T (μs)	Φ_F ± 0.02
1	0.86	235	0.15
1-FA	0.76	223	0.11
1/FA Mixed	0.69	230	0.17
1-AMNPs	0.87	279	0.11
2	0.62	199	0.16
2-FA	0.68	175	0.13
2/FA Mixed	0.57	238	0.18
2-AMNPs	0.69	256	0.14
3	0.73	258	0.18
3-FA	0.54	206	0.11
3-AMNPs	0.65	224	0.086
3-cys-AgNPs	0.74	249	0.08
4	0.68	199	0.11
4-AMNPs	0.79	221	0.06
4-cys-AgNPs	0.74	179	0.05
5	0.68	221	0.10
5-cys-AgNPs	0.77	186	0.07
6	0.34	241	0.13
6-AMNPs	0.43	272	0.02
6-cys-AgNPs	0.54	215	0.10

7	0.38	158	0.05
7-AMNPs	0.46	229	<0.01

4.2.1 Effect of metal nanoparticles.

MPcs (**2**, **4**-**7)** recorded an improved Φ_T when linked to metal nanoparticles (cys-AgNPs and AMNPs), Table 4.2. The increase in Φ_T is a result of the lower Φ_F and the heavy atom effect of cys-AgNPs and AMNPs when linked to the MPcs. Heavy atom effect encourages ISC of excited molecules to the triplet state as already stated. There was no change in the Φ_T of **1**-AMNPs compared to **1** or **3**-cys-AgNPs compared to complex **3.** The decrease in Φ_T of **3**-AMNPs compared to **3** could be due to aggregation. Complex **3** with a single cinnamic acid substituent and no bulky ligands would be more prone to aggregation. Aggregations formed through π-π stacking can quench the excited triplet state by increasing the nonradiative relaxation rates through intermolecular interactions or other processes sensitive to aggregation (such as internal conversion) [143,144].

Aggregation could also be the reason for the lack of change in Φ_T of **1**-AMNPs compared to **1**. **3**-cys-AgNPs and **6**-cys-AgNPs recorded higher Φ_T compared to **3**-AMNPs and **6**-AMNPs, respectively, while the Φ_T of **4**-cys-AgNPs and **4**-AMNPs were similar within experimental errors.

A lower Φ_F is expected to yield a higher Φ_T as more excited electrons populates through ISC to excited triplet state, but this was not the case with the Φ_T behavior of **6**-cys-AgNPs compared to **6**-AMNPs, Table 4.2. The length of the spacer between the MNPs and porphyrins has been reported to affect photophysical parameters [145,146]. The difference of the length of the spacers (L-cysteine for AgNPs and APTES for AMNPs) could have affected the Φ_T of conjugates. A longer spacer as in the case of APTES compared to a shorter L-cysteine may reduce the interaction between the AMNPs and the MPcs, lowering the heavy atom effect. However, this is not expected to quench the triplet quantum yields. It has also been reported that when porphyrins (similar in structure to MPcs) are anchored on the surface MNPs, aggregates form through π-π stacking (as observed in this work), which may quench the excited triplet state [141]. Thus, this study shows that the heavy atom effect and the paramagnetic nature of the MNPs do not always result in increased triplet state quantum yields, that factors such as spacing between the MPcs and MNPs, and aggregation take precedence.

A higher Φ_T is expected to produce a shorter τ_T [135], as with **4**-cys-AgNPs compared to **4**, **5**-cys-AgNPs compared to **5** and **6**-cys-AgNPs compared to **6**, Table 4.2. There was lengthening of τ_T for MPcs **1**, **2**, **4**, **6**, and **7** when linked to AMNPs. The lengthening in the presence of AMNPs may be caused by the protection of the Pc by the AMNPs. Triplet lifetimes are highly influenced by the environment, especially oxygen which quenches the lifetimes. Since triplet quantum yield studies in this work were performed under inert environment (oxygen deaerated by argon), the only effect left could be the effects of NPs, which could protect the MPcs from any environmental factors, hence improving the lifetime. The shortening of τ_T with a decrease Φ_T for **3**-

AMNPs as compared to **3** may be due to the lowering of the triplet energy and an increase in nonradiative decays [147,148] of MPcs linked to AMNPs.

4.2.2 Effect of central metal.

Complex **7,** with indium as a central metal, had a higher Φ_T = 0.38 as compared to **6** at Φ_T = 0.34 with zinc as a central metal corresponding to the lower Φ_F of the former, due to the heavy atom effect that populated intersystem crossing of molecules to excited triplet state, Table 4.2. Triplet lifetimes shorten when the triplet quantum yield increases, and *vice versa* [135], as with **6** compared to **7** or **6**-AMNPs compared to **7**-AMNPs. The increase of Φ_T and lengthening of τ_T values for **6**-AMNPs compared to **6** and **7**-AMNPs compared to **7** could be due to the protection of MPcs by AMNPs.

4.2.3 Effect of symmetry and substituents.

The triplet quantum yield (Φ_T) of asymmetric MPcs (**1** - **5**) were higher than those of symmetrical MPcs **6** and **7,** Table 4.2. This is expected as the asymmetric nature of MPcs is able to improve ISC to the triplet state [149]. Complex **1** (0.86) gave the highest Φ_T of all the asymmetric MPcs, followed by **3** (0.73), **4** and **5** (0.68) and **2** (0.62), Table 4.2. Complex **1** had a lower Φ_F compared to **3**, hence the higher Φ_T of **1** compared to **3** is due to a higher proportion of excited molecules undergoing intersystem crossing to the excited triplet state.

Carboxy phenoxy MPcs **1** and **2** had the same Φ_F yet **2** (0.62) had a lower triplet quantum yield than **1** (0.86), this could be due to aggregation of MPcs through π-π stacking of the planar rings of **2** as previously explained [144]. Complex **1** has bulky *tert*-butyl groups that reduces aggregation, hence its higher triplet quantum yield compared to **2,** Table 4.2.

Cinnamic acid MPcs **3** - **5** recorded Φ_T that is equivalent within experimental error even though **3** had a higher Φ_F compared to **4** and **5** which could be due to the loss of electronic energy and inefficient ISC by **4** and **5**. Complex **4** and **5** with cinnamic acid and *tert*-butyl substituents recorded the same fluorescence and triplet quantum yields.

Comparing *tert*-butyl containing MPcs (**1**, **4** and **5**), **1** (carboxy phenoxy) recorded a higher fluorescence and triplet quantum yields(Φ_F = 0.15, Φ_T = 0.86) compared to **4** (Φ_F = 0.11, Φ_T = 0.68) and **5** (Φ_F = 0.10, Φ_T = 0.68), both with cinnamic acid substituents, Table 4.2. Cinnamic acid has an extra alkene double bond compared to carboxy phenoxy group, the alkene bonds (olefins) are known to undergo *cis-trans* photoisomerization that leads to nonradiative relaxation [150], hence the lower Φ_T of **4** and **5** compared to **1** with a higher Φ_F. The τ_T of MPcs were longer where the Φ_T was lower, as in the case of **3** compared to **1** as expected [135], Table 4.2.

4.2.4 Effect of folic acid.

The Φ_T of **1**-FA and **3**-FA decreased as compared to **1** and **3**, an increase in Φ_T is expected where there is a decrease in Φ_F, since the two are competing processes. However, this is not observed for **1**-FA and **3**-FA compared to **1** and **3,** respectively, but the expected increase in Φ_T for **2**-FA compared to **2** is observed in Table 4.2. There was also a decrease in Φ_T of **1**/FA and **2**/FA as compared to **1** and **2**. The Φ_T values of linked conjugates **2**-FA and **1**-FA were higher than that of physical mixtures **2**/FA and **1**/FA. Both the reduction or small increases in triplet quantum yields when MPcs are linked to FA [49,138] have been reported. In this work, an increase in Φ_T for **2**-FA compared to **2**, and decreases for **3**-FA compared to **3, 1**-FA and **1**/FA compared to **1** and **2**/FA compared to **2** was observed, Table 4.2.

Aggregation and the disruption of the planarity of macrocyclic ring [144] are some of the reasons for the decrease in triplet quantum yields. τ_T lengthened for **2**/FA where there was a decrease in Φ_T (compared to **2** alone) and a shortening of τ_T with an increase Φ_T for **2**-FA compared to **2**, as expected, Table 4.2. There was a decrease in Φ_T and the shortening of τ_T for **1**-FA and **1**/FA compared to **1**, and **3**-FA compared to **3**. Complex **1** has σ-C-H bonds of *tert*-butyl groups that may experience a “loose bolt” effect [151]. The “loose bolt” effect accelerates internal conversion (IC) by the loss of electronic energy during the vibrations of C-H bonds. The loss of electronic energy reduces the efficiency of ISC and subsequently affecting both the Φ_T and τ_T of conjugates, hence the decrease of Φ_T and τ_T for **1**/FA and **1**-FA, Table 4.2. The decrease in both the triplet quantum yields and lifetimes of **3** following conjugation (**3**-FA), may be due to radiationless pathways.

4.3 SINGLET OXYGEN QUANTUM YIELDS.

The ability of MPcs and their conjugates to generate singlet oxygen species was evaluated using a chemical method. Equation 1.4 was used to calculate the singlet oxygen quantum yield with unsubstituted ZnPc (Φ_Δ= 0.67 in DMSO) [104] and $AlPcS_{mix}$ (Φ_Δ = 0.34 in aqueous media) [105] used as reference standards. DPBF and ADMA were used as quenches with ZnPc and $AlPcS_{mix}$ standards, respectively. The rate of photodegradation of ADMA or DPBF was monitored by Uv/Vis spectra, Fig 4.4 using the degradation of DPBF by **6**-cys-AgNPs for illustrative purposes. Triplet and singlet oxygen quantum yields are related since the latter are a result of the former interacting with ground state molecular oxygen.

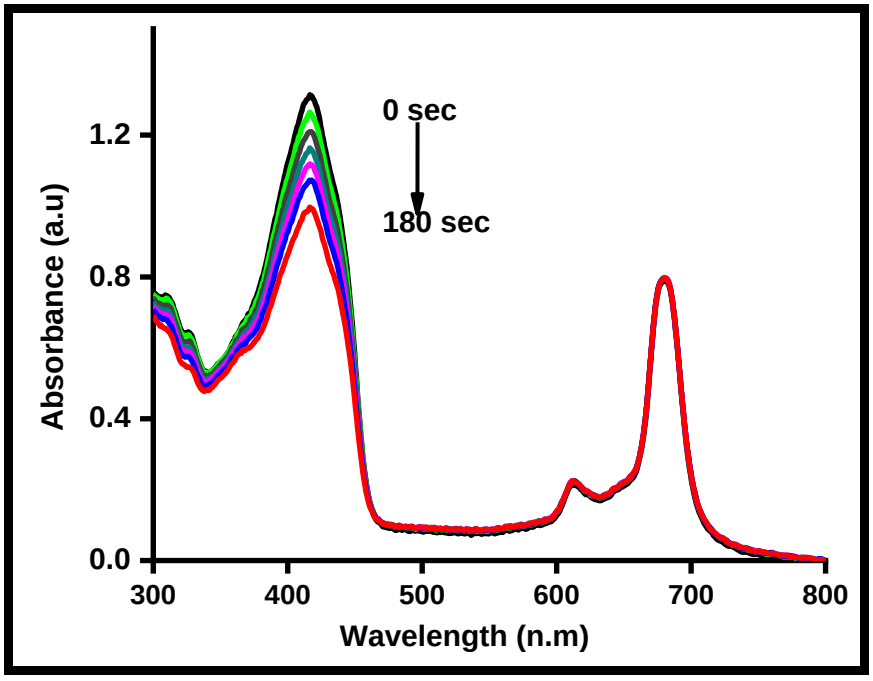

Fig 4.4. Photodegradation of DPBF using **6**-cys-AgNPs (as an example) in DMSO at 30 s interval.

Table 4.3. Singlet oxygen quantum yields of MPcs and conjugates in DMSO.

Complex	Φ_Δ ± 0.02	Φ_T ± 0.05
1	0.59	0.86
1-FA	0.47 (0.12)	0.76
1/FA Mixed	0.42	0.69
1-AMNPs	0.47	0.87
2	0.56	0.62
2-FA	0.61 (0.17)	0.68
2/FA Mixed	0.54	0.57
2-AMNPs	0.51	0.69
3	0.48	0.73
3-FA	0.41 (0.15)	0.54
3-AMNPs	0.38	0.65
3-cys-AgNPs	0.59	0.74
4	0.56	0.68
4-AMNPs	0.59	0.79
4-cys-AgNPs	0.63	0.74
5	0.59	0.68
5-cys-AgNPs	0.67	0.77
6	0.26	0.34
6-AMNPs	0.33	0.43

6-cys-AgNPs	0.45	0.54
7	0.30	0.38
7-AMNPs	0.37	0.46

Values in brackets represents singlet oxygen quantum yields in water

Singlet oxygen is generated when ground state molecular oxygen interacts with the excited triplet state of MPcs, hence a higher Φ_Δ is expected from a higher Φ. The Φ_Δ of asymmetric MPcs **1** - **5** were higher than those of symmetrical MPcs **6** and **7** due to their higher Φ_T, Table 4.3. Complex **7** also recorded a higher Φ_Δ compared to **6** due to a higher Φ_T of **7** compared to **6**. Asymmetric complex **3**, with a higher triplet quantum yield compared to asymmetric **2**, **4** and **5** recorded a lower singlet oxygen quantum yield compared to **2**, **3** and **5**, Table 4.3. The lower Φ_Δ of **3** could be due to nonradiative pathways.

MPc-AgNPs recorded a higher Φ_Δ compared to their MPcs due to their higher Φ_T, Table 4.3. MPc-AMNPs conjugates (**4**-AMNPs, **6**-AMNPs and **7**-AMNPs) also recorded higher Φ_Δ in relation to their higher Φ_T compared to their MPcs. A decrease in Φ_Δ was observed for **1**-AMNPs, **2**-AMNPs and **3**-AMNPs compared to **1**, **2** and **3,** respectively. The decrease in the Φ_Δ for the conjugates (**1**-AMNPs, **2**-AMNPs and **3**-AMNPs) could be due to the screening effect caused by AMNPs which could have prevented the interaction of the excited triplet state of nanoconjugates and the ground state molecular oxygen [152] resulting in the insufficient energy transfer from the excited triplet state to the molecular oxygen.

Higher singlet oxygen quantum yields were obtained for **3**-cys-AgNPs and **6**-cys-AgNPs compared to **3**-AMNPs and **6**-AMNPs owing to their higher triplet quantum yields, Table 4.3. **4**-cys-AgNPs had a higher Φ_Δ as compared to **4**-AMNPs even though **4**-AMNPs had a higher Φ_T than **4**-cys-AgNPs. The larger sized AMNPs (DLS = 16.45 nm) compared to cys-AgNPs (DLS = 13.98 nm), may screen off the energy transfer to molecular oxygen [152] as previously explained.

Linked **1**-FA and **2**-FA conjugates showed a larger Φ_Δ compared to physically mixed conjugates **1**/FA and **2**/FA owing to their higher triplet quantum yield, Table 4.3. **3**-FA recorded a lower Φ_Δ compared to **3** corresponding to the lower Φ_T value while **2**-FA had both its triplet and singlet oxygen quantum yield improved when compared to **2**. The Φ_Δ studies of water soluble MPc-FA conjugates (**1**-FA, **2**-FA, and **3**-FA) were also conducted in aqueous solutions, Table 4.3. Quenching of the excited triplet state of porphyrin type complexes in water is common and that decreases their Φ_Δ [153], hence values are low in water compared to DMSO. The ability of these complexes to generate singlet oxygen in water, makes them suitable candidates for biological application as photosensitizers. The Φ_Δ values in water (Table 4.3) are still high enough for PDT applications since PDT photosensitizers in clinical trials such as LUTRIN have Φ_Δ values as low as 0.11 [28].

4.4 SUMMARY.

The photophysical and photochemical properties of MPcs and their conjugates were performed in DMSO using a comparative method with unsubstituted ZnPc as a standard. Fluorescence quantum yield of most MPcs decreased when linked to AMNPs and cys-AgNPs due to heavy atom effect of metal nanoparticles. The lower Φ_F values mostly resulted in higher Φ_T and Φ_Δ due to ISC of excited molecules because of heavy atom effect of AMNPs and cys-AgNPs. The heavy atom effect also improved the Φ_T and Φ_Δ of InPc (**7**) compared to ZnPc (**6**), both symmetrical. The undesired triplet and singlet oxygen quantum yields recorded for MPcs **1** - **3** compared to their MPc-AMNPs and MPc-FA conjugates, could be caused by aggregation of MPcs, possible nonradiative relaxation processes and poor interaction of molecular oxygen with the excited triplet state. Linked MPc-FA conjugates were observed to have better singlet oxygen quantum yields than physically mixed MPc/FA conjugates. In addition, the ability of linked MPc-FA to generate singlet oxygen quantum yields in water makes them ideal photosensitizers for PDT. Asymmetric MPcs (**1**-**5**) and their conjugates recorded better photosensitizing properties than symmetrical MPcs (**6**,**7**) and their conjugates.

CHAPTER 5

PHOTODYNAMIC THERAPY

This chapter outlines the *in vitro* dark cytotoxicity and photodynamic therapy activity of MPcs when alone and when conjugated to folic acid, silver, and magnetic nanoparticles on MCF-7 breast cancer cells. MPcs **2** - **4, 6** and **7** and conjugates **2**-FA, **3**-FA, **2**-AMNPs, **3**-AMNPs, **4**-AMNPs, **4**-cys-AgNPs, **6**-AMNPs and **7**-AMNPs were tested for their cytotoxicity on MCF-7 cells.

5.1 PDT STUDIES ON MCF-7 CELLS.

5.1.1 Control studies.

Control studies were conducted with 1.6% DMSO in culture media (DMEM), marked as zero concentration of MPcs and conjugates, Fig 5.1. DMSO (1.6%) did not show any cytotoxic effect on MCF-7 cells when tested both in the dark and under light, Fig 5.1. AMNPs and FA alone showed no dark cytotoxicity and minimal PDT activity on MCF-7 breast cancer cells when studied at different concentrations, Fig 5.1 and 5.2, respectively.

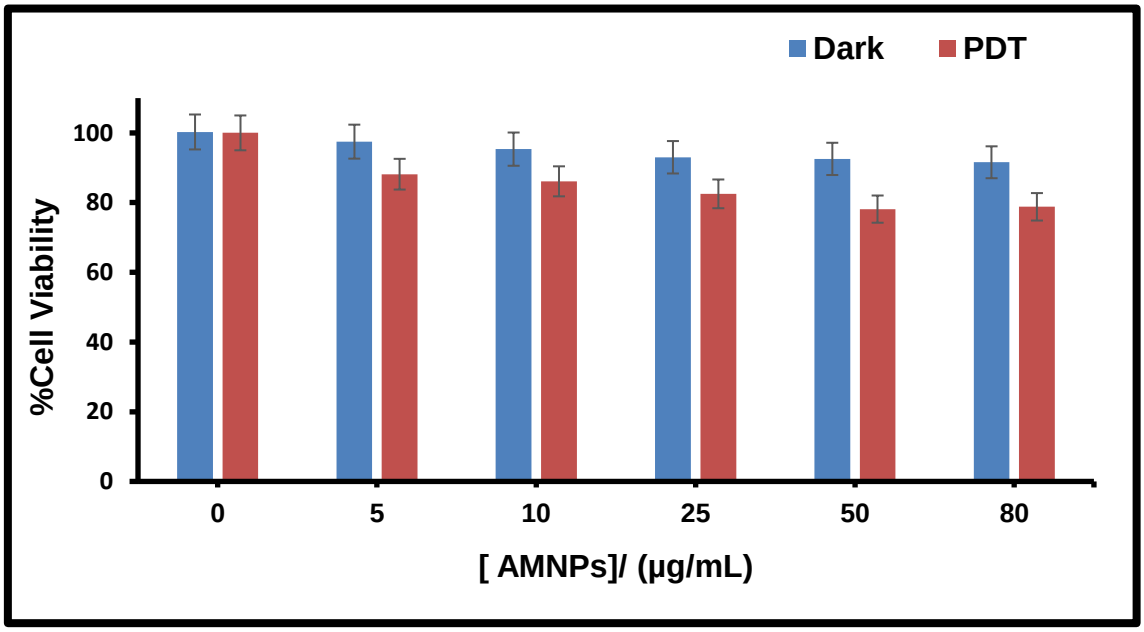

Fig 5.1. Dark cytotoxicity and PDT activity of 1.6% DMSO in culture media (0 µg/mL) and AMNPs alone (5-80 µg/mL) on MCF-7 cells.

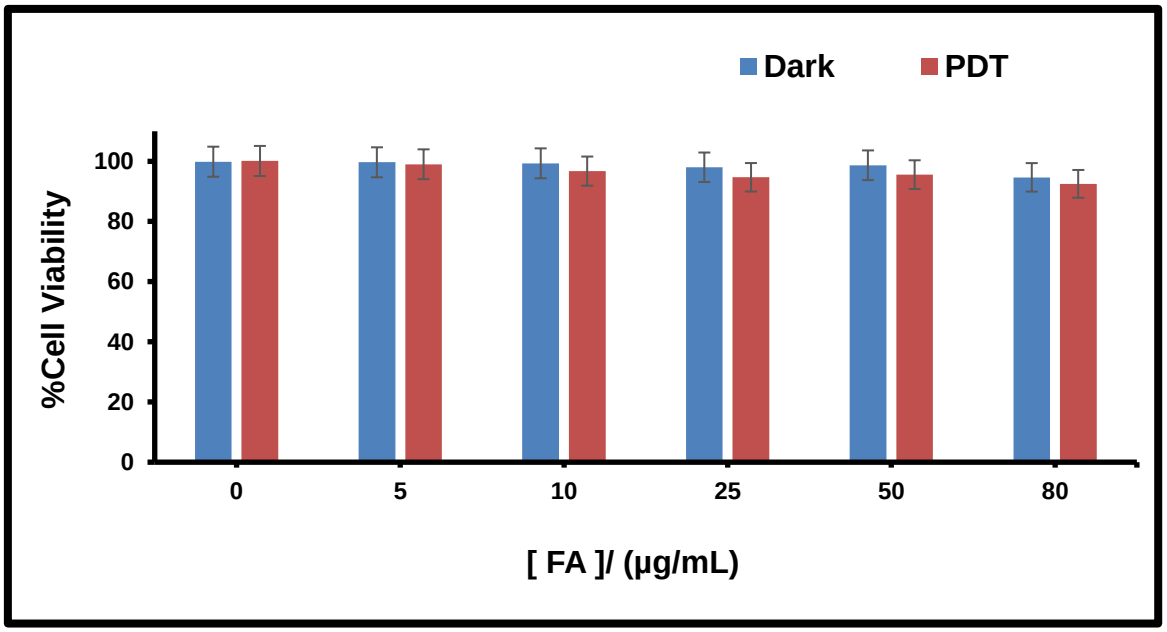

Fig 5.2. Dark cytotoxicity and PDT activity of 1.6% DMSO in culture media (0 µg/mL) and FA alone (5-80 µg/mL) on MCF-7 cells.

5.1.2 MPc-NPs conjugates.

5.1.2.1 *In vitro* dark cytotoxicity studies.

Dark cytotoxicity studies of PS agents (MPcs and conjugates) on MCF-7 cells are summarized in Table 5.1. At gradient concentrations, MPcs and conjugates were found to have low cytotoxicity in the dark, Fig 5.3 (complex **7** and **7**-AMNPs as examples) and Fig 5.4 with **4**, **4**-cys-AgNPs and **4**-AMNPs. More than 85% of cell viabilities were recorded below 50 µg/mL for both MPcs and conjugates, indicating very low cytotoxic effect in the dark, Fig 5.3A and B. The low cytocidal effect of MPcs and conjugates in the dark is demonstrated by ≥70% cell viability after treatment with 80 µg/mL, as shown in Table 5.1.

Fig 5.5B micrographs also depicts the low cytocidal effect of 80 µg/mL of **6**-AMNPs after dark treatment, as an example. Cell confluence of the viable cells after treatment (Fig 5.5B) is equivalent to that of 1.6% DMSO, Fig 5.5A, indicating low dark cytotoxicity of PS agents. There was a decrease in dark cytotoxicity of asymmetrical MPcs **2** - **4** when conjugated to nanoparticles compared to symmetrical MPcs **6** and **7** as highlighted on Table 5.1, proving the importance of symmetry in PDT. The low cytotoxic effect of MPcs and conjugates in the dark is desirable as it indicates poor chemotherapeutic effect of photosensitizers.

5.1.2.2 *In vitro* photodynamic therapy studies.

The efficacy of MPcs and conjugates as PS agents were evaluated at different concentration (5–80 µg/mL) at irradiation dosimetry of 150 J/cm^2 for **4**, **4**-cys-AgNPs and **4**-AMNPs and 170 J/cm^2 **2**, **3**, **6**, **7**, **2**-AMNPs, **3**-AMNPs, **6**-AMNPs and **7**-AMNPs. The different irradiation doses were used due to availability of the light sources (Modulight). There was an increase in the PDT activity with an increase in the administered concentration for all MPcs and conjugates as illustrated on Fig 5.3A and B, with complex **7** and **7**-AMNPs as examples and Fig 5.4 with **4**, **4**-cys-AgNPs and **4**-AMNPs at 80 µg/mL. The difference in cell death is also demonstrated by cell confluence of viable cells on Fig 5.5C and D micrographs at 5 µg/mL and 80 µg/mL of **6**-AMNPs as examples, respectively, after PDT treatment. Less cell death at 5 µg/mL is demonstrated by the resulting higher cell confluence of viable cells on Fig 5.5C, while a high cell death at 80 µg/mL of MPcs and conjugates is demonstrated by very low cell confluence of viable cells on Fig 5.5D.

PS agents generates singlet oxygen when irradiated with a beam of laser light, which is responsible for the cytotoxic killing of cancer cells, hence there is a sharp decline of viable cells after PDT treatment as opposed to dark cytotoxicity, Table 5.1. Complex **4** recorded the lowest cell viability of all MPcs alone at 80 µg/mL concentration even though low dosimetry was used. The lower cell viability is due to the higher singlet oxygen quantum yield of **4** compared to **3**, **6** and **7,** Table 5.1. In addition, the presence of bulky *tert*-butyl substituents could have prevented aggregation of complex **4** within the cells when also compared to other asymmetric MPcs **2** and **3** that only have carboxy phenoxy and cinnamic acid substituents only.

2-AMNPs and **3**-AMNPs recorded a lower PDT activity compared to their parent MPcs **2** and **3** due to their lower Φ_Δ, Table 5.1. There was also a decrease in the PDT activity for **4** =24.01% to **4**-cys-AgNPs = 31.42% and **4**-AMNPs = 35.28% even when the conjugates had higher singlet oxygen than **4**, Table 5.1. A similar decrease in PDT activity (increase in cell viability) was observed for **6**-AMNPs compared to **6** and **7**-AMNPs compared to **7,** which had higher Φ_Δ than MPcs (**6** and **7**).The decrease of the PDT activity for conjugates could be due to the slow *in vitro* dissolution rate of nanoparticles in physiological media such as DMEM that is known to affect their bioavailability [154,155], which could affect their efficacy as in the case of **4**-AMNPs, **4**-cys-AgNPs, **6**-AMNPs and **7**-AMNPs.

There was no major difference between the PDT activity of **4**-cys-AgNPs compared to **4**-AMNPs, although the former had a higher singlet oxygen quantum yield, Fig 5.4, and Table 5.1. Even though the PDT activity decreased for some conjugates, nanoparticles can still play an important role of improving delivery of MPcs and conjugates at the tumour side through the EPR effect or in targeted combination therapy as contrast agents in magnetic resonance imaging (MRI) (AMNPs) and therapeutic agents hyperthermia systems [156].

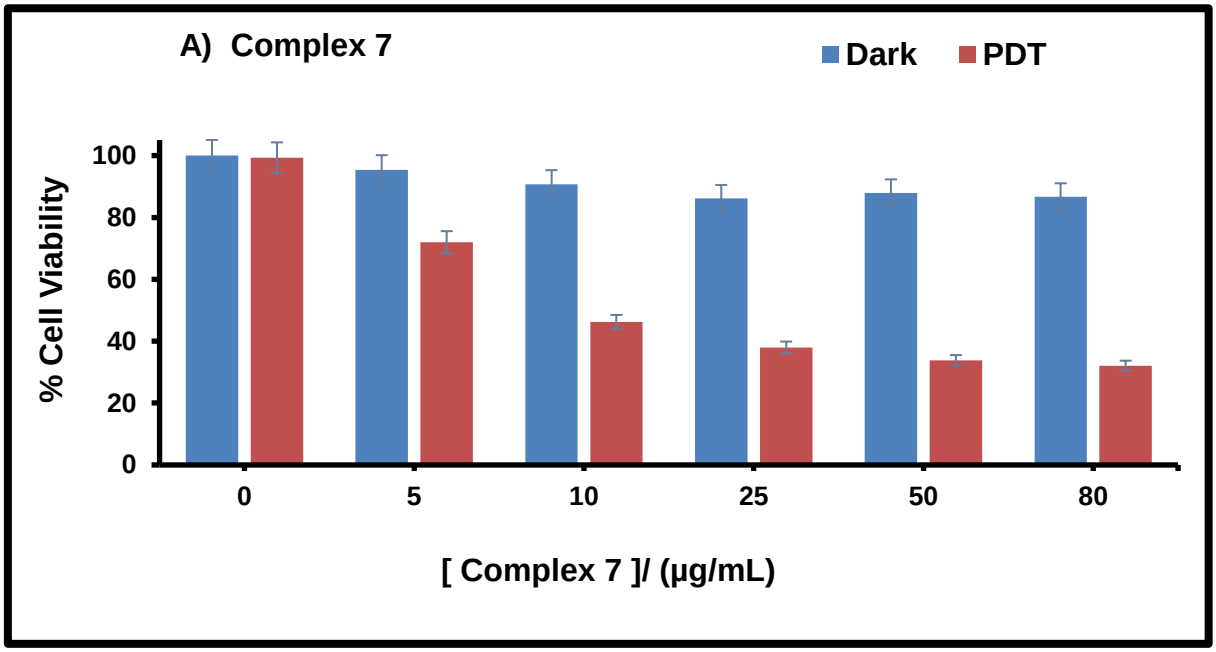

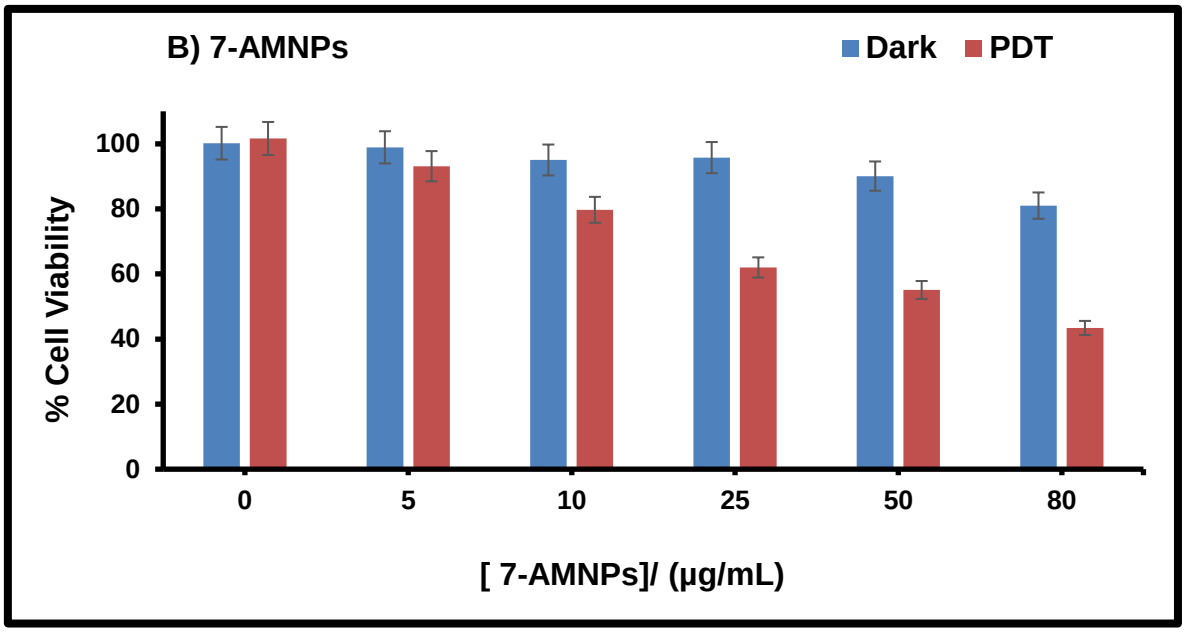

Fig 5.3. Dark cytotoxicity and PDT activity of (A) complex **7** and (B) **7**-AMNPs on MCF-7 at gradient concentrations. Zero concentration represent control media.

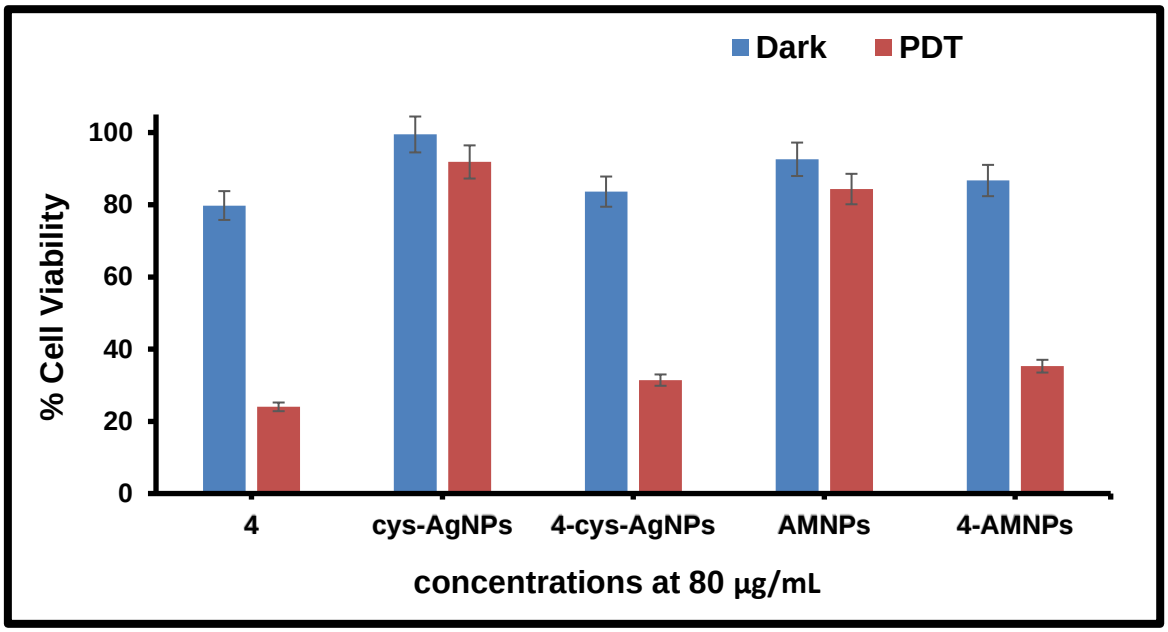

Fig 5.4. Dark cytotoxicity and PDT activity of complex **4** and its conjugates at 80 µg/mL on MCF-7 cells.

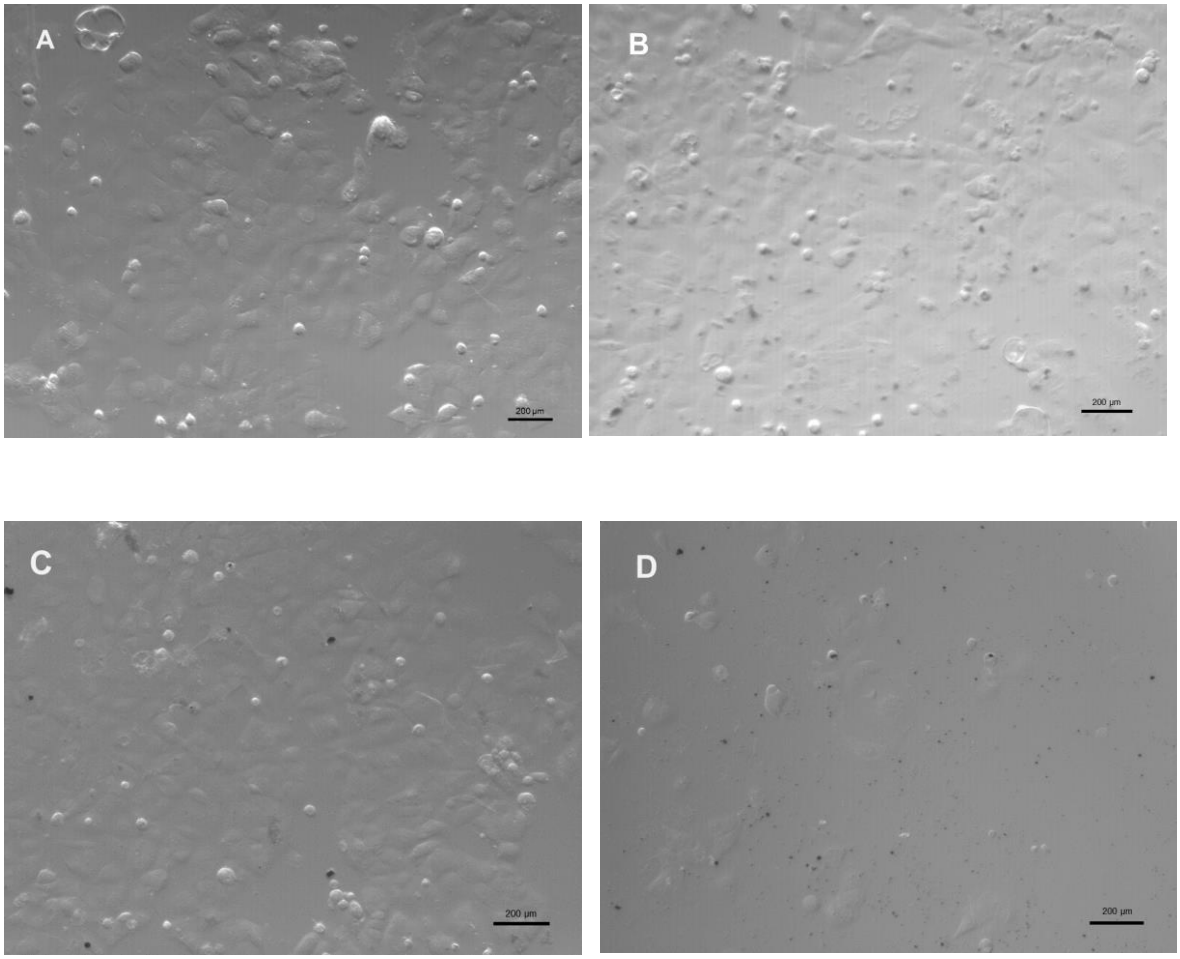

Fig 5.5. Micrographic representation of MCF-7 carcinoma cells after treatment with A) 1.6% DMSO, B) 80 µg/mL of **6**-AMNPs after dark cytotoxicity treatment, C) 5 µg/mL of **6**-AMNPs after PDT treatment and D) 80 µg/mL of **6**-AMNPs after PDT treatment.

Table 5.1. Percentage cell viabilities of MCF-7 cells at 80 μg/mL for the MPcs and conjugates in comparison to their singlet oxygen quantum yield.

MPcs/Conjugates	% cell viability (dark)	% cell viability (light)	Φ_Δ
2	69.98 ± 4.02	31.39 ± 3.59	0.56
2-AMNPs	91.03 ± 2.98	43.91 ± 1.52	0.51
3	77.73 ± 3.50	37.29 ± 1.86	0.48
3-AMNPs	88.34 ± 3.98	45.64 ± 2.28	0.36
4	79.78 ± 3.59	24.01 ± 1.20	0.56
4-cys-AgNPs	83.63 ± 4.81	31.42 ± 1.57	0.63
4-AMNPs	86.72 ± 4.34	35.28 ± 1.75	0.59
6	86.71 ± 4.34	32.10 ± 1.61	0.26
6-AMNPs	81.02 ± 4.05	43.41 ± 2.17	0.33
7	86.72 ± 3.56	32.10 ± 1.18	0.30
7-AMNPs	81.02 ± 3.74	43.40 ± 2.32	0.37

*Energy of the irradiation light was 150 J/cm^2 for **4** and its conjugates and 170 J/cm^2 for **2**, **3**, **6**, **7** and their conjugates.

5.1.3 MPc-FA conjugates.

5.1.3.1 *In vitro* dark cytotoxicity studies.

The *in vitro* dark cytotoxicity of complexes **2**, **3**, **2**-FA and **3**-FA against MCF-7 cells was evaluated at gradient concentrations, Fig 5.6 with **2**-FA as an example. MPcs and conjugates concentrations of ≤80 µg/mL accounted for more than 80% viable cells showing minimal dark cytotoxicity, Fig 5.6. Comparison of the dark cytotoxicity of FA conjugates and AMNPs conjugates is illustrated on Fig 5.7. The linkage of MPcs **2** and **3** to FA and AMNPs afforded reduced *in vitro* dark cytotoxicity of **2** and **3**, Fig 5.7. **2**-AMNPs was the least toxic with 93% cell viability in the dark while **3**-AMNPs, **3**-FA, **2**-FA accounted for >80% cell viability at 80 µg/mL, Fig 5.7. The low *in vitro* dark cytotoxicity of MPcs and conjugates was also observed in the overall cell confluence in the micrographs, Fig 5.8B using **3**-FA as an example, where the number of viable cells is almost close to those of control studies alone, Fig 5.8A.

5.1.3.2 *In vitro* photodynamic therapy studies.

Photodynamic therapy (PDT) activity of complexes on MCF-7 cells was evaluated in triplicates at a fixed irradiation dosimetry of 170 J/cm^2. PDT activity of MPcs and conjugates increased with an increase in concentration, Fig 5.6 with **2**-FA as an example. Fig 5.8C and D depicts the confluence of viable cells differences after PDT treatment. There was a significant loss of viable cells at highest concentrations after treatment of light as compared to cell viability data obtained in the dark which shows

that MPcs and conjugates under study are more potent as PS agents than they are as chemotherapeutic agents.

FA containing conjugates (**2**-FA and **3**-FA) recorded a better PDT activity on MCF-7 cells compared to AMNPs conjugates (**2**-AMNPs and **3**-AMNPs) as illustrated at their highest concentration (80 µg/mL) recording <40% viable cells compared to >40% cell viable cells for AMNPs conjugates, Fig 5.7. The Φ_{Δ} of **3**-FA = 0.41 is higher than **3**-AMNPs = 0.38. The same applies to **2**-FA at 0.61 which is higher than **2**-AMNPs at 0.51 in DMSO. Thus, the PDT activity is aligned with the higher singlet oxygen quantum yields of MPc-FA compared to MPc-AMNPs. Furthermore, the ability of **2**-FA and **3**-FA to generate singlet oxygen in water is thought to have improved the PDT activity and cytotoxic efficiency of PS agents. Targeted drug delivery by AMNPs is through EPR effect as previously explained while FA targeting is through high affinity binding of FA with folate receptors which are expressed on human cancer cells [157], hence improving bioavailability of FA conjugates on the cancer cells while improving PDT activity.

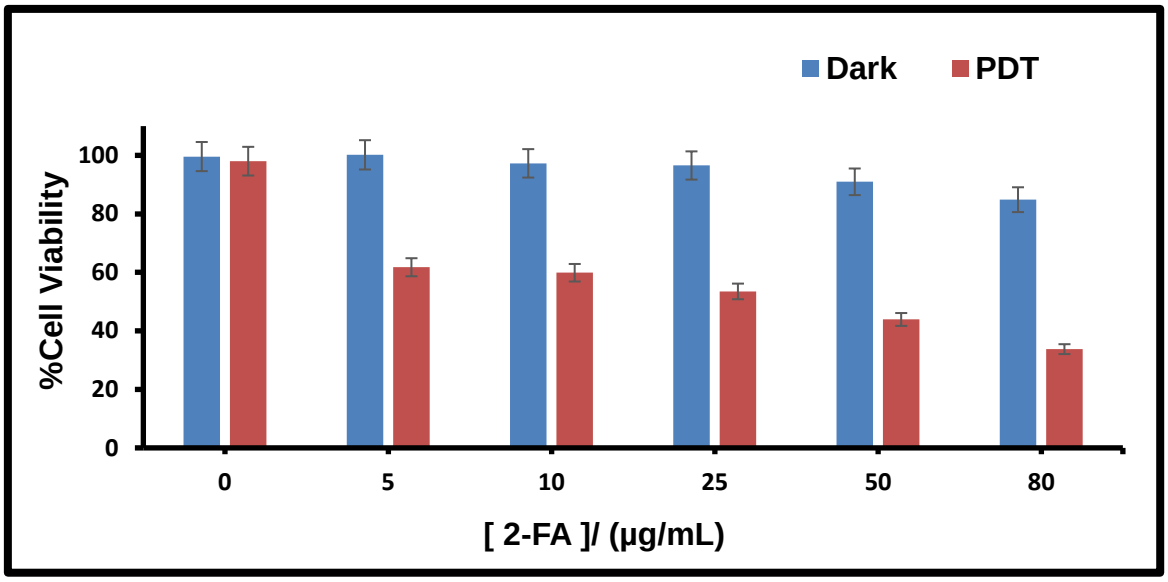

Fig 5.6. PDT activity and dark cytotoxicity of **2**-FA at different concentrations (as a representative). Control studies are represented by 0 µg/mL concentration.

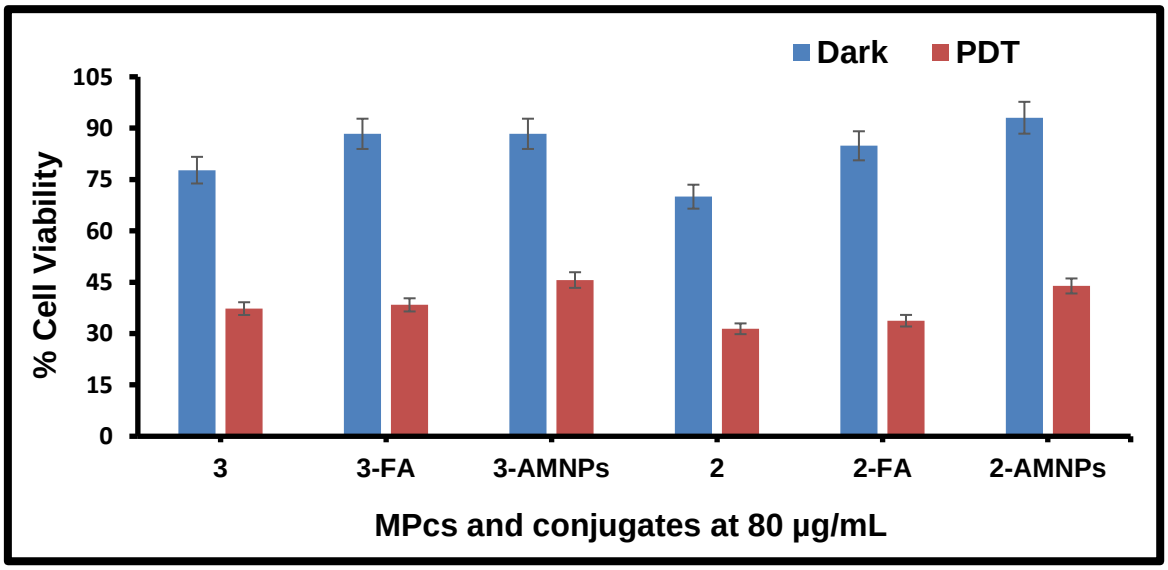

Fig 5.7. Dark cytotoxicity and PDT activity of **2**, **3**, **2**-AMNPs, **2**-FA, **3**-AMNPs and **3**-FA on MCF-7 cells at 80 µg/mL.

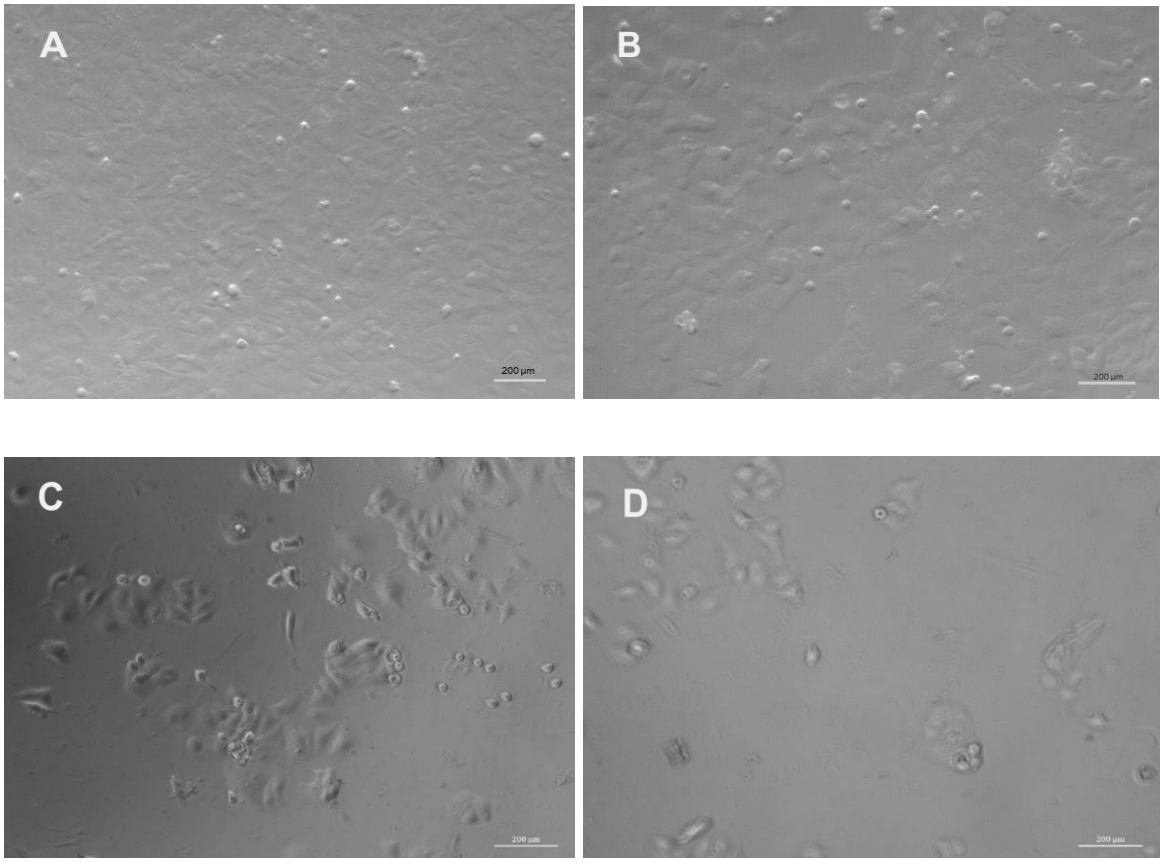

Fig 5.8. Photomicrographs of MCF-7 carcinoma cells for A) 1.6% DMSO after PDT treatment, B) 80 µg/mL of **3**-FA after dark cytotoxicity treatment C) 5 µg/mL of **3**-FA after PDT treatment and D) 80 µg/mL of **3**-FA after PDT treatment. Scale bar = 200 µm.

5.2 SUMMARY.

The *in vitro* dark cytotoxicity and PDT activity of MPcs and conjugates (MPc-FA, MPc-AMNPs and MPc-AgNPs) were tested on MCF-7 breast cancer cells at different concentrations. There was a low *in vitro* cytocidal effect of MPcs alone (**2**, **3**, **4**, **6** and **7**) and conjugates (**2**-AMNPs, **2**-FA, **3**-AMNPs, **3**-FA, **4**-AMNPs, **4**-cys-AgNPs, **6**-AMNPs and **7**-AMNPs) in the dark as compared to their PDT activity on MCF-7 cells. The PDT activity increased with an increase in concentration of MPcs and conjugates.

At 80 µg/mL, MPcs **2** and **3** alone recorded better PDT activity than their conjugates due to low Φ_Δ of **2**-AMNPs, **3**-AMNPs compared to **2** and **3**. A low PDT activity of conjugates **4**-cys-AgNPs, **4**-AMNPs, **6**-AMNPs and **7**-AMNPs with higher Φ_Δ compared to their MPcs alone was also observed, possibly due to aggregation of MPcs on the nanoparticle [133,144]. In addition, the slow *in vitro* dissolution of nanoparticles in physiological media is known to affect their bioavailability [154,155]. The same decrease of PDT activity was observed for **2**-FA and **3**-FA conjugates. MPc-FA conjugates recorded better PDT activity compared to MPc-AMNPs conjugates due to their higher Φ_Δ. Folic acid-folate targeting, and water solubility of MPc-FA conjugates improved their bioavailability, hence improving PDT activity on MCF-7 cells over AMNPs carriers. MCF-7 cell viabilities of less than 50% were recorded at 80 µg/mL of all MPcs and conjugates administered under laser irradiation making them better agents as photosensitizers in cancer therapy.

CHAPTER 6

PHOTODYNAMIC ANTIMICROBIAL CHEMOTHERAPY

This chapter outlines the *in vitro* dark cytotoxicity and photodynamic antimicrobial chemotherapy (PACT) activity of MPcs alone and when conjugated to silver nanoparticles on Gram (+) *S. aureus.* Cinnamic acid MPcs **3** - **6** with their MPc-AgNPs conjugates (Scheme 3.10) were tested for both dark cytotoxicity and PACT activity on *S. aureus*.

6.1 PACT STUDIES ON *S. AUREUS*.

6.1.1 Control and optimization studies.

All complexes were dissolved in 2% of DMSO in PBS (pH 7.4) which was also used for control studies. 2% DMSO/PBS did not show any antimicrobial effect on *S. aureus* when studied at 30 min irradiation under light or when placed in the dark for 30 min, Fig 6.1. Optimization studies were performed on *S. aureus* using complex **5** (as an example), Fig 6.1. The optimum concentration (amount that has the highest cytotoxicity, resulting in the lowest viable bacterial colonies (<50%)) was found to be 5 mg/L as tested with complex **5** (as an example), Fig 6.1. At higher concentrations, the antimicrobial activity of MPcs and conjugates decreases, which could be due to aggregation of the complexes at these concentrations.

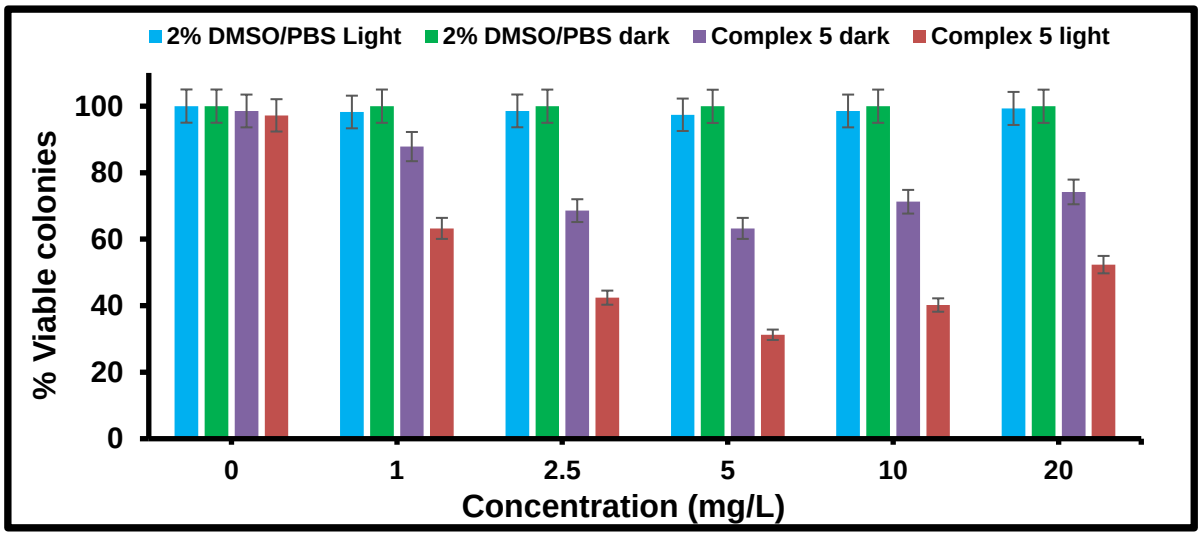

Fig 6.1. Effect of 2% DMSO/ PBS (pH 7.4) and MPcs and conjugates concentration (using **5** as an example) on *S. aureus* after 30 min of light irradiation.

6.1.2 *In vitro* dark cytotoxicity and PACT studies.

MPcs alone and their conjugates recorded minimal antimicrobial activity (< 15% killing) in the dark at times 90 min and 120 min, Fig 6.2 (using **5** and **5**-cys-AgNPs for illustrative purposes). The same trend was observed for all other MPcs (**3**, **4** and **6**) with their conjugates. The observed dark cytotoxicity (< 15% killing) could be due to the antimicrobial properties of cinnamic acid derivatives and silver nanoparticles [60,158]. The antimicrobial activity of MPcs alone and conjugates increased when incubated in the presence of light compared to that in the dark Fig 6.2, showing high potency against *S. aureus* in light treatment than in the dark. The difference in the dark cytotoxicity and PACT activity of MPcs and conjugates can also be observed on agar micrographs, Fig 6.3B and C using **5**-cys-AgNPs as an example. There was an almost complete inactivation of *S. aureus* colonies on agar micrographs after PACT treatment (Fig 6.3C) compared to partially full agar micrographs of viable *S. aureus* colonies after dark cytotoxicity studies (Fig 6.3B).

Log reductions and percentage reduction were used to quantify viable microorganisms after PACT. Percentage reductions is a ratio of the number of viable colonies after treatment with the photosensitizer to viable colonies of the control studies (without the photosensitizer) under the same treatment conditions. Log reduction determines the reduction of viable microorganisms using a logarithmic scale. Equation 6.1 [74] was used to calculate viable microorganisms and the results are summarizes in Table 6.1.

$$\text{Log reduction} = \text{Log}_{10}(A) - \text{Log}_{10}(B) \quad \text{6.1}$$

where A and B are the number of viable micro-organism, before and after treatment, respectively. Photocytotoxicity (PACT) activity of conjugates resulted in higher log reduction and percentage reductions as compared to MPcs alone, Table 6.1. The higher photocytotoxicity is related to the higher Φ_Δ of conjugates compared to that of MPcs alone, Table 6.1. Cys-AgNPs alone had log reduction of 4.49 with percentage reduction of 45.21, which shows relatively low antimicrobial potency on the *S. aureus* under light. This provides evidence that the PACT activity of conjugates was influenced more by the MPc structure and its singlet oxygen generating abilities than the cys-AgNPs, the later improves singlet oxygen quantum yields.

Complex **6** and **6**-cys-AgNPs recorded the lowest log reductions of 2.97 and 5.68, respectively compared to other MPcs and conjugates, Table 6.1, corresponding to the low singlet oxygen quantum yields in **6** and **6**-cys-AgNPs. The log reduction of 2.97 obtained for complex **6** is comparable to the recently reported 2.61 for a cationic silicon phthalocyanine [159]. MPcs **3** - **5** and their conjugates have asymmetric structures with higher Φ_Δ compared to **6** and **6**-cys-AgNPs, Table 6.1. In addition to higher Φ_Δ, asymmetry in complexes such as MPcs is known to improve photosensitizing properties, hence the higher log reduction for **3** - **5** and conjugates compared to **6** and **6**-cys-AgNPs. **5** and **5**-cys-AgNPs had the highest log reductions of all MPcs and conjugates due to high singlet oxygen quantum yields, Table 6.1.

Comparing the PDT and PACT activities of **4** and **4**-cys-AgNPs, shows that there was low cytotoxicity in the dark of **4** and **4**-cys-AgNPs when tested on MCF-7 cells and on *S. aureus*. **4** and **4**-cys-AgNPs also had higher phototoxicity that resulted in high PDT activity (low cell viability) and high log reductions as a result of *S. aureus* photoinactivation, Table 5.1 and 6.1.

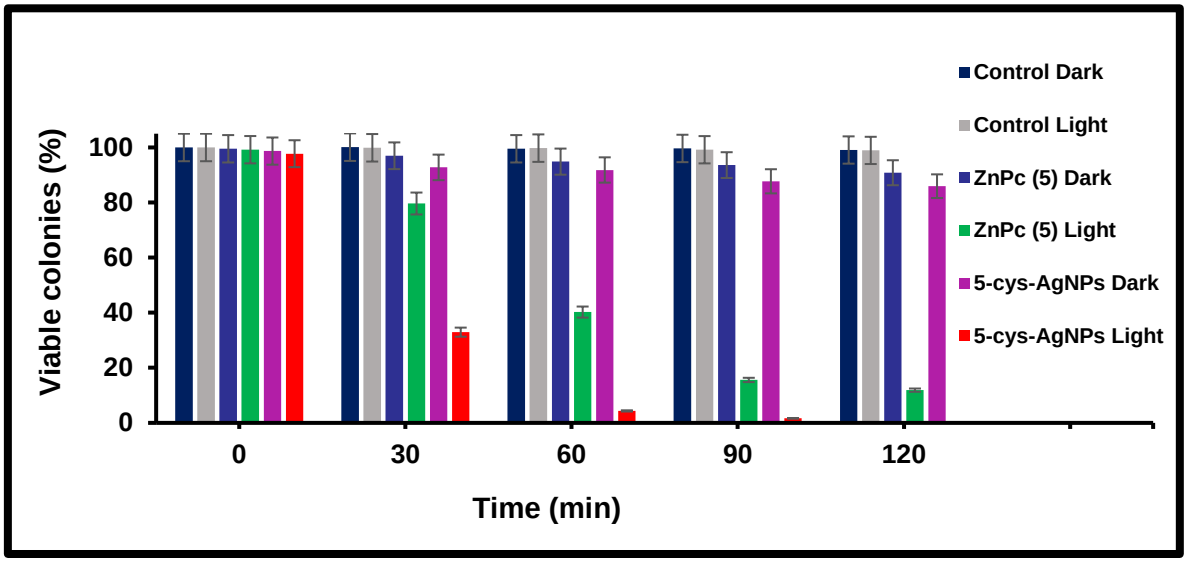

Fig 6.2. Dark cytotoxicity and PACT activity of 5 mg/L of **5** and **5**-cys-AgNPs (as an example) on *S. aureus*. Control studies were done with 2% DMSO in PBS (pH 7.4).

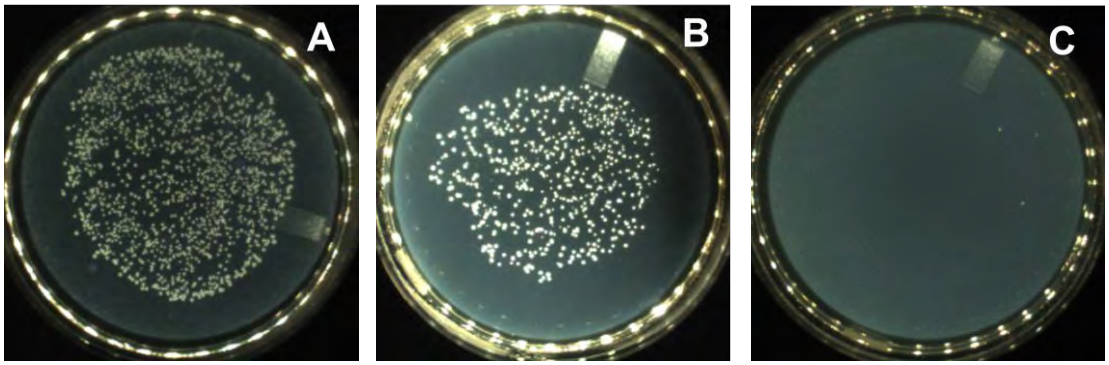

Fig 6.3. Agar plates micrographs depicting the *S. aureus* colonies after 120 min of treatment with A) 2% DMSO in PBS as control, B) 5 mg/L of **5**-cys-AgNPs in the dark and C) 5 mg/L of **5**-cys-AgNPs (as an example) in the light (PACT).

Table 6.1. Log reduction values for the photoinactivation of *S. aureus* with 5 mg/L of photosensitizers dissolved in 2% DMSO of PBS. Irradiation time of 120 min.

Complex	Percentage reduction	Log reduction	Φ_Δ
Cys-AgNPs	45.21	4.49	-
3	85.89	3.42	0.48
3-cys-AgNPs	99.72	6.71	0.59
4	96.98	5.82	0.56
4-cys-AgNPs	99.84	7.71	0.63
5	94.56	6.12	0.59
5-cys-AgNPs	99.95	8.06	0.67
6	84.52	2.97	0.26
6-cys-AgNPs	95.83	5.68	0.45

6.1.3 MPcs photostability studies.

Irradiation times used during PACT studies were longer (30 min to 120 min) in order to allow the reactive oxygen species (ROS) to oxidize the cell membranes and the internal DNA structures to result in effective destruction of the cytoplasm, thus the inactivation of the bacteria [160]. The MPcs and conjugates used in this work were hence tested for their stability under longer (0 to 180 min) UV irradiations (light source wavelength of 680 nm) while monitoring the spectral changes of the Q-band over 60 min intervals, Fig 6.4. There was no degradation of the complexes or the conjugates that were observed at 0-180 min UV irradiation of the photosensitizers [161], indicating the stability of the complexes at longer irradiation times of PACT. There were insignificant spectral changes on the Q-band of complex **5** and **5**-cys-AgNPs (as representatives of the photosensitizers) after irradiation with light, Fig 6.4A and B, respectively.

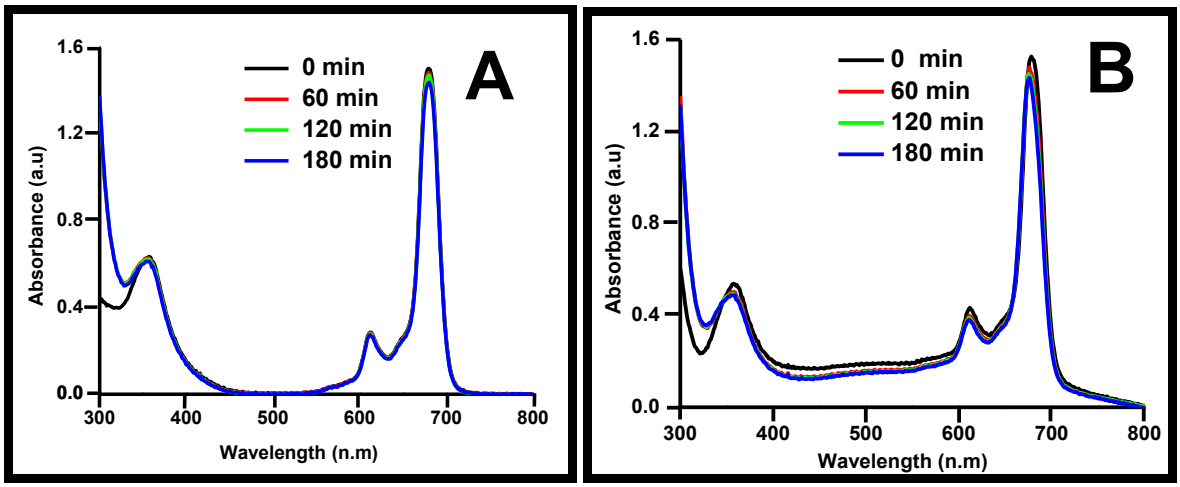

Fig 6.4. Spectral changes in the Q-band of the UV irradiated A) **5** and B) **5**-cys-AgNPs in DMSO monitored at 60 min irradiation with initial absorbance at ~1.5. Light source UV wavelength of 680 nm.

6.2 SUMMARY.

The dark cytotoxicity and PACT activity of cinnamic acid ZnPcs alone and when conjugated to cys-AgNPs were successfully tested on Gram (+) *S. aureus* microorganisms. There was very low dark cytotoxicity of MPcs (**3** - **6**) and MPc-AgNPs (**3**-cys-AgNPs, **4**-cys-AgNPs, **5**-cys-AgNPs and **6**-cys-AgNPs) compared to their PACT activity on *S. aureus*. Asymmetric MPcs (**3** - **5**) and their conjugates recorded better PACT activity compared to symmetrical MPc **6** and its conjugate. MPc-AgNPs recorded higher log reductions and reduction percentages of *S. aureus* compared to MPcs alone, due to their higher singlet oxygen quantum yield.

CHAPTER 7

CONCLUSION AND RECOMMENDATIONS

This chapter outlines the findings of the studies completed and reported in this thesis. It also makes recommendations for future studies.

7.1 CONCLUSIONS.

This study reported on the successful synthesis of novel asymmetric and symmetrical carboxylic acid functionalized phthalocyanine complexes metallated with zinc and indium in their inner cavity. The electronic absorption spectra of MPcs and conjugates showed the appearance of a monomeric Q-band (ca. 670 nm) and a B-band (ca. 350 nm) in DMSO, such bands are typical of MPcs in DMSO. The structure of MPcs was confirmed by FTIR, NMR, MALDI-TOF mass spectrometry and elemental analysis. MPcs were further covalently linked to amino functionalized magnetic nanoparticles (AMNPs), L-cysteine capped silver nanoparticles (cys-AgNPs) and folic acid (FA) through an amide bond between the carboxylic acid of MPcs and the NH_2 of AMNPs, or cys-AgNPs or FA. This was for the first time that MPcs were linked to FA through the NH_2 group of FA instead of carboxyl groups. MPcs were also linked to AgNPs through a cysteine linker for the first time in this work.

The covalent linkage of FA to MPcs improved the water solubility of MPcs (**1 - 3**) and improved the photosensitizing properties of MPcs in water compared to the non-water soluble physically mixed MPcs and FA conjugates. Asymmetric MPcs (**1**-**5**) and their conjugates recorded improved photophysical and photochemical properties compared to the symmetrical MPcs (**6** and **7**) and their conjugates, respectively. Tetra substituted InPc (**7**) and its conjugate recorded higher triplet and singlet oxygen quantum yields compared to tetra substituted ZnPc (**6**), due to heavy atom effect of indium compared to zinc. The heavy atom effect of AMNPs and AgNPs also improved the triplet and singlet oxygen quantum yields of MPcs **4**, **6**

and **7** when linked to AMNPs and MPcs **3** - **6** when linked to AgNPs. MPcs **1** - **3** recorded peculiar triplet and singlet oxygen quantum yields when linked to AMNPs and FA. This was thought to be due to aggregation of MPc monomers, possible non-radiative processes, or poor interaction of molecular oxygen with excited triplet state.

MPcs and conjugates (MPc-FA, MPc-AgNPs and MPc-AMNPs) recorded lower dark cytotoxicity effect and higher PDT activity on MCF-7 breast cancer cells at different concentrations. At 80 µg/mL, the lower singlet oxygen quantum yield of **2**-AMNPs and **3**-AMNPs resulted in a lower PDT activity compared to **2** and **3**, respectively. There was also a decrease in PDT activity of **4**-cys-AgNPs, **4**-AMNPs, **6**-AMNPs, **7**-AMNPs, **2**-FA and **3**-FA compared to their MPcs. The decrease in PDT activity of conjugates compared to MPcs alone could be due to aggregation of MPcs through π-π stacking of the planar rings which decreases the photoactivity of MPcs [133,144]. In addition, the slow *in vitro* dissolution rate of nanoparticles in physiological media is also known to affect their bioavailability [154,155].

MPc-FA conjugates recorded better PDT activity when compared to MPc-AMNPs conjugates due to their higher Φ_{Δ}. Additionally, folic acid-folate targeting, and water solubility of MPc-FA improved their bioavailability, hence improving the PDT activity on MCF-7 cells over AMNPs carriers. All MPcs and conjugates recorded MCF-7 cell viabilities of less than 50% at 80 µg/mL concentration under light irradiation (PDT), hence proving that the complexes under study are more potent as photosensitizers in cancer therapy than as chemotherapeutic agents.

The *in vitro* dark cytotoxicity and PACT activity of cinnamic acid ZnPcs and their AgNPs showed low cytotoxicity of MPcs (**3** - **6**) and MPc-AgNPs (**3**-cys-AgNPs, **4**-cys-AgNPs, **5**-cys-AgNPs and **6**-cys-AgNPs) in the dark compared to their PACT activity on *S. aureus*. Asymmetric MPcs (**3** - **5**) and their conjugates recorded better PACT activity compared to symmetrical MPc **6** and its conjugate. MPc-AgNPs recorded higher log reductions and reduction percentages of *S. aureus* compared to MPcs alone, due to their higher singlet oxygen quantum yield. This study has demonstrated for the first time that MPcs and their conjugates can be applied to both PDT and PACT.

7.2 RECOMMENDATIONS.

To synthesize water soluble asymmetric MPcs for improved singlet oxygen quantum yields in water and to achieve better cellular uptake by cancer cells (PDT) or microorganisms (PACT).

Detailed *in vitro* and *in vivo* studies of MPcs and conjugates on different cancer cell lines and microorganism (Gram (+) and Gram (-)) with fluorescence imaging to monitor cellular uptake will be required to advance the research on PDT and PACT.

Different cancer specific molecules linked to asymmetric MPcs will be required to improve delivery of PS agents on cancer site. Further studies need to be conducted on different nanoparticles when linked to MPcs for improved drug delivery and solubility *in vitro* and *in vivo*.

REFERENCES

This section gives reference of all the articles and book chapters that were used during this study. The references below are for all the chapters of this thesis.

1. K. C. Hwang, *J Chem Soc, Chem Commun*, 1995, **4**, 173–174.

2. D. B. Mawhinney, V. Naumenko, A. Kuznetsova, J. T. Yates, J. Liu and R. E. Smalley, *J Amer Chem Soc*, 2000, **122**, 2383–2384.

3. S. Banerjee, T. Hemraj-Benny and S. S. Wong, *Adv Mat*, 2005, **17**, 17–29.

4. I. Muzikante, V. Parra, R. Dobulans, E. Fonavs, J. Latvels and M. Bouvet, *Sensors*, 2007, **7**, 2984–2996.

5. M. Hanack, T. Schneider, M. Barthel, J. S. Shirk, S. R. Flom and R. G. S. Pong, *Coord Chem Rev*, 2001, **219**–**221**, 235–258.

6. T. Rawling and A. McDonagh, *Coord Chem Rev*, 2007, **251**, 1128–1157.

7. M. Camerin, M. Magaraggia, M. Soncin, G. Jori, M. Moreno, I. Chambrier, M. J. Cook and D. A. Russell, *Eur J Canc*, 2010, **46**, 1910–1918.

8. M. Wainwright, *J Antimicrob Chemother*, 1998, **42**, 13–28.

9. L. Edwards and M. Gouterman, *J Mol Spectros*, 1970, **33**, 292–310.

10. A. Henriksson and M. Sundbom, *Theor Chim Acta*, 1972, **27**, 213–222.

11. M. J. Stillman and T. Nyokong, in *Phthalocyanines-Properties and Applications*, eds. C. C. Leznoff and B. Lever, VCH Publications, New York, 1989, pp. 133–290.

12. M. Gouterman, in *The Porphyrins-Physical Chemistry, Part A.*, ed. D. Dolphin, Academic Press, New York, 1978, pp. 1–165.

13. J. M. Kroon, R. B. M. Koehorst, M. Van Dijk, G. M. Sanders and E. J. R. Sudhölter, *J Mat Chem*, 1997, **7**, 615–624.

14. A. Eisfeld and J. S. Briggs, *Chem Phys*, 2006, **324**, 376–384.

15. M. S. Rodrigues-morgade, G. de la Torre and T. Torres, in *The Porphyrin Handbook*, eds. K. M. Kadish, K. M. Smith and R. Guilard, Academic Press, New York, 2003, pp. 125–160.

16. A. Louati, M. E. El Meray, M. Gross, A. Giraudeau, J. J. Andre, J. Simon and K. M. Kadish, *Inorg Chem*, 1985, **24**, 1175–1179.

17. P. Erk and H. Hengelsberg, in *The Porphyrin Handbook : Applications of Phthalocyanines*, eds. K. M. Kadish, T. A. Smith and R. Guilard, Academic Press, New York, 2003, vol. 15, pp. 105–149.

18. K. M. Kadish, K. M. Smith and R. Guilard, Eds., *The Porphyrin Handbook : Phthalocyanines synthesis*, Academic Press, New York, 2003, vol. 15.

19. P. Gregory, *J Porphyr Phthalocyanine*, 1999, **3**, 468–476.

20. T. Keller, T. R. Price and J. R. Griffith, *Synthesis*, 1980, **8**, 613–620.

21. P. García Calavia, I. Chambrier, M. J. Cook, A. H. Haines, R. A. Field and D. A. Russell, *J Coll Int Sc*, 2018, **512**, 249–259.

22. A. Wang, L. Long and C. Zhang, *Tetrahedron*, 2012, **68**, 2433–2451.

23. W. A. Nevin, W. Liu, S. Greenberg, M. R. Hempstead, S. M. Marcuccio, M. Melník, C. C. Leznoff and A. B. P. Lever, *Inorg Chem*, 1987, **26**, 891–899.

24. J. M. Ward, M. E. Grabin, E. Berlin and D. M. Young, *Canc Res*, 1977, **37**, 1238–1240.

25. M. F. Pera, B. C. Zook and H. C. Harder, *Canc Res*, 1979, **39**, 1279–1286.

26. E. A. Lukyanets, *J Porphyr Phthalocyanine*, 1999, **3**, 424–432.

27. C. Anderson, K. Freye, K. A. Tubesing, Y. S. Li, M. Kenney, H. Mukhtar and C. Elmets, *Photochem Photobiol*, 1998, **67**, 332–336.

28. R. Bonnett, in *Chemical Aspects of Photodynamic therapy*, Gordon and Breach Science Publishers, Amsterdam, 2000, p. 231.

29. N. L. Oleinick, A. R. Antunez, M. E. Clay, B. D. Rihter and M. E. Kenney, *Photochem Photobiol*, 1993, **57**, 242–247.

30. L. B. Josefsen and R. W. Boyle, *Theranostics*, 2012, **2**, 916–966.

31. P. Agostinis, K. Berg, K. Cengel, T. Foster, A. Girotti, S. Gollnick, S. Hahn, M. Hamblin, A. Juzeniene, D. Kessel, M. Koberlik, J. Moan, P. Mroz, D. Nowis, J. Piette, B. Wilson and J. Golab, *CA Canc J Clin*, 2011, **61**, 250–281.

32. L. Dai, J. Liu, Z. Luo, M. Li and K. Cai, *J Mat Chem B*, 2016, **4**, 6758–6772.

33. A. Stallivieri, L. Colombeau, G. Jetpisbayeva, A. Moussaron, B. Myrzakhmetov, P. Arnoux, S. Acherar, R. Vanderesse and C. Frochot, *Bioorg Med Chem*, 2017, **25**, 1–10.

34. A. Wicki, D. Witzigmann, V. Balasubramanian and J. Huwyler, *J Contr Rel*, 2015, **200**, 138–157.

35. P. S. Low, W. Henne and D. Doorneweerd, *Acc Chem Res*, 2008, **41**, 120–129.

36. A. Stallivieri, F. Baros, G. Jetpisbayeva and B. Myrzakhmetov, *Curr Med Chem*, 2015, **22**, 3185–3207.

37. Y. Lu and P. S. Low, *Adv Drug Del Rev*, 2002, **64**, 342–352.

38. K. Jeong, C. S. Kang, Y. Kim, Y.D. Lee, I. C. Kwon and S. Kim, *Canc Lett*,

2016, **374**, 31–43.

39. F. Moret and E. Reddi, *J Porphyr Phthalocyanine*, 2017, **21**, 239–256.

40. H.C. Huang, S. Barua, G. Sharma, S. K. Dey and K. Rege, *J Contr Rel*, 2011, **155**, 344–357.

41. T. Nyokong and E. Antunes, *Coord Chem Rev*, 2013, **257**, 2401–2418.

42. N. Bertrand, J. Wu, X. Xu, N. Kamaly and O. C. Farokhzad, *Adv Drug Del Rev*, 2014, **66**, 2–25.

43. D. Bechet, P. Couleaud, C. Frochot, M. L. Viriot, F. Guillemin and M. Barberi-Heyob, *Trend Biotech*, 2008, **26**, 612–621.

44. L. Zhou, E. Chen, W. Jin, Y. Wang, J. Zhou and S. Wei, *Dalton Trans*, 2016, **45**, 15170–15179.

45. B. M. Motloung, K. E. Sekhosana, M. Managa, E. Prinsloo and T. Nyokong, *Polyhedron*, 2019, **174**, 114157-114165.

46. D. A. Fadeel, G. M. Al-Toukhy, A. M. Elsharif, S. S. Al-Jameel, H. H. Mohamed and T. E. Youssef, *Photodiag Photodyn Ther*, 2018, **23**, 25–31.

47. L. B. De Paula, F. L. Primo, M. R. Pinto, P. C. Morais and A. C. Tedesco, *RSC Adv*, 2017, **7**, 9115–9122.

48. K. Li, W. Dong, Q. Liu, G. Lv, M. Xie, X. Sun, L. Qiu and J. Lin, *J Photochem*

Photobiol B: Biol, 2019, **190**, 1–7.

49. R. O. Ogbodu, E. Antunes and T. Nyokong, *Polyhedron*, 2013, **60**, 59–67.

50. R. O. Ogbodu, I. Ndhundhuma, A. Karsten and T. Nyokong, *Spectrochim Acta - Part A: Molec Biomol Spectros*, 2015, **137**, 1120–1125.

51. D. O. Oluwole, E. Prinsloo and T. Nyokong, *Polyhedron*, 2016, **119**, 434–444.

52. B. S. Wang, J. Wang and J.Y. Chen, *J Mater Chem B*, 2014, **2**, 1594-1605.

53. N. Nombona, K. Maduray, E. Antunes, A. Karsten and T. Nyokong, *J Photochem Photobiol B: Biol*, 2012, **107**, 35–44.

54. L. C. Nene, M. Managa and T. Nyokong, *Dye Pigment*, 2019, **165**, 488–498.

55. A. R. Vortherms, R. P. Doyle, D. Gao, O. Debrah and P. J. Sinko, *Nucleoside, Nucleotide Nucleic Acid*, 2008, **27**, 173–185.

56. P. Huang, Z. Li, J. Lin, D. Yang, G. Gao, C. Xu, L. Bao, C. Zhang, K. Wang, H. Song, H. Hu and D. Cui, *Biomaterials*, 2011, **32**, 3447–3458.

57. N. Rapulenyane, E. Antunes and T. Nyokong, *New J Chem*, 2013, **37**, 1216–1223.

58. J. D. Guzman, *Molecules*, 2014, **19**, 19292–19349.

59. H. ML, D. Kromhout, C. Aravanis and E. Al, *Arch Int Med*, 1995, **155**, 381–

386.

60. A. A. Esenpinar, A. R. Özkaya and M. Bulut, *Polyhedron*, 2009, **28**, 33–42.

61. J. Chen, Z. Chen, Y. Zheng, S. Zhou, J. Wang, N. Chen, J. Huang, F. Yan and M. Huang, *J Porphyr Phthalocyanine*, 2011, **15**, 293–299.

62. J. E. Schneider, J. R. Phillips, Q. Pye, M. L. Maidt, S. Price and R. A. Floyd, *Arch Biochem Biophys*, 1993, **301**, 91–97.

63. S. B. Brown, E. A. Brown and I. Walker, *Lancet: Oncol*, 2004, **5**, 497–508.

64. F. Sperandio, Y.Y. Huang and M. Hamblin, *Rec Pat Anti-Inf Drug Disc*, 2013, **8**, 108–120.

65. L. Bourré, F. Giuntini, I. M. Eggleston, C. A. Mosse, A. J. MacRobert and M. Wilson, *Photochem Photobiol Sc*, 2010, **9**, 1613–1620.

66. F. Vatansever, W. C. M. A. de Melo, P. Avci, D. Vecchio, M. Sadasivam, A. Gupta, R. Chandran, M. Karimi, N. A. Parizotto, R. Yin, G. P. Tegos and M. R. Hamblin, *FEM Microbiol Rev*, 2013, **37**, 955–989.

67. R. H. Thompson, *Lancet*, 2006, **368**, 824–826.

68. N. Ahmed, H. Fessi and A. Elaissari, *Drug Disc Today*, 2012, **17**, 928–934.

69. T. Mthethwa and T. Nyokong, *Photochem Photobiol Sc*, 2015, **14**, 1346–1356.

70. S. Perni, P. Prokopovich, J. Pratten, I. P. Parkin and M. Wilson, *Photochem Photobiol Sc*, 2011, **10**, 712–720.

71. N. Kashef, Y. Y. Huang and M. R. Hamblin, *Nanophotonics*, 2017, **6**, 853–879.

72. A. Tunçel, S. Öztörk, M. Ince, K. Ocakoglu, M. Hoşgör-Limoncu and F. Yurt, *J Porphyr Phthalocyanine*, 2019, **23**, 206–212.

73. O. L. Osifeko, I. Uddin, P. N. Mashazi and T. Nyokong, *New J Chem*, 2016, **40**, 2710–2721.

74. M. A. Idowu, S. Xego, Y. Arslanoglu, J. Mark, E. Antunes and T. Nyokong, *Spectrochim Acta - Part A: Molec Biomol Spectros*, 2018, **193**, 407–414.

75. N. Nombona, E. Antunes, W. Chidawanyika, P. Kleyi, Z. Tshentu and T. Nyokong, *J Photochem Photobiol A: Chem*, 2012, **233**, 24–33.

76. K. Niska, N. Knap, A. Kędzia, M. Jaskiewicz, W. Kamysz and I. Inkielewicz-Stepniak, *Int J Med Sc*, 2016, **13**, 772–782.

77. R. Yin, T. Agrawal, U. Khan, G. k Gupta, V. Rai, Y.Y. Huang and M. R. Hamblin, *Nanomedicine*, 2015, **10**, 2379–2404.

78. Z. Biyiklioglu, I. Ozturk, T. Arslan, A. Tunçel, K. Ocakoglu, M. Hosgor-Limoncu and F. Yurt, *Dye Pigment*, 2019, **166**, 149–158.

79. N. Masilela and T. Nyokong, *J Photochem Photobiol A: Chem*, 2013, **255**, 1–9.

80. E. Anaya-Plaza, E. van de Winckel, J. Mikkilä, J. M. Malho, O. Ikkala, O. Gulías, R. Bresolí-Obach, M. Agut, S. Nonell, T. Torres, M. A. Kostiainen and A. de la Escosura, *Chem - A Eur J*, 2017, **23**, 4320–4326.

81. W. Tong, Y. Xiong, S. Duan, X. Ding and F. J. Xu, *Biomat Sc*, 2019, **7**, 1905–1918.

82. A. Sindelo and T. Nyokong, *Heliyon*, 2019, **5**, 2352-2360.

83. D. O. Oluwole and T. Nyokong, *Polyhedron*, 2015, **87**, 8–16.

84. A. J. Cole, V. C. Yang and A. E. David, *Trend Biotechnol*, 2011, **29**, 323–332.

85. A. L. Andrade, D. M. Souza, M. C. Pereira, J. D. Fabris, R. Z. Domingues, U. Federal, D. M. Gerais and B. Horizonte, *Ceramica*, 2009, **55**, 420–424.

86. A. B. Chin and I. I. Yaacob, *J Mat Proces Technol*, 2007, **191**, 235–237.

87. M. C. Mascolo, Y. Pei and T. A. Ring, *Material*, 2013, **6**, 5549–5567.

88. M. Kimata, D. Nakagawa and M. Hasegawa, *Powder Technol*, 2003, **132**, 112–118.

89. H. C. Roth, S. P. Schwaminger, M. Schindler, F. E. Wagner and S. Berensmeier, *J Magnet Mag Mat*, 2015, **377**, 81–89.

90. X. Chao, Z. Zhang, L. Guo, J. Zhu, M. Peng, A. J. M. Vermorken, W. J. M. van de Ven, C. Chen and Y. Cui, *Plos One*, 2012, **7**, 40388–40394.

91. A. C. Burdușel, O. Gherasim, A. M. Grumezescu, L. Mogoantă, A. Ficai and E. Andronescu, *Nanomaterials*, 2018, **8**, 1–25.

92. S. Mura and P. Couvreur, *Adv Drug Del Rev*, 2012, **64**, 1394–1416.

93. G. A. Sotiriou, A. Meyer, J. T. N. Knijnenburg, S. Panke and S. E. Pratsinis, *Langmuir*, 2012, **28**, 15929–15936.

94. S. M. Hussain, K. L. Hess, J. M. Gearhart, K. T. Geiss and J. J. Schlager, *Toxicol in Vitro*, 2005, **19**, 975–983.

95. P. M. Holmblad, J. H. Larsen and I. Chorkendorff, *J Amer Chem Soc*, 2010, **104**, 7289–7295.

96. D. R. Arnold, N. C. Baird, J. R. Bolton, J. C. D. Brand, P. W. M. Jacobs, P. de Mayo, in *Photochemistry - an Introduction*, ed. H. Timpe, Academic Press, Inc, New york, 1974, vol. 318, pp. 878–878.

97. S. Fery-forgues and D. Lavabre, *J Chem Educ*, 1999, **76**, 1260–1264.

98. A. Ogunsipe, J. Chen and T. Nyokong, *New J Chem*, 2004, **28**, 822–827.

99. A. Magadla, D. O. Oluwole, J. Britton and T. Nyokong, *Inorg Chim Acta*, 2018, **482**, 438–446.

100. T. Tran-Thi, C. Desforge and C. Thiec, *J Phys Chem*, 1989, **93**, 1226–1233.

101. P. Kubát and J. Mosinger, *J Photochem Photobiol A: Chem*, 1996, **96**, 93–97.

102. H. Li and T. F. Guarr, *J Chem Soc, Chem Commun*, 1989, **13**, 832–834.

103. N. A. Kuznetsova, N. S. Gretsova, O. A. Yuzhakova, V. M. Negrimovskii, O. L. Kaliya and E. A. Lukyanets, *Russ J Gen Chem*, 2001, **71**, 36–41.

104. T. Nyokong and E. Antunes, in *The handbook of Pophyrin Science*, eds. K. Kadish, K. Smith and R. Guilard, Academic Press, New York, vol. 7, p. 2010.

105. F. Wilkinson, P. W. Helman and A. B. Ross, *J Phys Chem Ref Data*, 1993, **22**, 113–262.

106. A. Yahyazadeh and V. Azimi, *Chemi Solid Mat*, 2012, **49**, 33–40.

107. P. Tau and T. Nyokong, *Polyhedron*, 2006, **25**, 1802–1810.

108. M. Ambroz, A. Beeby, A. Macrobert, M. Simpson, R. Svensen and D. Phillips, *J Photochem Photobiol B: Biol*, 1991, **9**, 87–95.

109. L. Shen, Y. Qiao, Y. Guo, S. Meng, G. Yang, M. Wu and J. Zhao, *Cer Int*, 2014, **40**, 1519–1524.

110. P. Modisha, T. Nyokong and E. Antunes, *J Mol Cat A: Chem*, 2013, **380**, 131–138.

111. D. O. Oluwole, C. M. Tilbury, E. Prinsloo, J. Limson and T. Nyokong, *Polyhedron*, 2016, **106**, 92–100.

112. O. L. Osifeko, M. Durmuş and T. Nyokong, *J Photochem Photobiol A: Chem*, 2015, **301**, 47–54.

113. V. Kussovski, V. Mantareva, I. Angelov, P. Orozova, D. Wöhrle, G. Schnurpfeil, E. Borisova and L. Avramov, *FEM Microbiol Lett*, 2009, **294**, 133–140.

114. V. Mantareva, V. Kussovski, I. Angelov, E. Borisova, L. Avramov, G. Schnurpfeil and D. Wöhrle, *Bioorg Med Chem*, 2007, **15**, 4829–4835.

115. J. Rusanova, M. Pilkington and S. Decurtins, *Chem Commun*, 2002, **1**, 2236–2237.

116. N. Kobayashi, T. Furuyama and K. Satoh, *J Amer Chem Soc*, 2011, **133**, 19642–19645.

117. Y. Zorlu, U. Kumru, Ü. Işci, B. Divrik, E. Jeanneau, F. Albrieux, Y. Dede, V. Ahsen and F. Dumoulin, *Chem Commun*, 2015, **51**, 6580–6583.

118. N. Kobayashi, N. Sasaki, Y. Higashi and T. Osa, *Inorg Chem*, 1995, **34**, 1636–1637.

119. H. Shinohara, O. Tsaryova, G. Schnurpfeil and D. Wöhrle, *J Photochem Photobiol A: Chem*, 2006, **184**, 50–57.

120. W. Song, C. He, Y. Dong, W. Zhang, Y. Gao, Y. Wu and Z. Chen, *Phys Chem Chem Phys*, 2015, **17**, 7149–7157.

121. L. Li, J.F. Zhao, N. Won, H. Jin, S. Kim and J.Y. Chen, *Nanosc Res Lett*, 2012, **7**, 386–393.

122. K. M. Rosenblatt and H. Bunjes, *Eur J Pharmac Biopharm*, 2017, **117**, 49–59.

123. M. Abbas, B. Parvatheeswara Rao, S. M. Naga, M. Takahashi and C. Kim, *Cer Int*, 2013, **39**, 7605–7611.

124. A. W. Snow, J. R. Griffith and N. P. Marullo, *Macromolecules*, 1984, **17**, 1614–1624.

125. R. Jenkins and R. Synder, in *Introduction to X-ray Diffractometry*, Wiley and Sons, New York, 1998.

126. M. Danaei, M. Dehghankhold, S. Ataei, F. Hasanzadeh Davarani, R. Javanmard, A. Dokhani, S. Khorasani and M. R. Mozafari, *Pharmaceutics*, 2018, **10**, 1–17.

127. M. C. Hoo, N. Starostin, P. West and M. L. Mecartney, *J Nanopart Res*, 2008, **10**, 89–96.

128. K. G. Thomas and P. V Kamat, *Acc Chem Res*, 2003, **36**, 888–898.

129. B. L. Darby, B. Auguié, M. Meyer, A. E. Pantoja and E. C. Le Ru, *Nat Phot*,

2016, **10**, 40–45.

130. A. A. Lanje, S. J. Sharma and B. P. Ramchandra, *J Chem Pharm Res*, 2011, **3**, 478–483.

131. F. Dumoulin, M. Durmu, V. Ahsen and T. Nyokong, *Coord Chem Rev*, 2010, **254**, 2792–2847.

132. H. Isago and H. Fujita, *J Porphyr Phthalocyanine*, 2018, **22**, 102–111.

133. A. Ogunsipe, J. Chen and T. Nyokong, *New J Chem*, 2004, **28**, 822–827.

134. A. Ogunsipe, D. Maree and T. Nyokong, *J Mol Struct*, 2003, **650**, 131–140.

135. J. R. Darwent, P. Douglas, A. Harriman, G. Porter and M. C. Richoux, *Coord Chem Rev*, 1982, **44**, 83–126.

136. J. R. Lakowicz, J. Malicka, I. Gryczynski, Z. Gryczynski and C. D. Geddes, *J Phys D: Appl Phys*, 2003, **36**, 240–249.

137. J. J. Apperloo, C. Martineau, P. Van Hal, J. Roncali and R. J. Janssen, *J Phys Chem A*, 2002, **106**, 21–31.

138. P. Khoza, E. Antunes, J. Y. Chen and T. Nyokong, *J Lum*, 2013, **134**, 784–790.

139. N. Nombona, W. Chidawanyika and T. Nyokong, *Polyhedron*, 2011, **30**, 654–659.

140. G. Li, D. Magana and R. B. Dyer, *J Phys Chem B*, 2012, **116**, 3467–3475.

141. A. Dudkowiak, E. Teślak and J. Habdas, *J Mol Struct*, 2006, **792**–**793**, 93–98.

142. N. Nombona and T. Nyokong, *Inorgan Chim Acta*, 2012, **392**, 380–387.

143. K. Virkki, H. Hakola, M. Urbani, L. Tejerina, M. Ince, M. V. Martínez-Díaz, T. Torres, V. Golovanova, V. Golovanov and N. V. Tkachenko, *J Phys Chem C*, 2017, **121**, 9594–9605.

144. S. Mathai, T. A. Smith and K. P. Ghiggino, *Photochem Photobiol Sc*, 2007, **6**, 995-1005.

145. H. Gu, K. Xu, Z. Yang, C. K. Chang and B. Xu, *Chem Communi*, 2005, 4270–4282.

146. O. L. Osifeko, I. Uddin, P. N. Mashazi and T. Nyokong, *New J. Chem*, 2016, **40**, 2710–2721.

147. J. C. Koziar and D. Cowan, *Acc Chem Res*, 1978, **11**, 334–341.

148. A. Drzewiecka-Matuszek, A. Skania, A. Karocki, G. Stochel and L. Fiedor, *J Biol Inorg Chem*, 2005, **10**, 453–462.

149. C. C. Byeon, M. M. McKerns, W. Sun, T. M. Nordlund, C. M. Lawson and G. M. Gray, *Appl Phys Lett*, 2004, **84**, 5174–5176.

150. M. Promkatkaew, S. Suramitr, T. Karpkird, S. Wanichwecharungruang, M. Ehara and S. Hannongbua, *Photochem Photobiol Sc*, 2014, **13**, 583–594.

151. N. Turro, in *Modern Molecular Photochemistry*, University Science Books, Sausalito, 1991, pp. 170–176.

152. E. I. Sagun, E. I. Zenkevich, V. N. Knyukshto, A. M. Shulga, D. A. Starukhin and C. Von Borczyskowski, *Chem Phys*, 2002, **275**, 211–230.

153. C. Tanielian, C. Wolff and M. Esch, *J Phys Chem*, 1996, **100**, 6555–6560.

154. H. M. Braakhuis, M. V. D. Z. Park, I. Gosens, W. H. De Jong and F. R. Cassee, *Part Fibre Toxicol*, 2014, **11**, 1–25.

155. D. J. Shen and Burgess, *Drug Del Trans Res*, 2014, **3**, 409–415.

156. S. Laurent, D. Forge, M. Port, A. Roch, C. Robic, L. Vander Elst, R. N. Muller, L. V Elst and R. N. Muller, *Chem Rev*, 2008, **108**, 2064–2110.

157. H. Dong, J. Lei, H. Ju, F. Zhi, H. Wang, W. Guo, Z. Zhu and F. Yan, *Angew Chem - Int Ed,* 2012, **51**, 4607–4612.

158. B. Le Ouay and F. Stellacci, *Nano Today*, 2015, **10**, 339–354.

159. P. Sen, A. Sindelo, D. M. Mafukidze and T. Nyokong, *Syn Metal*, 2019, **258**, 116203-116212.

160. L. Sobotta, P. Skupin-mrugalska, J. Piskorz and J. Mielcarek, *Eur J Med Chem*, 2019, **175**, 72–106.

161. R. Słota and G. Dyrda, *Inorg Chem*, 2003, **42**, 5743–5750.